

NEW SOLUTIONS TO THE CHARGED CURRENT B-ANOMALIES

By

POUYA ASADI

A dissertation submitted to the

School of Graduate Studies

Rutgers, The State University of New Jersey

In partial fulfillment of the requirements

For the degree of

Doctor of Philosophy

Graduate Program in Physics and Astronomy

Written under the direction of

David Shih

And approved by

New Brunswick, New Jersey

OCTOBER, 2019

ABSTRACT OF THE DISSERTATION

New Solutions To The Charged Current B-Anomalies

By POUYA ASADI

Dissertation Director:

David Shih

There are a host of different experimental efforts looking for signs of physics beyond the Standard Model. For the most part, the results from these experiments are in agreement with the Standard Model prediction. Nonetheless, a handful of discrepancies have been observed. One of the most significant discrepancies is observed in the flavor-changing processes $B \rightarrow D\tau\nu$ and $B \rightarrow D^*\tau\nu$. In this work we propose two novel explanations for these anomalies and study their phenomenology. The characteristic feature of these two models are (i) use of right-handed neutrinos and a new W' mediator, and (ii) mixing between two leptoquarks after the electroweak symmetry breaking, respectively. We further study the imprint of these models, as well as all other viable solutions, on related asymmetry observables. We motivate the measurement of various asymmetry observables associated with the τ lepton in these processes, as they can likely distinguish different viable solutions.

Acknowledgments

I would like to thank anyone I interacted with, collaborated, or learned from during my PhD. Every single of these encounters taught me something new and truly enriched my experience as a student.

In particular, I deeply appreciate numerous discussions and collaborations with Ariya Basirnia, Matthew Baumgart, Matthew Buckley, Nathaniel Craig, Anthony DiFranzo, Daniel Egana, Marco Farina, Ying-Ying Li, Sebastian Macaluso, Angelo Monteux, Yuichiro Nakai, Tracy Slatyer, and Scott Thomas. Interacting with each of these great physicists helped me understand different aspects of physics and taught me how to think appropriately about different problems.

I also benefited a lot from taking many amazing classes during my PhD. I would like to express my gratitude to Eric Gawiser, Igor Klebanov, Sasha Zamolodchikov, and specially Scott Thomas for their phenomenal courses.

Above all, I have to thank my PhD advisor, David Shih. David has had the single most important impact on my career. He is the best collaborator and the best teacher I have ever had. I will always be in his debt.

Finally, I would like to thank my parents, Ali and Saghar, and my sister, Gelareh, for their support and their lessons on the value of hard work and perseverance.

Dedication

To Gelareh, Saghar, and Ali

Table of Contents

Abstract	ii
Acknowledgments	iii
Dedication	iv
List of Tables	vii
List of Figures	x
1. Introduction	1
1.1. Beyond the Standard Model of Particle Physics	1
1.2. The Charged Current Flavor Anomalies	6
1.3. Three Broad Classes of Solutions	15
1.4. Outline	18
2. A New Solution With RH Neutrinos	20
2.1. Motivation and Overview	20
2.2. General Setup	21
2.3. The Model	24
2.4. Phenomenology and Constraints	32
2.5. Final Remarks	45
3. A New Solution Relying On C_{RL}^V	47

3.1. Motivation	47
3.2. Explaining the Observed $F_{D^*}^L$	48
3.3. A Model for C_{RL}^V	56
3.4. Phenomenology	63
3.5. Comments on RH Neutrinos	72
3.6. Final Remarks	75
4. Discerning Different Solutions	77
4.1. Simplified Models for $R_{D^{(*)}}$	77
4.2. Asymmetry Observables	87
4.3. Distinguishing Different Solutions	96
4.4. Final Remarks	103
5. Outlook	107
Appendix A. Leptonic and Hadronic Functions	111
Appendix B. Details of Fermion-Gauge Boson Couplings	115
Appendix C. Details on Maximizing the Observables	117
Appendix D. Analytic Expressions for the Observables	119
Bibliography	128

List of Tables

1.1. The field content of the SM. The first three rows include the different quarks, followed by the leptons in the next two rows. We also have a neutral scalar, namely the Higgs scalar, and 4 different gauge bosons. The subscripts L, R on the fermions indicates their chirality. For each type of fermion, the three generations are include in the same row. The charges under the SM gauge groups $SU(3) \times SU(2) \times U(1)$ are included as well; for the gauge bosons, we include the mass eigenstates and indicate which group they belong to. The gluon (g) and the photon (γ) correspond to unbroken gauges and thus remain massless. The other masses are from Particle Data Group [3].	4
2.1. The numerical values of different variables used in deriving Eqs. (2.1).	23
2.2. The field content of the model. The right-handed SM-like fermions u_R, d_R , and e_R will eventually mix with the fields charged under the new gauge group $SU(2)_V$ to give rise to the actual right-handed SM fermions. One generation of ν_R , and one generation of $Q_{L/R}$, and $L_{L/R}$ mixing with SM-like fermions, are sufficient to explain the R_D and R_{D^*} anomalies. However, we will see in section 2.4.2 that $N_V > 1$ is generally required to evade $Z' \rightarrow \tau\tau$ searches.	27
3.1. The combination of WCs that maximize $F_{D^*}^L$ for the global average of $R_{D^{(*)}}$ and with various values of $\text{Br}(B_c \rightarrow \tau\nu)$. All these combinations exhibit a large value of C_{RL}^V and C_{LL}^T ; the SM contribution of $C_{LL}^V = 1$ is also largely canceled.	52

3.2.	The combination of WCs that maximize $R_{J/\psi}$ for the global average of $R_{D^{(*)}}$ and with various values of $\text{Br}(B_c \rightarrow \tau\nu)$. Intriguingly, the WCs at the global maximum of $R_{J/\psi}$ exhibit very similar features to those at the global maximum of $F_{D^*}^L$	52
3.3.	Benchmark points that can reach the maximum $F_{D^*}^L$ with a particular C_{RL}^V and fixed $R_{D^{(*)}}$ and $\text{Br}(B_c \rightarrow \tau\nu)$. The $R_{J/\psi}$ with the same set of WCs is calculated as well; these values of $R_{J/\psi}$ are very close to the maximum attainable $R_{J/\psi}$ with the same C_{RL}^V , see fig. 3.3.	56
3.4.	The searches which give the most constraining reducible and irreducible bounds and the relevant diagrams.	67
3.5.	Benchmark points satisfying all the constraints while generating a large $ C_{RL}^V $. In light of the results in Fig. 3.7 we focus on the case of $\tilde{g}_1^{33} \geq g_1^{23}$	72
4.1.	A complete list of the simplified mediator models and resulting effective operators that are possibly relevant for the $R_{D^{(*)}}$ anomalies. The U_1^μ and S_1 LQs as well as the colorless scalars can give rise to two independent WCs, while the rest of the mediators can generate only one. We use $x = 1/8$ in this work, see the text for more details. We indicate in the last column if the model is still viable (by V) or not (by NV), and if not, what experimental constraint rules it out (see Sec. 4.1.3 for discussion of these constraints). The operators with a line crossed over them are severely constrained by the $b \rightarrow s\nu\nu$ constraints as well.	81
4.2.	The Asymmetry Observables studied in this work, our numerical calculation for the prediction in the SM, and the projected Belle II sensitivity (assuming the 50 ab^{-1} full data set) where available. We use these observables to identify different explanations of the anomalies. In the upcoming sections we will assume the observables in $B \rightarrow D^*\tau\nu$ are measured with the same uncertainty as in $B \rightarrow D\tau\nu$	96

4.3. Pairs of benchmark points for the LQ models S_1 , U_1 , and R_2 coupled to LH neutrinos that are less than 1σ apart in our estimation. The approximate uncertainties using Tab. 4.2 are quoted in the first row as well. We need further measurements to distinguish these models in these cases.	102
D.1. The parameter values used in our calculation of the numerical formulas presented in Chap. 4.	129

List of Figures

1.1. The measurement of R_D (top) and R_{D^*} (bottom) from different experiments (with various τ and secondary B taggings). The global average of the measured values (the SM prediction) is shown by the green (red) band. The figure is provided by the HFLAV collaboration [13]. . . .	9
1.2. The measurement of R_D and R_{D^*} from different experiments (with various τ and secondary B taggings). The figure clearly indicated the correlation in the measurement of these observables. The SM is around 4σ away from the global average of all the measurements. The figure is provided by the HFLAV collaboration [13].	10
1.3. The equivalent of Fig. 1.1 with the new Belle analysis of the data with semi-leptonic B tagging. We observe that with the new R_D measurement and the reanalysis of the R_{D^*} result from the same channel, the significance has gone down.	13
1.4. The equivalent of Fig. 1.2 with the new Belle analysis of the data with semi-leptonic B tagging. The global average has become more consistent with the SM, but still shows around 3.1σ discrepancy with the SM.	14
1.5. The generic diagrams that contribute to R_D and R_{D^*} by modifying $b \rightarrow c\tau\nu$ amplitudes with a BSM mediator. The mediator can be one of the three candidates indicated in the text: (a) charged Higgs or W' ; or (b) leptoquarks.	17

2.1.	The dependence of R_D and R_{D^*} on individual WCs from NP (with all the other NP effects being zero). The orange (blue) band indicates the 1σ band of the observed values for R_D (R_{D^*}) [13]. The qualitatively different dependence of $R_{D^{(*)}}$ on operators with left-handed neutrinos (the black lines) and those with right-handed neutrinos (the red lines) is due to the interference with the SM contribution.	25
2.2.	Schematic presentation of gauge groups and matter content of our theory. We have SM-like fields charged under $SU(2)_L \times U(1)_X$ while new vector-like fermions and a new scalar ϕ' are charged under $SU(2)_L \times U(1)_X$. For the purpose of the anomalies of interest, only one generation of singlet ν_R is necessary. Once ϕ' gets a vev, one generation of the new vector-like fermions mixes with SM-like fermions through the Yukawa coupling.	28

- 2.3. A summary of the bounds on our model. For the left (right) plots we are assuming $C_{RR}^V = 0.4$ ($C_{RR}^V = 0.6$), two benchmark values that can account for the $R_{D^{(*)}}$ anomaly. Those on the top (bottom) correspond to the case $N_V = 2$ ($N_V = 3$) generations of new vector-like fermions, only one of which has mixing with SM fermions. We are assuming all the new leptons (quarks) have $m_L = 250$ GeV ($m_Q = 1500$ GeV). The dashed blue curves denote the contours of constant η , while the solid black curves indicate contours of constant $\Gamma_{Z'}/m_{Z'}$. Points within the gray region have corrections to m_W which are outside 1σ observed range according to [69]. (The simple inequality in Eq. (2.30) explains the shape of the gray lines.) Bounds from [56] (obtained by recasting an older ATLAS search [77]) are indicated by the purple region (the colored region is ruled out) while a rough estimation of the bounds from a newer search [78] are denoted by dashed purple lines. As explained in the text, adding extra generations of vector-like matter alleviates the collider bounds. 39
- 2.4. The only potentially dangerous loop-diagram mixing ν_R with the SM neutrinos. Other diagrams are suppressed by lack of tree-level mixing between left-handed fermions charged under different $SU(2)$ groups. Different sources of suppressions, e.g. loop factors, V_{cb} suppression, and heavy mediators, will make this diagram suppressed enough so that we can evade the bounds from neutrino mixing with light-enough new neutrinos. 43

- 3.1. The maximum attainable $F_{D^*}^L$ (left) and the maximum attainable $R_{J/\psi}$ (right) for different values of $\text{Br}(B_c \rightarrow \tau\nu)$ and $R_{D^{(*)}}$. The green and red contours correspond to $\text{Br}(B_c \rightarrow \tau\nu) = 10\%$ and $\text{Br}(B_c \rightarrow \tau\nu) = 30\%$, respectively. The blue (black) triangle indicates the SM predictions (the world-averaged measured values) of $R_{D^{(*)}}$ while the dashed gray ellipses are contours of 1 and 2σ around the world-average measured values. These figures indicate that indeed there exists a combination of the WCs that can explain the observed value of $F_{D^*}^L$ from (1.7); yet, there are no combinations of these WCs that can reach the 1σ range of the observed $R_{J/\psi}$ value in (1.5). 53
- 3.2. The maximum attainable $F_{D^*}^L$ as a function of WCs C_{LL}^T , C_{RL}^V , or C_{LL}^V ; in each plot we marginalize over other WCs, given the constraints $R_D = 0.4$ and $R_{D^*} = 0.3$. The green and red curves correspond to $\text{Br}(B_c \rightarrow \tau\nu) = 10\%$ and $\text{Br}(B_c \rightarrow \tau\nu) = 30\%$, respectively. The purple (orange) band shows the 1σ error bar around the central observed value (SM prediction) of $F_{D^*}^L$. These figures highlight the necessity of NP with all of these WCs in order to explain the observed $F_{D^*}^L$ 55
- 3.3. The maximum attainable $R_{J/\psi}$ as a function of WCs C_{LL}^T , C_{RL}^V , or C_{LL}^V ; in each plot we marginalize over other WCs. The colors and bands are as in fig. 3.2. We see that we can not even reach the 1σ range of the observed $R_{J/\psi}$ for any values of the WCs. 57
- 3.4. The contribution of C_{RL}^V to R_D and R_{D^*} . The orange and the blue bands denote the 1σ range from Eq. (1.3) for R_{D^*} and R_D , respectively. 58

- 3.5. The diagrams generating C_{RL}^V (1st row) and C_{LL}^S, C_{LL}^T (2nd row) WCs in our model. After integrating the mediators out and Fierz transformation, the WC in Eqs. (3.13) is generated. The operator \mathcal{O}_{RL}^V is proportional to the mixing between the LQs. The relevant couplings from Eq. (3.10) are shown for each diagram. 60
- 3.6. An example of a new decay channel for the LQ. This new channel allows the LQ to evade the *reducible* bounds. The new particles ψ and ϕ should be chosen almost degenerate in mass such that the missing particle χ is very soft and is not treated as MET in the searches. The final signature is three jets per LQ. 66
- 3.7. The bounds on $\text{Br}(\text{LQ} \rightarrow b\tau)$ and $\text{Br}(\text{LQ} \rightarrow c\nu)$ from direct LQ searches (brown) and SUSY searches (green). We include the LQ mass M_1 of 650 GeV, 750 GeV, and 850 GeV. For each LQ mass, the colored region is excluded. The (gray) dashed lines denote the branching ratio of the new decay channel. 69
- 3.8. The constraints on the plane of $M_{R_2} = M^{5/3}$ and $M_{\tilde{R}_2} = M^{-1/3}$ from EWPT (gray regions) and DY irreducible bounds for $c\tau$ (brown) and $b\tau$ (blue). We keep the WC C_{RL}^V and the couplings \tilde{g}_1^{33} and g_1^{23} fixed on each plot. Then, λ_3 (black curves) and the lighter mass eigenstate of charge 2/3 LQs (green) are determined. For reducible bounds, we assume the coupling into the new channel is 4π , i.e. maximum allowed by unitarity arguments; with this coupling, the BR into the new decay channel from Fig. 3.6 dominates and all the reducible bounds are subdominant to the EWPT and DY bound. The white region is allowed. 71
- 3.9. The diagrams generating C_{LR}^V (1st row) and C_{RR}^S, C_{RR}^T (2nd row) WCs. The relevant couplings from Eqs. (3.10), (3.16) and (3.23) are shown for each diagram. 73

- 3.10. The diagrams giving rise to various flavor constraints. The most relevant constraint is from $b \rightarrow s\nu\nu$ (the top-left diagram), which only constrains C_{RR}^S and C_{RR}^T . The other processes include : $D_s \rightarrow \tau\nu$ (top-right), the B_s - \bar{B}_s mixing diagrams (middle row), $B \rightarrow K\tau\tau$ or $B_s \rightarrow \tau\tau$ (bottom-left) and $b \rightarrow s\gamma$ (bottom-right). With the exception of the top diagrams, all the diagrams here are suppressed by the neutrino mixing and will not put tight constraints on our model. The relevant couplings for each process are shown as well; this combination of couplings severely constrains the C_{RR}^S operator in Eq. (3.25) and prevents us from generating both C_{RL}^V and C_{LR}^V simultaneously in our setup. All these bounds can be circumvented by suppressing $\tilde{g}_2^2\tilde{g}_1^{33}$. . . 74
- 4.1. Ranges of $R_{D^{(*)}}$ spanned by single operators with complex WCs. The SM prediction is denoted by a cyan dot. No other experimental constraints are imposed in this figure. The 1, 2, and 5σ contours around the current global average are shown as gray-dashed lines. We also show these contours with the projected Belle II precision [2] around the current global average (red ellipses) and a hypothetical average after Belle II that still barely allows a 5σ discovery (magenta ellipses), assuming the current correlation $\rho_{\text{corr}} = -0.2$. (See Sec. 4.1.4 for details.) 79
- 4.2. The range of $R_{D^{(*)}}$ spanned by the simplified models from Tab. 4.1 with complex WCs. The superscript on S_1 and U_1 LQ refers to the neutrino chirality which they are coupled to in each figure. No other experimental constraints are imposed in this figure. The other features are as in Fig. 4.1. 82

- 4.3. The kinematics of $\bar{B} \rightarrow D^{(*)}\tau\nu$ and subsequent $\tau \rightarrow d\nu'$ decay processes, in the center-of-mass frame of the leptonic system (the “ q^2 frame”). The black plane indicates the original decay plane, defined by the B momentum \vec{p}_B (or the $D^{(*)}$ momentum $\vec{p}_{D^{(*)}}$) and the leptonic pair. The red plane is the decay plane of the τ , defined by the visible daughter meson d and invisible daughter neutrino ν' of the τ . The three directions in which we will project the τ polarization asymmetries are indicated in green. 88
- 4.4. A schematic showing the Lorentz boost that relates the angles $\theta_{\tau d}$ in the q^2 frame on the left and θ_{hel} in the τ rest frame on the right. The former angle is reconstructible at the B -factories, while the latter is used to extract $\mathcal{P}_\tau^{(*)}$. Although the τ momentum vector cannot be fully reconstructed at the B factories, its magnitude is measurable, and this is sufficient to relate the two frames. 94
- 4.5. Two-dimensional plots of asymmetry observables for the 10σ scenario. We scan over WCs that result in $R_{D^{(*)}}$ values within the 2σ Belle II error ellipse centered on the present-day world averages. We also impose the $Br(B_c \rightarrow \tau\nu) \leq 10\%$ bound [52]. The projected Belle II precision for each observable, centered on the SM prediction, is indicated by the dashed gray lines, see the text. Regions which can be realized by models with LH SM neutrinos (shown in green) are from U_1 LQ and single operators \mathcal{O}_{LL}^T and \mathcal{O}_{RL}^V , while the one requiring new RH neutrinos (shown in red) corresponds to U_1 LQ. We can distinguish all the models from one another by measuring these asymmetry observables. 98

- 4.6. Two-dimensional plots of asymmetry observables in the 5σ scenario. We scan over WCs which result in $R_{D^{(*)}}$ values within the 2σ Belle II error ellipse centered at $R_D = 0.34$ and $R_{D^*} = 0.275$. We also impose the $b \rightarrow s\nu\nu$ bound [119, 155] and the $Br(B_c \rightarrow \tau\nu) \leq 10\%$ bound [52]. The projected Belle II precision for each observable, centered on the SM prediction, is indicated by the dashed gray lines, see the text. All the currently viable models and single operators remain viable in this scenario. Regions which can be realized by models with LH SM neutrinos are shown in green, while those requiring new RH neutrinos are in red. 100
- 4.7. The \mathcal{P}_T and \mathcal{P}_T^* observables for the points from Fig. 4.6 that are less than 1σ apart in our estimation. These figures indicate that the CP-odd asymmetries \mathcal{P}_T and $\mathcal{P}_T^{(*)}$ may be useful for further distinguishing the R_2 , U_1 , and S_1 leptoquark models coupled to LH neutrinos; however, the fact that they cross at the origin in the left figure also indicates that these asymmetries cannot resolve the difference in all cases. . . 104
- D.1. The q^2 distribution for benchmark WCs for models interacting with LH neutrinos (green curves) and those interacting with RH neutrinos (red curves). The decay rate for $\bar{B} \rightarrow D\tau\nu$ ($\bar{B} \rightarrow D^*\tau\nu$) is shown on top (bottom). We show the viable LQ models whose effective operators from Tab. 4.1 are related through the symmetry in (4.12)–(4.13). The dashed gray line is the SM prediction. The area under each curve is proportional to its prediction for $R_{D^{(*)}}$. Up to a rescaling factor the plots for different types of neutrinos have indistinguishable shapes. . . 125

Chapter 1

Introduction

1.1 Beyond the Standard Model of Particle Physics

The Standard Model (SM) of particle physics is the underlying theory describing the building blocks of our universe and the known interactions between them. It is consisted of three generations of fermions (leptons and quarks) charged under a $SU(3) \times SU(2) \times U(1)$ gauge group. The theory also includes a Higgs scalar that interacts with some of the gauge bosons and the fermions; this Higgs scalar is responsible for generating masses for all these fundamental particles.

While this framework explains most of the observed phenomena in high energy physics, there are a handful of discrepancies between its predictions and the experimental results. The focus of this thesis is on a few of these discrepancies.

Before moving on to the main topic of this thesis, it is worth reviewing the field content of the SM, some of the important properties of each sector that are relevant for our study, and why it is believed there should be physics beyond this framework.

- **$SU(3)$ gauge group.** This gauge group describes the strong force of the SM model. Only the quarks are charged under this gauge group. The strong force is mediated by the exchange of gluons. The $SU(3)$ gauge symmetry is unbroken in the SM, hence the gluons are massless. Despite being massless, their effect is only observable at small scales. The reason for this is that this force becomes stronger as we go to larger distances and, eventually, it becomes strong enough that instead of mediating a force between two separated points it generates

pairs of quarks out of the vacuum.

The non-perturbative behavior associated with the strong force is relevant for energies smaller than this confinement scale at around 1GeV (associated with length scales of around 1fm); only states neutral under this force can be more separated than this. Hence, the fundamental fermions charged under this force, i.e. quarks, are confined inside bounds states neutral under $SU(3)$; these composite states are the hadrons. In this work, we will work extensively with the matrix elements between some of these hadrons.

Due to the non-perturbative nature of the strong force, we can not use the conventional perturbative field theory techniques in order to study the hadronic matrix elements. Instead, various approximate models or numerical lattice studies are invoked to parametrize these matrix elements.

- **$SU(2)_L \times U(1)_Y$ gauge group and the Higgs field.** The force described by these groups is the weak force. Unlike the strong force, this force becomes weaker as we go to larger distances. There are a total of four generators in these gauge groups each of which corresponding to a mediator of this force.

An important phenomena related to this force is the Higgs mechanism. The minimum of the Higgs potential does not respect this gauge symmetry, thus spontaneously breaking it to $U(1)_{em}$. As a result of this breaking, some of the gauge bosons will get masses comparable to the Higgs vacuum expectation value (vev). These are the W^\pm and Z bosons. The surviving gauge group describes electromagnetism and its massless gauge boson in the photon.

Even though W and Z are heavy, thus short-ranged, various precision measurements allow us to track their effects in even longer distances. As will be discussed in the following sections, the discrepancies with the SM that we will study in this work are an outcome of such precision experiments.

- **The SM Fermions.** These particles are the building blocks of the visible matter in our universe. Each fermion has two chiralities : left-handed (LH) and right-handed (RH), which are related to each other through parity symmetry. Different chiralities of the same field have different charges under the weak force of the SM, thus the weak interactions break the parity symmetry.

There are three generations of fermions in the SM. The only differences between these three generations are in their couplings to the Higgs, which in turn gives rise to different masses for them, and their interactions with the W boson. A significant part of the SM rich phenomenology is a result of the existence of these different generations and the cross-generation interactions. The study of these topics are collectively referred to as *flavor physics*. There are numerous excellent reviews on this subject and the on-going research directions, e.g. see [1].

The active areas of research in flavor physics include study of the Cabibbo-Kobayashi-Maskawa (CKM) matrix in the quark interactions with the W boson, signatures of new physics (NP) in rare processes, CP-violation in and beyond the SM, hadron spectroscopy, searches for dark sectors, etc., see for instance [2] for different physics goals in flavor physics and the relevant experiments. The focus of this thesis is on the signatures of NP in rare processes.

We summarize the matter content of the SM model in Tab. 1.1. This framework has explained a wide range of different phenomena from the electroweak symmetry breaking scale at subatomic ranges to the neutrinos behavior in cosmological scales. There are, however, quite a few unexplained issues in the SM. For instance:

- Why are there three generations of matter in the SM? What is the origin of their different Yukawa couplings to the Higgs field?

Field	Mass [GeV]	SM Charges/Gauge Group
$Q_L = \begin{pmatrix} u \\ d \end{pmatrix}_L, \begin{pmatrix} c \\ s \end{pmatrix}_L, \begin{pmatrix} t \\ b \end{pmatrix}_L$	$\begin{pmatrix} 2.16 \times 10^{-3} \\ 4.67 \times 10^{-3} \end{pmatrix}, \begin{pmatrix} 1.28 \\ 0.093 \end{pmatrix}, \begin{pmatrix} 173 \\ 4.18 \end{pmatrix}$	(3,2,1/6)
u_R, c_R, t_R	$2.16 \times 10^{-3}, 1.28, 173$	(3,1,2/3)
d_R, s_R, b_R	$4.67 \times 10^{-3}, 0.093, 4.18$	(3,1,2/3)
e_R, μ_R, τ_R	$0.51 \times 10^{-3}, 0.11, 1.78$	(1,1,-1)
$L_L = \begin{pmatrix} \nu_e \\ e \end{pmatrix}_L, \begin{pmatrix} \nu_\mu \\ \mu \end{pmatrix}_L, \begin{pmatrix} \nu_\tau \\ \tau \end{pmatrix}_L$	$\begin{pmatrix} \sim 10^{-10} \\ 0.51 \times 10^{-3} \end{pmatrix}, \begin{pmatrix} \sim 10^{-10} \\ 0.11 \end{pmatrix}, \begin{pmatrix} \sim 10^{-10} \\ 1.78 \end{pmatrix}$	(1,2,-1/2)
H	125.10	(1,2,1/2)
g	0	$SU(3)$
Z	90.19	$SU(2) \times U(1)$
W	80.38	$SU(2)$
γ	0	$SU(2) \times U(1)$

Table 1.1: The field content of the SM. The first three rows include the different quarks, followed by the leptons in the next two rows. We also have a neutral scalar, namely the Higgs scalar, and 4 different gauge bosons. The subscripts L, R on the fermions indicates their chirality. For each type of fermion, the three generations are include in the same row. The charges under the SM gauge groups $SU(3) \times SU(2) \times U(1)$ are included as well; for the gauge bosons, we include the mass eigenstates and indicate which group they belong to. The gluon (g) and the photon (γ) correspond to unbroken gauges and thus remain massless. The other masses are from Particle Data Group [3].

- Have we discovered all the fundamental particles? Are there other fundamental particles at the shorter scales?
- What is determining the Electroweak symmetry-breaking scale in the Higgs sector?
- Why is the SM gauge group $SU(3) \times SU(2) \times U(1)$? Do these gauge groups have a unified origin?
- What is the nature of the Dark Matter?
- Why are there only LH neutrinos in the SM? Do these particles, like any other SM fermion, have RH partners as well?

Motivated by these questions, and numerous other shortcomings of the SM, many searches for beyond SM (BSM) physics are being carried out. In a handful of these experiments discrepancies with the SM predictions have been observed. These discrepancies have been guiding the BSM model-building in different fronts.

In this thesis, we will focus on a particular set of such "anomalies" in the charged current processes in different flavor physics experiments. The discrepancies we are studying are in a pair of observables called R_D and R_{D^*} , see Sec. 1.2, related to the decays $B \rightarrow D\tau\nu$ and $B \rightarrow D^*\tau\nu$, respectively. After reviewing these observables in the upcoming section, we will introduce two new BSM explanations and how we can distinguish various solutions to these anomalies.

Solutions of these anomalies can guide us toward the right answer to a handful of SM shortcomings mentioned earlier. In particular, as we will see shortly, the solutions to these anomalies require the existence of new heavy states that treat different generations of fermions on different grounds. As a result of this, it is conceivable that these BSM proposals could be a part of a larger structure explaining the difference between different generations and even why there are three generations of fermions.

Furthermore, the new heavy states could play a role in stabilizing the electroweak scale or could serve as a portal between the SM matter and a dark matter candidate.

While these are intriguing questions to think about, we should first understand the anomalies and their possible solutions better. Hence, the focus of this thesis will be directly on the anomalies themselves and the minimal extensions of the SM that can explain them.

1.2 The Charged Current Flavor Anomalies

Experimental tests of the SM have probed many different aspects of potential new physics (NP), including direct searches for new heavy particles at the Large Hadron Collider (LHC), various direct and indirect dark matter detection experiments, neutrino experiments, and precision measurements of flavor physics. For the most part, predictions from the SM are in good agreement with the results from these experiments. There are, however, a handful of anomalies which suggest the existence of new physics.

Arguably, some of the most significant and enduring discrepancies with SM predictions are observed in B -physics experiments. Collaborations such as BaBar [4–6], Belle [7–9], and LHCb [10–12], have observed anomalies in the rate of B -hadron decays, compared to the theoretical predictions of the SM. The most significant deviations from the SM predictions are found in the semi-leptonic decay of B mesons to D or D^* , encapsulated in the ratios R_D and R_{D^*} , defined as

$$R_D = \frac{\Gamma(\bar{B} \rightarrow D\tau\nu)}{\Gamma(\bar{B} \rightarrow D\ell\nu)}, \quad R_{D^*} = \frac{\Gamma(\bar{B} \rightarrow D^*\tau\nu)}{\Gamma(\bar{B} \rightarrow D^*\ell\nu)}, \quad (1.1)$$

where ℓ stands for either electrons or muons.

The Standard Model predictions for these ratios are [5, 6, 13–20]

$$R_D = 0.300 \pm 0.008, \quad R_{D^*} = 0.252 \pm 0.003, \quad (1.2)$$

In order to calculate these ratios, we can factorize the matrix element into the hadronic and the leptonic side; the two sides are connected by a W propagator.

The leptonic side of the calculation can be done straightforwardly. If the masses of different charged leptons were equal, both these ratios would have been equal to 1 as the SM W interacts with all the leptons with the same strength. The deviation from 1 in these predictions are entirely due to the phase space suppression when the off-shell W decays to τ .

On the hadronic side we will have to calculate the $\bar{B} \rightarrow D^{(*)}$ matrix element, for which the perturbative techniques are not useful thanks to the non-perturbative nature of the strong force at the scale of these processes. These matrix elements can be parametrize with the help of a handful of form factors. These form factors in turn can be determined using numerical results from lattice studies, different sum rules and quark models, or with the help of heavy quark limit and heavy quark effective theory (HQET) [21–23]. All these different approaches have been used in calculating the relevant form factors and they all agree with each other [5, 6, 13–20].

As the hadronic matrix element of the numerator and the denominator in $R_{D^{(*)}}$ are the same, by taking the ratio, various sources of uncertainties (such as the uncertainty in some of the hadronic form factors or in some SM parameters such as V_{cb}) cancel [16]. The uncertainties in Eq. (1.2) are mostly due to the uncertainty in m_c/m_b , the remaining uncertainties from the form factors, higher order electromagnetic corrections, and deviation from heavy quark limit (if we use heavy quark effective theory) [16, 6].

Meanwhile, the global average [13] of the observed values [4–6, 8–10] for these ratios are

$$R_D = 0.403 \pm 0.040 \pm 0.024, \quad R_{D^*} = 0.310 \pm 0.015 \pm 0.008, \quad (1.3)$$

where the first (second) experimental errors are due to statistics (systematics). The

dominant sources of uncertainties are the limited data sample, Monte-Carlo statistics, B meson reconstruction, background from decays to excited states like D^{**} , and the error in determining the efficiencies of different channels [6]. These numbers are in sharp disagreement with the SM values reported earlier. A combined analysis [13] shows a $\sim 3.8\sigma$ discrepancy with the SM predictions of Eq. (1.2).

Various experiments have measured $R_{D^{(*)}}$ in various channels. In particular, as τ can not be observed directly, one can look for its different decay channels as independent measurements of $R_{D^{(*)}}$. In the e^+e^- colliders we can further use different taggings on a second B in our event selection. Figure 1.1 shows different measurements of these ratios (with different B and τ taggings) and the SM predictions. The figures show the results from different collaborations and clearly illustrate the deviation from the SM predictions.

There is also some correlation between R_D and R_{D^*} measurements that are not captured in Fig. 1.1. In Fig. 1.2 we present the same data in the R_D - R_{D^*} plane to illustrate this correlation as well. This figure clearly indicates $\sim 4\sigma$ significance for the combination of anomalies.

The relevant experiments measuring $R_{D^{(*)}}$ are included in Fig. 1.1 and Fig. 1.2. Below we briefly review each of these experiments.

- **BaBar.** BaBar is an experiment with asymmetric e^+e^- beam at the center-of-mass energy 10.58GeV, equal to a $\Upsilon(4S)$ mass. The facility is located at SLAC in California. The experiment collected around 426 fb^{-1} of data. After the collision an on-shell $\Upsilon(4S)$ is generated which subsequently decays to a pair of B mesons with a branching ratio above 96% [3]. The integrated luminosity of the experiment corresponds to around 0.5×10^9 pairs of $B\bar{B}$ mesons. Events in which at least one of the B mesons decays hadronically are selected. This B can be reconstructed completely and gives us information about the momentum of the other B . We can use the decays of the second B to probe $R_{D^{(*)}}$ [6].

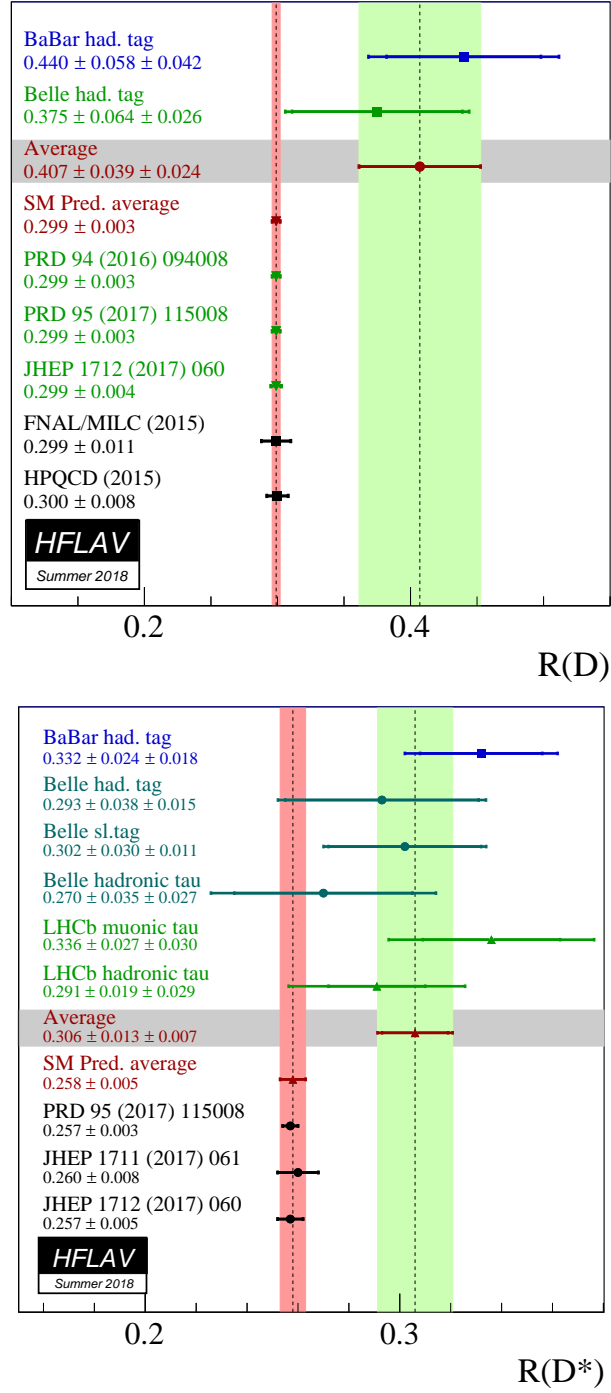


Figure 1.1: The measurement of R_D (top) and R_{D^*} (bottom) from different experiments (with various τ and secondary B taggings). The global average of the measured values (the SM prediction) is shown by the green (red) band. The figure is provided by the HFLAV collaboration [13].

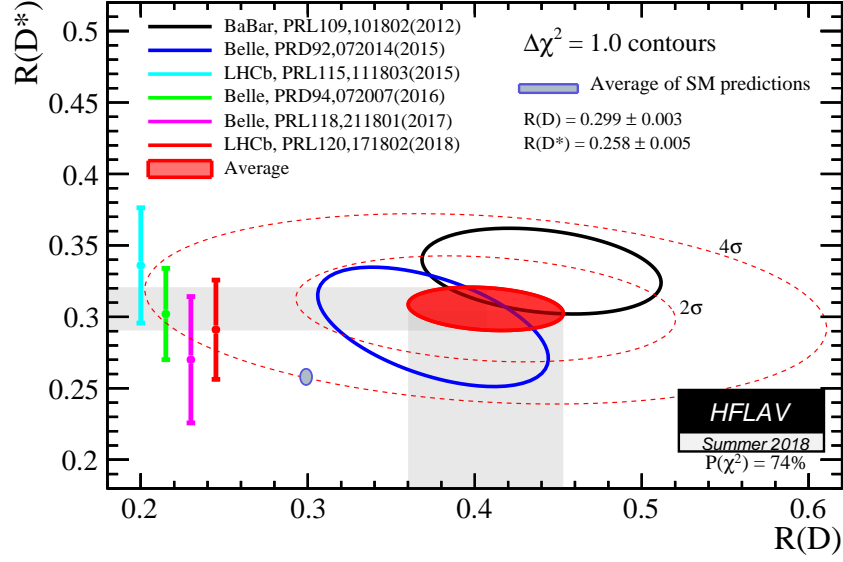


Figure 1.2: The measurement of R_D and R_{D^*} from different experiments (with various τ and secondary B taggings). The figure clearly indicated the correlation in the measurement of these observables. The SM is around 4σ away from the global average of all the measurements. The figure is provided by the HFLAV collaboration [13].

The measurement has been done with both $B^- \rightarrow D^{(*)0}$ and $\bar{B}^0 \rightarrow D^{(*)+}$ and with ~ 20 different bins in the leptonic system momentum q^2 .

- **Belle and Belle II.** The Belle experiment is located at the KEK facility in Japan. It ran from late 90s till 2010 and there are still new analysis published every year on these anomalies. Similar to BaBar, Belle uses an asymmetric e^+e^- beam with center of mass energy equal to $\Upsilon(4S)$. It gathered around 1 ab^{-1} of data which corresponds to around $10^9 \text{ } B\bar{B}$ pairs.

The measurement has been done with both $B^- \rightarrow D^{(*)0}$ and $\bar{B}^0 \rightarrow D^{(*)+}$ and with ~ 20 different bins in the leptonic system momentum q^2 . They have studied exclusive hadronic τ decay channels as well, see Fig 1.1. While BaBar only records the events with hadronic tagging of the secondary B , Belle has studied events in which the second B decays both hadronically and semi-leptonically, see Fig. 1.1.

Belle II is an update of the Belle experiment with some upgrades to the detector. It is projected to gather around 40 times the Belle data in the next ten years. Belle II had its first collisions during the last year and has been gathering data since. The first analyses from this experiment on $R_{D^{(*)}}$ is scheduled to be released by late 2021.

- **LHCb.** LHCb is a part of LHC; thus, unlike the previous experiments, it has a proton-proton beam and operates in the TeV range. While the integrated luminosity at LHCb is in the fb^{-1} ballpark, the large cross-section of the relevant processes allows it to gather comparable number of events.

Unlike an e^+e^- collider environment, here the background is less severe for the leptonic final states. LHCb has looked for the signals of these observables with both $\tau \rightarrow \mu\nu\nu$ [10] and $\tau \rightarrow \pi\pi\pi\nu$ [24] final decays.

Currently Belle II and LHCb are still running and are projected to have enough

data and enough sensitivity to establish if these anomalies are indeed due to NP or not.

Recently Belle has released a new result for measurement of R_D with semi-leptonic tagging of the secondary B . They further re-analyzed and updated their result on R_{D^*} with the same tagging. The equivalent of Fig. 1.1 and Fig. 1.2 with the new result from Belle are depicted in Fig. 1.3 and Fig. 1.4, respectively. These figure indicate that the average observed value of $R_{D^{(*)}}$ has slightly decreased with the new analysis results.

The updated numbers can still constituent a discovery after LHCb and Belle II. For the most of our studies in this thesis we work with the results from Fig. 1.1 and Fig. 1.2; as we will see later on, after lowering the measured value of $R_{D^{(*)}}$ not only the models we are proposing are still viable, but even more models can explain the discrepancy while respecting other experimental bounds.

Lastly, let us introduce two closely-related observables that have recently been measured by Belle and LHCb. Similar to $R_{D^{(*)}}$, an upward fluctuation has been observed in the following ratio

$$R_{J/\psi} = \frac{\Gamma(B_c \rightarrow J/\psi \tau \nu)}{\Gamma(B_c \rightarrow J/\psi \ell \nu)}. \quad (1.4)$$

The value measured by LHCb is [11]

$$R_{J/\psi} = 0.71 \pm 0.17 \text{ (stat)} \pm 0.18 \text{ (sys)}. \quad (1.5)$$

The dominant source of uncertainty is the hadronic form factors. There is significant uncertainty in the SM predictions for this ratio [25–29] as well. The lattice calculation of these form factors is not completed yet and results only exist for small values of q^2 . The most recent calculation of this ratio [29] in the SM uses light-cone sum rules and has found,

$$R_{J/\psi}^{SM} = 0.23 \pm 0.01, \quad (1.6)$$

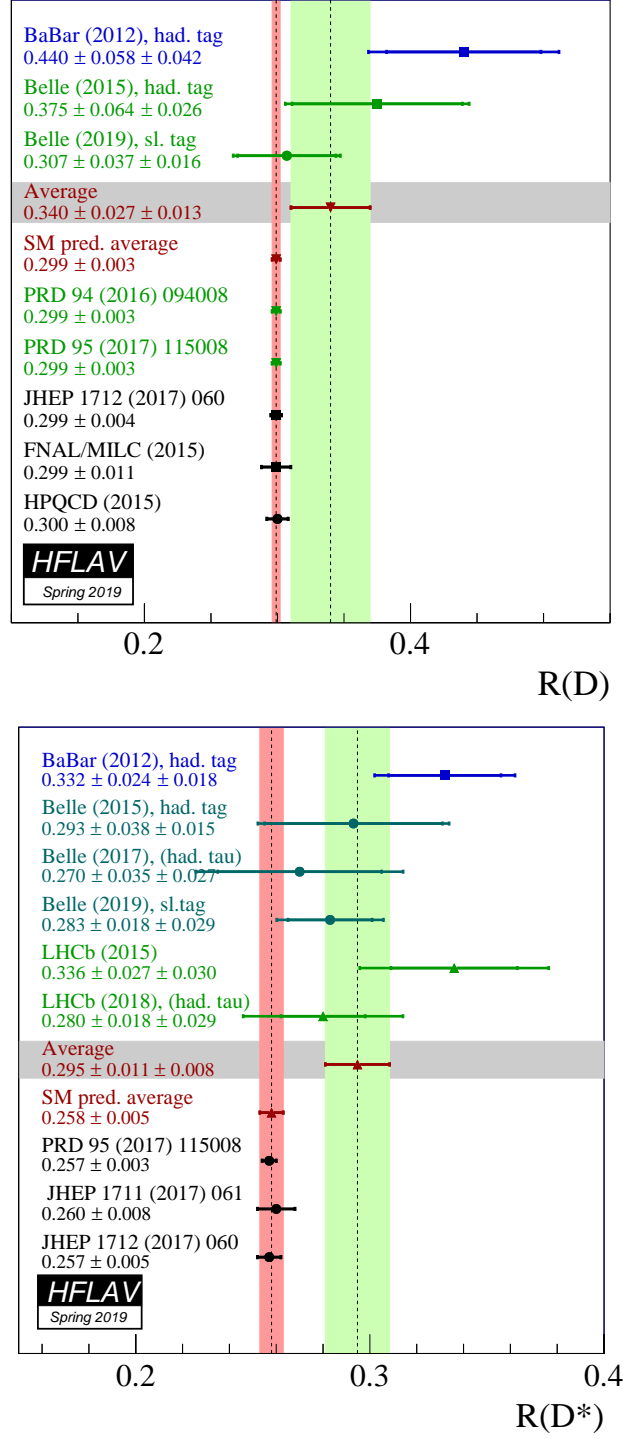


Figure 1.3: The equivalent of Fig. 1.1 with the new Belle analysis of the data with semi-leptonic B tagging. We observe that with the new R_D measurement and the reanalysis of the R_{D^*} result from the same channel, the significance has gone down.

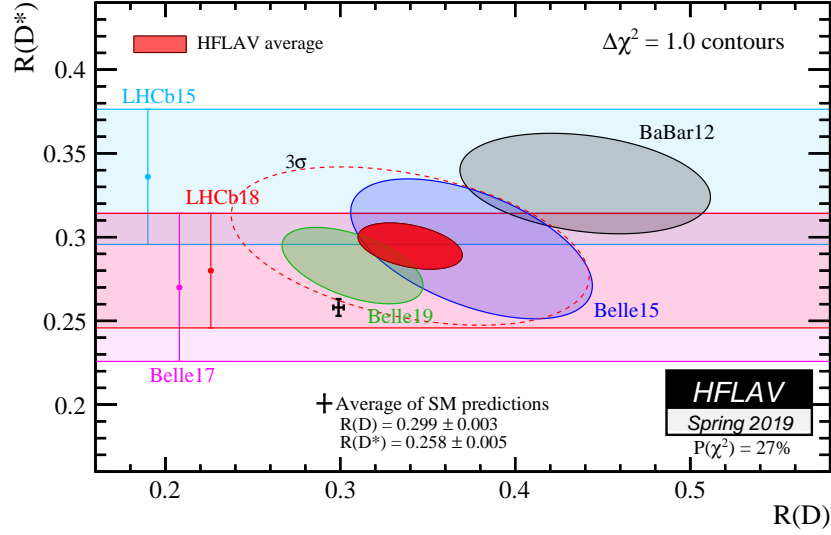


Figure 1.4: The equivalent of Fig. 1.2 with the new Belle analysis of the data with semi-leptonic B tagging. The global average has become more consistent with the SM, but still shows around 3.1σ discrepancy with the SM.

showing $\sim 2\sigma$ discrepancy with the observed value. Earlier calculations of this ratio have larger error bars and find a central value of $R_{J/\psi} \in (0.23, 0.39)$, see [29] and the references therein. Even considering these error bars there is still a significant discrepancy with the experimental result in Eq. (1.5).

There are also a host of different polarization and asymmetry observables [30, 31, 16, 32–42] that can be measured in the $B \rightarrow D^{(*)}\tau\nu$ decays. Recently, Belle has released preliminary results on the measurement of the D^* longitudinal polarization fraction in the $B \rightarrow D^*\tau\nu$ decay [43]

$$F_{D^*}^L = 0.60 \pm 0.08 \text{ (stat)} \pm 0.035 \text{ (sys)}, \quad (1.7)$$

where

$$F_{D^*}^L = \frac{\Gamma(\bar{B} \rightarrow D_L^* \tau \nu)}{\Gamma(\bar{B} \rightarrow D^* \tau \nu)} \quad (1.8)$$

with D_L^* referring to a longitudinally polarized D^* . Meanwhile the SM prediction is

[38, 44, 45], e.g. [44]

$$(F_{D^*}^L)^{SM} = 0.457 \pm 0.010, \quad (1.9)$$

showing around 1.6σ fluctuation compared to the SM. As the dominant source of error in this measurement is statistics, we expect the future updates to significantly reduce the uncertainty in these measurements. Even among the systematic uncertainties the dominant uncertainty can be alleviated by more Monte-Carlo statistics [43].

The underlying hard process for all these observables ($R_{D^{(*)}}$, $R_{J/\psi}$, $F_{D^*}^L$) is $b \rightarrow c\tau\nu_\tau$ through a W exchange. As a result, the combination of all these observations make an appealing case for the existence of BSM effects on this process.

1.3 Three Broad Classes of Solutions

Given the large deviation between the SM predictions and the observed values, an investigation of different possible theoretical explanations beyond the SM is well-motivated. Many theoretical models have been put forward to explain the R_D and R_{D^*} anomalies. Given that the measured $R_{D^{(*)}}$ ratios are higher than their SM predictions, model building efforts have focused on enhancing the rate of $b \rightarrow c\tau\nu$ transitions through new mediating particles (this is much easier than suppressing the rate of $b \rightarrow c(e, \mu)\nu$ transitions, given the much more stringent constraints on new physics coupling to electrons and muons). Integrating out the heavy mediators along with the W at tree-level results in a dimension-6 effective Hamiltonian of the form

$$\mathcal{H}_{\text{eff}} = \frac{4G_F V_{cb}}{\sqrt{2}} \left(\sum_{\substack{X=S,V,T \\ M,N=L,R}} C_{MN}^X \mathcal{O}_{MN}^X \right) \quad (1.10)$$

where the four-fermion effective operators are defined as

$$\begin{aligned} \mathcal{O}_{MN}^S &\equiv (\bar{c}P_M b)(\bar{\tau}P_N \nu) \\ \mathcal{O}_{MN}^V &\equiv (\bar{c}\gamma^\mu P_M b)(\bar{\tau}\gamma_\mu P_N \nu) \\ \mathcal{O}_{MN}^T &\equiv (\bar{c}\sigma^{\mu\nu} P_M b)(\bar{\tau}\sigma_{\mu\nu} P_N \nu), \end{aligned} \quad (1.11)$$

for $M, N = R$ or L . We have separated out the SM contribution in the first term of Eq. (1.10); the normalization factor is conventional and chosen so that $(C_{LL}^V)_{SM} = 1$.

The mediators can be spin-0 or spin-1, and they can either carry baryon and lepton number (leptoquarks) or be B/L neutral (charged Higgs and W'). These possibilities are illustrated in Fig. 1.5. Existing models can be divided into three general categories:

- *Extended Higgs sector* [31, 46–48]. Integrating out a charged Higgs produces the scalar-scalar operators \mathcal{O}^S . These operators are severely constrained by the bounds on $B_c \rightarrow \tau\nu$ branching ratio [49–52], which rules out nearly all explanations of the observed $R_{D^{(*)}}$ using this class of models. It should be noted that these constraints are generic to all models in this category; even general extensions of the Higgs sector, for example Type-III two-Higgs-doublet models (2HDMs), are strongly disfavored for these anomalies.
- *Heavy charged vector bosons* [53, 54]. Integrating out W' s gives rise to the vector-vector operators \mathcal{O}^V . Constraints on these models arise from the inevitable existence of an accompanying Z' mediator. By $SU(2)$ invariance, the $W'b_L c_L$ vertex implies a $Z'b_L s_L$ vertex. In order to avoid catastrophic tree-level flavor-changing neutral currents (FCNCs) from this Z' , some mechanism to suppress the $Z'b_L s_L$ vertex – for example, minimal flavor violation (MFV) – must be assumed [55, 56]. However, this will not suppress $Z'bb$ and $Z'\tau\tau$ vertices in general. In such models, there are therefore typically severe constraints from LHC direct searches for $Z' \rightarrow \tau\tau$ resonances. Evading these limits requires one to go to unnaturally high Z' widths [56, 57].
- *Leptoquarks* [46, 58]. Leptoquarks (LQs) couple quarks and leptons at a vertex. Other than their spin (which can be either zero or one), leptoquarks can be categorized by their representation under SM gauge groups. Appropriate choices

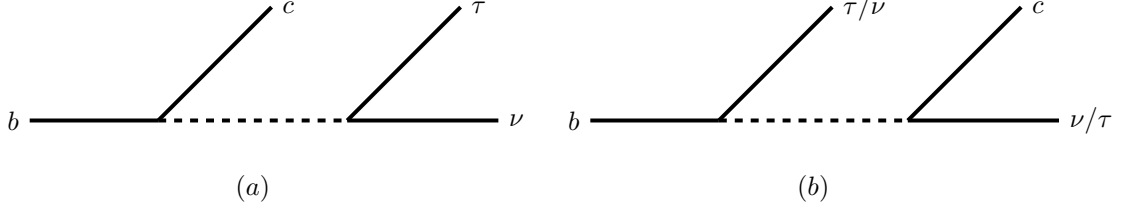


Figure 1.5: The generic diagrams that contribute to R_D and R_{D^*} by modifying $b \rightarrow c\tau\nu$ amplitudes with a BSM mediator. The mediator can be one of the three candidates indicated in the text: (a) charged Higgs or W' ; or (b) leptoquarks.

of these quantum numbers can give rise to many of the operators in Eq. (1.11) after Fierz rearrangement. Given the wide variety of leptoquark models, there are many potentially relevant constraints, ranging from $b \rightarrow s\nu\nu$ flavor bounds [57], to LHC searches for $\tau\tau$ resonances [56, 57], and measurements of the B_c life-time [51, 52]. Nevertheless, viable leptoquark models exist (with either spin-0 and spin-1), and so they are considered to be the favored explanations for the $R_{D^{(*)}}$ anomaly [57, 59], because the alternatives (as described above) are even more stringently constrained.

A more detailed study of these possible mediators will be presented in Chap. 4. As mentioned earlier, each of these mediators can be embedded in a larger structure, which in turn can answer a few other puzzles in the SM model. For instance, a W' comes from a broken gauge symmetry; the SM electroweak gauge group can be embedded in this broken gauge which can potentially stabilize the electroweak symmetry-breaking scale. The same W' or colorless scalars can serve as a portal to a dark sector as well. Different LQs can be embedded in different gauge groups unifying the electroweak gauge groups and the strong gauge.

1.4 Outline

The outline of the rest of the thesis is as follows.

In Chap. 2 we will introduce a model explaining the anomalies using new RH neutrinos instead of the SM neutrinos. While the W' models with LH neutrinos are severely constrained, we will show that using the RH neutrinos instead will allow us to circumvent various experimental bounds. This solution is the first solution of the anomalies with a W' and RH neutrinos, and one of the first solutions relying on the RH neutrinos. The content of this chapter closely follows [60].

Next, In Chap. 3 we first study $F_{D^*}^L$ and $R_{J/\psi}$ in more details and show that one needs C_{RL}^V (or its equivalent with RH neutrinos) in order to explain the observed $F_{D^*}^L$. We then embark upon building the first such model. Our proposed model relies on two LQs and their mixing after the electroweak symmetry-breaking. The content of this chapter closely follows [61] and an on-going work that will soon appear on arXiv.

We then review all the existing minimal solutions in Chap. 4 and start studying a few other related observables. In particular, we will show that τ 's polarization asymmetry and its forward-backward asymmetry can be used to tell different solutions apart. We also highlight the importance of a particular CP-odd τ polarization asymmetry in discerning different models and the need for viable measurement proposals. This chapter is based on [42].

Finally, in Chap. 5 we conclude our work and propose a few future directions for similar studies.

Numerous appendices are included in the end as well. These appendices are again closely related to the results presented in [60, 42, 61].

In App. A we include further details about the calculation of the relevant hadronic and leptonic matrix elements. In particular, we study the leptonic matrix elements with RH neutrinos.

We then study the couplings of the fermions to the gauge bosons in the model of Chap. 2 in App. B. These details are particularly important in the study of the electroweak precision bounds on the model of Chap. 2.

In App. C, we include further details related to the study of $F_{D^*}^L$ and $R_{J/\psi}$ in Chap. 3. In Chap. 3 we model-independently look for the maximum of $F_{D^*}^L$ and $R_{J/\psi}$, through which we arrive at the important role played by C_{RL}^V in explaining the observed $F_{D^*}^L$; App. C elaborates more on how this maximization goes through.

Finally, in App. D we discuss the asymmetry observables in more depth and report the most general analytic formula for each observable with all the WCs from Eq. (1.10).

Chapter 2

A New Solution With RH Neutrinos

2.1 Motivation and Overview

In this chapter we revisit the W' models and identify a new class which avoids the pitfalls described above. All of the existing W' models assume that the missing energy in the semi-leptonic B decay is a SM neutrino.¹ Our key modification is to make the ν enhancing the $B \rightarrow D^{(*)}\tau\nu$ rate a light *right*-handed neutrino, rather than a left-handed neutrino of the SM. As we will show, cosmological and astrophysical considerations require $m_{\nu_R} \lesssim 10$ keV, in which case the kinematics of the B decay into this new particle would be indistinguishable from decays to the (nearly massless) SM neutrinos. Once we integrate out the W' at tree level we generate the dimension six operator \mathcal{O}_{RR}^V . We will show that (similar to \mathcal{O}_{LL}^V) this single operator can explain both R_D and R_{D^*} simultaneously.

Furthermore, by having the W' and Z' couple only to right-handed fermions in the SM (through mixing with heavy vector-like fermions charged under the extra $SU(2)$), we can couple the W' directly to c_R and b_R (instead of to the $q_{L2} = (c_L, s_L)$ and $q_{L3} = (t_L, b_L)$) and so can avoid the $Z'bs$ vertex. Thus there is no danger of tree-level FCNCs in this model, and we obviate the need for the Z' coupling to the third generation fermions to be enhanced by $1/V_{cb}$ when compared to the $W'bc$ coupling required to explain the anomalies. This alleviates the stringent bounds from LHC

¹RH neutrinos have been combined with leptoquarks in [53, 62] and extended Higgs sector in [63, 64]; a model-independent study has been done in [39, 65, 66].

direct searches for $Z' \rightarrow \tau\tau$ resonances which were the main obstacles to previous W' models. That said, we find that these searches still set meaningful bounds on the parameter space of our W' model. These can be satisfied while still keeping the model perturbative, but it requires a mild enhancement to the Z' width ($\Gamma_{Z'}/m_{Z'} \sim 3\text{--}10\%$). We achieve this enhancement by introducing additional vector-like matter charged under the extra $SU(2)$ which do not mix with the SM.

The additional $SU(2)$ and the fermion mixing we introduce between new vector-like fermions and SM fields can modify the relation between W and Z masses and the couplings of SM fermions to W and Z . These are constrained by electroweak precision (EWP) tests. However, the EWP constraints are much milder than in models where the two $SU(2)$'s are broken down to the diagonal by a bifundamental vev (see, e.g. [54, 67]), as there is no W - W' mixing. Additional constraints come from the effect new right-handed light neutrinos have on the cosmic microwave background (CMB) power spectrum, as well as their mixing with SM left-handed neutrinos. Flavor constraints such as FCNCs can be evaded by a suitable choice of fermion mixing, which eliminate FCNCs at tree-level. As we will show, our model survives all current experimental tests, while having some prospect of being discovered or ruled out by the future searches.

2.2 General Setup

In this section, we will review the contributions to R_D and R_{D^*} from each of the dimension six operators in Eq. (1.10), and discuss how this motivates model building with W' 's and RH neutrinos. We begin by writing down useful and fully-general

numerical formulas for R_D and R_{D^*} in the presence of \mathcal{H}_{eff} :

$$\begin{aligned}
R_D \approx R_D^{SM} \times \{ & (|C_{LL}^V + C_{RL}^V|^2 + |C_{RR}^V + C_{LR}^V|^2) \\
& + 1.35 (|C_{RL}^S + C_{LL}^S|^2 + |C_{LR}^S + C_{RR}^S|^2) + 0.70 (|C_{LL}^T|^2 + |C_{RR}^T|^2) \\
& + 1.72 \mathcal{R}e [(C_{LL}^V + C_{RL}^V)(C_{RL}^S + C_{LL}^S)^* + (C_{RR}^V + C_{LR}^V)(C_{LR}^S + C_{RR}^S)^*] \\
& + 1.00 \mathcal{R}e [(C_{LL}^V + C_{RL}^V)(C_{LL}^T)^* + (C_{LR}^V + C_{RR}^V)(C_{RR}^T)^*] \},
\end{aligned} \tag{2.1}$$

$$\begin{aligned}
R_{D^*} \approx R_{D^*}^{SM} \times \{ & (|C_{LL}^V|^2 + |C_{RL}^V|^2 + |C_{LR}^V|^2 + |C_{RR}^V|^2) \\
& + 0.04 (|C_{RL}^S - C_{LL}^S|^2 + |C_{LR}^S - C_{RR}^S|^2) \\
& + 12.11 (|C_{LL}^T|^2 + |C_{RR}^T|^2) - 1.78 \mathcal{R}e [(C_{LL}^V)(C_{RL}^V)^* + C_{RR}^V(C_{LR}^V)^*] \\
& + 5.71 \mathcal{R}e [C_{RL}^V(C_{LL}^T)^* + C_{LR}^V(C_{RR}^T)^*] - 4.15 \mathcal{R}e [(C_{LL}^V)(C_{LL}^T)^* + C_{RR}^V(C_{RR}^T)^*] \\
& + 0.12 \mathcal{R}e [(C_{LL}^V - C_{RL}^V)(C_{RL}^S - C_{LL}^S)^* + (C_{RR}^V - C_{LR}^V)(C_{LR}^S - C_{RR}^S)^*] \}.
\end{aligned}$$

To derive these formulas without calculating any new form factors or matrix elements, one can use the following trick: we expect that these formulas should be invariant under interchange of R and L (i.e. parity) since we sum over all polarizations and spins in the end. Thus we can start from the results in the literature for left-handed neutrinos, and map them using parity to the results for right-handed neutrinos. Since there is no interference between operators with left- and right-handed neutrinos, this mapping does not miss any contributions from mixed terms.

The analytic formulae for the differential decay rates $d\Gamma(B \rightarrow D^{(*)}\tau\nu)/dq^2$ (using only the operators that involve the SM neutrinos) are calculated in [68].² We then integrate the differential decay rates over the momentum transfer in the interval

²We are using a slightly different naming convention for the Wilson coefficients (WCs) and operators than [68]. The map between our convention and the one used in [68] is

$$\begin{aligned}
C_{LL}^V &\rightarrow C_{V1}, & C_{RL}^V &\rightarrow C_{V2} \\
C_{LL}^S &\rightarrow C_{S2}, & C_{RL}^S &\rightarrow C_{S1}, \\
C_{LL}^T &\rightarrow C_T.
\end{aligned} \tag{2.2}$$

V_{cb}	$G_F [\text{GeV}^{-2}]$	$m_{\bar{B}} [\text{GeV}]$	$m_D [\text{GeV}]$
42.2×10^{-3}	1.166×10^{-5}	5.279	1.870
$m_{D^*} [\text{GeV}]$	$m_e [\text{GeV}]$	$m_\mu [\text{GeV}]$	$m_\tau [\text{GeV}]$
2.010	0.511×10^{-3}	0.106	1.777

Table 2.1: The numerical values of different variables used in deriving Eqs. (2.1).

$q^2 \in (m_\tau^2, (m_B - m_{D^{(*)}})^2)$, and substitute the numerical values in Table 2.1 for all the SM parameters [69]. This results in the numerical expressions shown in Eq. (2.1).

We have corroborated this result by directly calculating, from scratch, the contribution of operators involving right-handed neutrinos to $R_{D^{(*)}}$. This involves first calculating the matrix element of $\bar{B} \rightarrow D^{(*)} \tau \nu_R$ using the Hamiltonian in Eq. (1.10). The matrix element factorizes into a leptonic side, which can be calculated straightforwardly, and a hadronic side [58, 70]. The hadronic matrix elements are functions of the masses, the momentum transfer, and a handful of known form factors. A list of these form factors, the leptonic matrix elements with left-handed neutrinos, and the hadronic matrix elements can be found in [58, 39, 68]. Specifically, for the $\bar{B} \rightarrow D \tau \nu$ we use the same form factors as in [39] (derived from the available lattice results [17] and from [71]), while for the $\bar{B} \rightarrow D^* \tau \nu$ decay, following [39, 68], we use the heavy quark effective theory form factors based on [72]. Further details about this calculation, and the analytic formulas from which (2.1) is derived, are included in [42].

Once we find the matrix elements, the differential decay rates of the B meson can be calculated, and verified to be manifestly parity invariant.

We see from (2.1) that C_{LL}^V , C_{LR}^V and C_{RR}^V are special, in that if we only turn on one of these coefficients at a time, then R_D and R_{D^*} share the same functional form. Thus a model that generates one of these coefficients will naturally explain

the curious experimental fact that both R_D and R_{D^*} appear to be high relative to the SM prediction by the same factor. The measured values of R_D and R_{D^*} can be accommodated by the other coefficients at specific points in the complex plane, but then $R_D/R_D^{SM} \approx R_{D^*}/R_{D^*}^{SM}$ would be a numerical accident, and far from natural or automatic. This is illustrated in Fig. 2.1, which shows the dependence of R_D and R_{D^*} on different individual WCs (we focus in this plot on real values for simplicity). The explanation of the $R_{D^{(*)}}$ anomaly in terms of C_{LL}^V is well-explored in the literature. However, the vector operators involving right-handed neutrinos are completely unexplored and would appear, from this point of view, to be equally promising.

Specializing to just C_{RR}^V , the contribution of this Wilson coefficient to each anomaly is given simply by

$$R_D = R_D^{SM} (1 + |C_{RR}^V|^2), \quad (2.3)$$

$$R_{D^*} = R_{D^*}^{SM} (1 + |C_{RR}^V|^2). \quad (2.4)$$

We see that C_{RR}^V in the range 0.4–0.6 can explain both anomalies. For the rest of our phenomenological investigation in this chapter we will focus on this range of this Wilson coefficient.

2.3 The Model

In this section, we introduce our model that explains the R_D and R_{D^*} anomalies using a W' that couples to right-handed SM fermions and a right-handed neutrino. The right-handed neutrino is assumed to be light enough ($m_{\nu_R} \lesssim 10$ keV) so that it is safe from cosmological and astrophysical bounds (see Section 2.4.3); this makes it indistinguishable at the collider from the nearly-massless SM neutrinos in the decays of the B mesons. Integrating out the W' generates the C_{RR}^V Wilson coefficient, capable of explaining both branching ratio measurements, as discussed in the previous section.

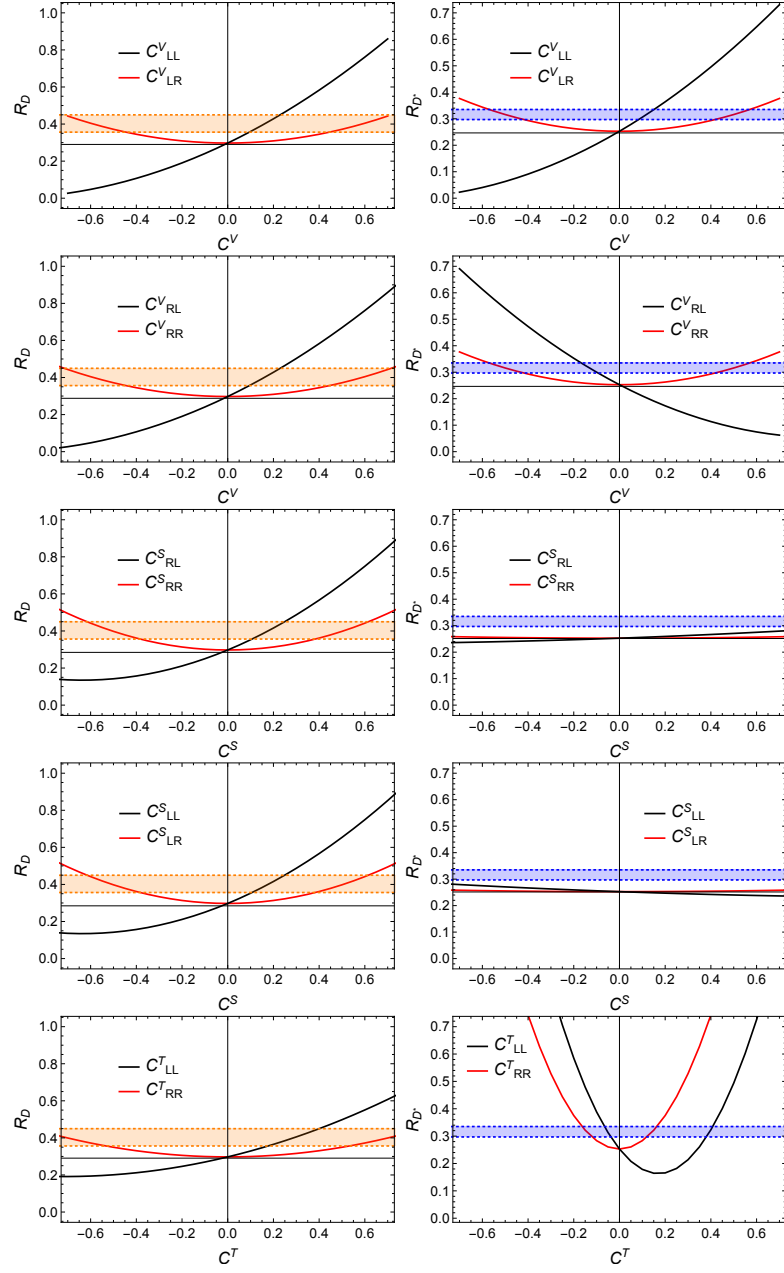


Figure 2.1: The dependence of R_D and R_{D^*} on individual WCs from NP (with all the other NP effects being zero). The orange (blue) band indicates the 1σ band of the observed values for R_D (R_{D^*}) [13]. The qualitatively different dependence of $R_{D^{(*)}}$ on operators with left-handed neutrinos (the black lines) and those with right-handed neutrinos (the red lines) is due to the interference with the SM contribution.

The field content of the model is summarized in Table 2.2, and a schematic presentation of the model is included in Fig. 2.2. Our model embeds hypercharge into a new $SU(2)_V \times U(1)_X$ gauge group (with gauge couplings g_V and g_X respectively), broken by the vev of $\langle\phi'\rangle = \frac{1}{\sqrt{2}}(0, v_V)^T$. It is useful to define the effective hypercharge coupling in our model:

$$g_Y^2 \equiv \frac{g_X^2 g_V^2}{g_X^2 + g_V^2}. \quad (2.5)$$

After the heavy particles are integrated out, g_L and g_Y are identified with the SM gauge couplings, and ϕ is identified with the SM-like Higgs (with vev $\langle\phi\rangle = \frac{1}{\sqrt{2}}(0, v_L)^T$).

In what follows, we expand some of our equations and find the leading contribution in $v_L \ll v_V$ and $g_X, g_L \ll g_V$. This useful limit will simplify many of the equations that will follow. It will also prove to be a fairly good approximation in the region of the experimentally allowed parameter space capable of explaining the B -anomalies.

We extend the SM matter fields with a right-handed neutrino ν_R and N_V generations of vector-like fermions Q and L . In order to explain the anomalies, only one ν_R and one generation ($N_V = 1$) of vector-like fermions suffices. However, we will see in Section 2.4 that additional vector-like fermions (with no mixing into the SM) are required to evade direct $Z' \rightarrow \tau\tau$ searches (by enlarging the width of the Z'). The Lagrangian of the SM is extended to³

$$\begin{aligned} -\mathcal{L} \supset & M_Q \bar{Q}_L Q_R + M_L \bar{L}_L L_R + m_{\nu_R} \nu_R \nu_R \\ & + \tilde{y}^d \bar{Q}_L \phi' b_R - \tilde{y}^u \bar{Q}_L \phi'^* c_R + \tilde{y}^e \bar{L}_L \phi' \tau_R - \tilde{y}^n \bar{L}_L \phi'^* \nu_R + \text{h.c.} \end{aligned} \quad (2.6)$$

After $SU(2)_V \times U(1)_X$ breaking, the vector-like fermions will mix with right-handed fermions carrying SM quantum numbers. This will facilitate the interaction between the b_R , c_R , τ_R and ν_R (mediated by the W' of the $SU(2)_V$) that forms the basis of our explanation of the R_D/R_{D^*} anomaly.

³The scalar potential part of the Lagrangian is straightforward and we omit it for brevity. We can have an interaction $\bar{\nu}_R \phi \ell_L$ at tree-level as well. This operator can generate a large mass and disastrous mixing between neutrinos (see Section 2.4); hence, we must assume its Yukawa coupling is very suppressed at tree-level.

	Generations	$SU(3)$	$SU(2)_L$	$SU(2)_V$	$U(1)_X$
ϕ	1	1	2	1	1/2
q_L	3	3	2	1	1/6
u_R	3	3	1	1	2/3
d_R	3	3	1	1	-1/3
ℓ_L	3	1	2	1	-1/2
e_R	3	1	1	1	-1
ν_R	1	1	1	1	0
ϕ'	1	1	1	2	1/2
Q	N_V	3	1	2	1/6
L	N_V	1	1	2	-1/2

Table 2.2: The field content of the model. The right-handed SM-like fermions u_R , d_R , and e_R will eventually mix with the fields charged under the new gauge group $SU(2)_V$ to give rise to the actual right-handed SM fermions. One generation of ν_R , and one generation of $Q_{L/R}$, and $L_{L/R}$ mixing with SM-like fermions, are sufficient to explain the R_D and R_{D^*} anomalies. However, we will see in section 2.4.2 that $N_V > 1$ is generally required to evade $Z' \rightarrow \tau\tau$ searches.

In the following sections we will explore the spectrum and couplings of the model, in preparation for a detailed study of the phenomenology in section 2.4.

2.3.1 Gauge bosons

The charged gauge bosons do not mix at tree-level; their spectrum is given by:

$$m_W = \frac{1}{2}g_L v_L, \quad m_{W'} = \frac{1}{2}g_V v_V. \quad (2.7)$$

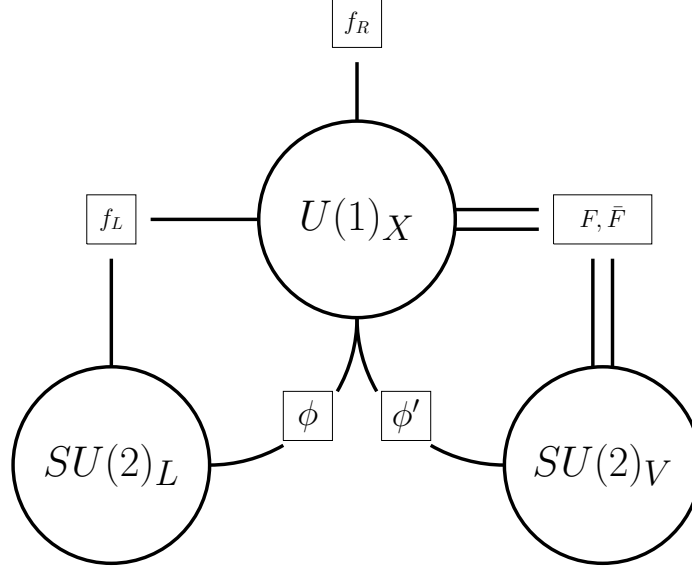


Figure 2.2: Schematic presentation of gauge groups and matter content of our theory. We have SM-like fields charged under $SU(2)_L \times U(1)_X$ while new vector-like fermions and a new scalar ϕ' are charged under $SU(2)_L \times U(1)_X$. For the purpose of the anomalies of interest, only one generation of singlet ν_R is necessary. Once ϕ' gets a vev, one generation of the new vector-like fermions mixes with SM-like fermions through the Yukawa coupling.

Meanwhile, the spectrum of neutral gauge bosons is given by:

$$m_Z^2 \approx \frac{1}{4} (g_L^2 + g_Y^2) v_L^2 \left(1 - \frac{v_L^2 \varepsilon^4}{v_V^2} + \mathcal{O} \left(\varepsilon^6 \times \left(\frac{v_L}{v_V} \right)^4 \right) \right), \quad (2.8)$$

$$m_{Z'}^2 \approx \frac{1}{4} g_V^2 v_V^2 \left(1 + \mathcal{O} \left(\varepsilon^4 \times \left(\frac{v_L}{v_V} \right)^2 \right) \right), \quad (2.9)$$

where $\varepsilon \equiv g_X/g_V$.

These expressions arise from diagonalizing the following mass matrix:

$$\mathcal{L} \supset -\frac{1}{8} \begin{pmatrix} B & W_3^L & W_3^V \end{pmatrix} \begin{pmatrix} g_X^2(v_L^2 + v_V^2) & -g_L g_X v_L^2 & -g_V g_X v_V^2 \\ -g_L g_X v_L^2 & g_L^2 v_L^2 & 0 \\ -g_V g_X v_V^2 & 0 & g_V^2 v_V^2 \end{pmatrix} \begin{pmatrix} B \\ W_3^L \\ W_3^V \end{pmatrix} \quad (2.10)$$

via

$$\begin{pmatrix} B \\ W_3^L \\ W_3^V \end{pmatrix} \equiv \mathcal{R}^\dagger \begin{pmatrix} A \\ Z \\ Z' \end{pmatrix}, \quad (2.11)$$

where, to leading order in v_L/v_V and ε , the rotation matrix is

$$\mathcal{R}^\dagger = \begin{pmatrix} \frac{g_L}{\sqrt{g_L^2 + g_X^2}} & -\frac{g_X}{\sqrt{g_L^2 + g_X^2}} & -\varepsilon \\ \frac{g_X}{\sqrt{g_L^2 + g_X^2}} & \frac{g_L}{\sqrt{g_L^2 + g_X^2}} & 0 \\ \frac{g_L}{\sqrt{g_L^2 + g_X^2}} \varepsilon & -\frac{g_X}{\sqrt{g_L^2 + g_X^2}} \varepsilon & 1 \end{pmatrix} + \mathcal{O}(\varepsilon^2). \quad (2.12)$$

In this limit we see that W_3^V can be identified with the Z' while the photon A and Z boson are a combination of B and W_3^L with a similar mixing pattern as in the SM. We also observe from Eq. (2.9) that $m_{Z'}$ is identical to $m_{W'}$ up to $\mathcal{O}(\varepsilon^4)$ corrections. Further details on the mass matrix and the mixing can be found in Appendix B.

2.3.2 Fermion mass and mixing

From Eq. (2.6), after symmetry breaking, the relevant part of the fermion mass matrices can be written as

$$\begin{pmatrix} \bar{F}_L & \bar{f}_L \end{pmatrix} \begin{pmatrix} M_F & \frac{1}{\sqrt{2}} \tilde{y}_f v_V \\ 0 & m_f \end{pmatrix} \begin{pmatrix} F_R \\ f_R \end{pmatrix}, \quad (2.13)$$

where (F, f) refers to a paired set of a new vector-like fermion and a fermion carrying SM charges. As discussed above, to explain the anomalies without introducing FC-NCs, these pairs should be (U, c) , (D, b) , (E, τ) , or (N, ν) , where (U, D) and (E, L) come from the vector-like fermions Q and L respectively after $SU(2)_V$ breaking.

Here we are implicitly working in the mass basis of the SM-like fermions, i.e. we imagine having already performed the CKM rotation on the left-handed SM-like matter fields, so that m_f is a number, not a matrix.

Given the structure of the mass matrix above, and the fact that the new fermion masses are much higher than SM masses, the left-handed fermions are essentially not mixed with the new vector-like fermions. As a result, for the left-handed fermions, the relationship between gauge and mass basis – and thus the CKM matrix – is the same as SM.

Meanwhile, the right-handed fermions are highly mixed with the new vector-like particles. The mixings can be parametrized by the following replacements

$$\begin{pmatrix} F_R \\ f_R \end{pmatrix} \rightarrow \begin{pmatrix} \mathcal{U}_{11}^{f*} & \mathcal{U}_{21}^{f*} \\ \mathcal{U}_{12}^{f*} & \mathcal{U}_{22}^{f*} \end{pmatrix} \begin{pmatrix} F_R \\ f_R \end{pmatrix}, \quad (2.14)$$

In order for the lighter mass eigenvalues to match the observed quark and lepton masses, the numerical values of m_f must differ from the SM by an $\mathcal{O}(1)$ amount.

2.3.3 Fermion-vector boson couplings

We begin with the coupling to new gauge bosons. The mixing pattern derived in the previous section gives rise to couplings between the W' gauge bosons and right-handed SM fermions:

$$\mathcal{L} \supset \frac{g_V}{\sqrt{2}} W'_\mu \left(\mathcal{U}_{21}^{b*} \mathcal{U}_{21}^c \bar{c}_R \gamma^\mu b_R + \mathcal{U}_{21}^{\tau*} \mathcal{U}_{21}^\nu \bar{\nu}_R \gamma^\mu \tau_R \right) + \text{h.c.} \quad (2.15)$$

The coupling to left-handed SM fermions is highly suppressed in the large v_V and g_V limit, and so we neglect it in the following. After integrating out the W' we generate

the desired C_{RR}^V operator, which can explain the R_D/R_{D^*} anomaly at tree-level. In our model, the Wilson coefficient is given by:

$$C_{RR}^V = \frac{g_V^2 \mathcal{U}_{21}^e \mathcal{U}_{21}^\nu \mathcal{U}_{21}^d \mathcal{U}_{21}^u}{4\sqrt{2}m_{W'}^2 G_F V_{cb}}. \quad (2.16)$$

In order to eventually study the constraints from Z' resonance production in LHC, we also need the coupling of fermions to Z' . To leading order, the couplings of the Z' to right-handed fermions will be

$$\mathcal{L} \supset \frac{g_V}{2} Z'_\mu \left(|\mathcal{U}_{21}^e|^2 \bar{c}_R \gamma^\mu c_R + |\mathcal{U}_{21}^\nu|^2 \bar{\nu}_R \gamma^\mu \nu_R - |\mathcal{U}_{21}^b|^2 \bar{b}_R \gamma^\mu b_R - |\mathcal{U}_{21}^t|^2 \bar{\tau}_R \gamma^\mu \tau_R \right). \quad (2.17)$$

Even if we go beyond this leading order, we observe that the Z' couplings to SM fermions are flavor diagonal and our model evades the constraining bounds from tree-level FCNCs at tree-level, as advertised. Again, the coupling of Z' to the left-handed SM fermions is highly suppressed and we ignore it.

Let us now study the couplings of fermions to SM gauge bosons. These couplings will be relevant in studying EWP tests, see Section 2.4.1. The coupling of W to left-handed fermions has the same form as in the SM:

$$\mathcal{L} \supset \frac{1}{\sqrt{2}} g_L W_\mu^+ \bar{f}_L \gamma^\mu f_L' + \text{h.c.} \quad (2.18)$$

and similarly for photons:

$$\mathcal{L} \supset e Q_f A_\mu \bar{f} \gamma^\mu f, \quad (2.19)$$

where

$$e = g_L \frac{g_Y}{\sqrt{g_L^2 + g_Y^2}}, \quad Q_f = Y + T_3^L = X + T_3^L + T_3^V. \quad (2.20)$$

Finally, the coupling to the Z takes the form:

$$\mathcal{L} \supset \sqrt{g_L^2 + g_Y^2} Z_\mu \left((c^{Zf} + \delta c_L^{Zf}) \bar{f}_L \gamma^\mu f_L + (c^{Zf} + \delta c_R^{Zf}) \bar{f}_R \gamma^\mu f_R \right), \quad (2.21)$$

where

$$c^{Zf} = \left(T_3^L - Q_f \frac{g_Y^2}{g_L^2 + g_Y^2} \right) \quad (2.22)$$

is as in the SM, and

$$\begin{aligned}\delta c_R^{Zf} &\approx Q_f \frac{v_L^2 \varepsilon^4}{v_V^2} \mp \frac{1}{2} \frac{v_L^2 \varepsilon^2}{v_V^2} (\mathcal{U}_{21}^f)^2, \\ \delta c_L^{Zf} &\approx (Q_f - T_3^L) \frac{v_L^2 \varepsilon^4}{v_V^2},\end{aligned}\tag{2.23}$$

parametrize the deviations from the SM formulas. The minus (plus) sign in Eq. (2.23) is for up-type quarks (down-type quark and charged leptons); further details on these equations and couplings are included in Appendix B. These deviations arise either through Z – Z' mixing (the terms that are independent of \mathcal{U}_{21}^f), or through fermion mixing with new vector-like fermions (the term proportional to $(\mathcal{U}_{21}^f)^2$). Following [73], we will use these deviations in the couplings in our study of the EWP bounds in Section 2.4.1.

2.4 Phenomenology and Constraints

In this section we demonstrate that our model can generate the necessary interactions to explain the B -physics anomalies while evading all present constraints.

We begin by establishing the parameter space of the model. There are six underlying parameters most relevant for our studies: the three gauge couplings (g_L, g_X, g_V), the vevs (v_L, v_V), and the fermion mixing parameter \mathcal{U}_{21} .⁴ Other parameters that we encounter in our studies can be derived from these six quantities.

Some experimental measurements can be used to impose further relationships between these core quantities. In particular, given the precise bounds on G_F , α_{em} , and m_Z , we keep these quantities fixed at their experimentally observed values [69]

$$G_F = 1.16637 \times 10^{-5} \text{ GeV}^{-2}, \quad \alpha_{\text{em}}(m_Z) = 7.755 \times 10^{-3}, \quad m_Z = 91.1875 \text{ GeV}.\tag{2.24}$$

⁴We assume from this point onwards that the mixing parameter is the same for all types of fermions so as to simplify our analysis.

We will denote the values of the gauge couplings derived from these measured quantities (assuming the SM gauge structure holds) as

$$\hat{g}_Y = 0.356, \quad \hat{g}_L = 0.650. \quad (2.25)$$

We can fix v_L using the relation $G_F = 1/\sqrt{2}v_L^2$ (which is a tree-level relation that continues to hold in our model):

$$v_L = 246.2 \text{ GeV}. \quad (2.26)$$

Then, we can use Eqs. (2.8) and (2.19) to solve for g_Y and g_L in terms of the experimental values of $(\alpha_{\text{em}}, m_Z)$ and the other parameters of our model. To the first sub-leading order, the gauge couplings g_Y and g_L in our model are given by

$$g_Y = \hat{g}_Y \left(1 - \frac{\hat{g}_Y^6 v_L^2}{2g_V^4 (\hat{g}_L^2 - \hat{g}_Y^2) v_V^2} + \mathcal{O} \left(\varepsilon^6 \times \left(\frac{v_L}{v_V} \right)^4 \right) \right), \quad (2.27)$$

$$g_L = \hat{g}_L \left(1 + \frac{\hat{g}_L^2 \hat{g}_Y^4 v_L^2}{2g_V^4 v_V^2 (\hat{g}_L^2 - \hat{g}_Y^2)} + \mathcal{O} \left(\varepsilon^6 \times \left(\frac{v_L}{v_V} \right)^4 \right) \right), \quad (2.28)$$

where \hat{g}_Y and \hat{g}_L are the SM values given above. Evidently, the values of g_Y and g_L are shifted from their SM values by higher order corrections in ε and v_L/v_V .

Using the three experimentally measured quantities $(G_F, \alpha_{\text{em}}, m_Z)$, we have reduced the number of undetermined variables that span our parameter space to three: $(g_V, v_V, \mathcal{U}_{21})$. We work in terms of the more physical parameters $(g_V, m_{W'}, C_{RR}^V)$, where

$$C_{RR}^V = \frac{v_L^2}{v_V^2} \frac{(\mathcal{U}_{21})^4}{V_{cb}} \quad (2.29)$$

is derived from Eq. (2.16) after setting all the mixing angles equal.

2.4.1 Electroweak precision tests

Our study of the EWP observables in our model closely follows the analysis in [73]. Given the precise measurements of G_F , α_{em} , and m_Z , these quantities are fixed at their experimentally observed values. Our model can then be constrained by requiring

that the NP corrections to the W mass and the coupling of the W and Z gauge bosons to the SM fermions are within the experimental uncertainties [73].

We saw in Eqs. (2.27)–(2.28) that keeping G_F , α_{em} , and m_Z fixed implies that g_L and g_Y should slightly deviate from the SM gauge couplings (\hat{g}_L and \hat{g}_Y). This amounts to a change in m_W from the SM predictions. Demanding the deviation in m_W ($= 80.385 \pm 0.015$ GeV) [69] to be within the 1σ experimental range, we find

$$m_W g_V \gtrsim 0.97 \text{ TeV}. \quad (2.30)$$

This is the most-constraining limit we get from EWP observables on our model.

In principle there could be additional EWP limits coming from deviations in W/Z couplings to fermions compared to the SM predictions. No such deviation occurs for the photon, as we have set the coupling e to its experimentally observed value in Eq. (2.19). From Eq. (2.18), the W the coupling is g_L . While g_L deviates from the SM value according to Eq. (2.28), this is precisely the deviation that is being constrained by the W mass measurement. The W couplings to fermions do not offer any additional constraint, as they are less precisely measured than the W mass.

Finally, we consider the Z couplings to fermions, shown in Eq. (2.21). These deviations are captured by the $\delta c_{L,R}^{Zf}$ variables in Eq. (2.23).⁵ The m_W constraint Eq. (2.30) forces $v_V \gtrsim 1$ TeV, and we will see in the next subsection that $g_V \gtrsim 1$. Using these values in Eq. (2.23), we find that $\delta c_R^{Zf} \lesssim 10^{-3}$ and δc_L^{Zf} is even smaller.

The most constraining limits on the fermion couplings are at the $(\text{few}) \times 10^{-3}$ level (coming from δc_R^{Ze} and $\delta c_R^{Z\tau}$) [73]. Therefore, by satisfying the EWP constraint on m_W and the collider bounds of the next subsection, these bounds are automatically satisfied.⁶

⁵The additional deviations from $g_L \neq \hat{g}_L$ and $\hat{g}_Y \neq g_Y$ in Eqs. (2.27)–(2.28) are negligible once we have satisfied the W mass constraint.

⁶As a result of a forward-backward asymmetry anomaly in LEP [73, 74], δc_R^{Zb} is approximately 2σ away from the SM prediction; we do not try to fit this anomaly in our model. Instead, our model predicts a very small δc_R^{Zb} , in agreement with SM predictions. According to the analysis of [73], the 1σ best-fit regions of some other couplings do not include the SM values either.

2.4.2 Collider Searches

Since the W' and Z' couple to quarks and leptons, they can be produced resonantly at the LHC. A number of different dedicated searches at LHC target such signatures [75–79]. In this section we study the bounds that these searches impose on our model.

We focus on what should be the most constraining mode: resonant production of Z' 's that subsequently decay to $\tau^+\tau^-$ (the situation for $W' \rightarrow \tau\nu$'s should be similar). The relevant LHC searches [75–79] all assumed a narrow resonance when setting their limits. We will be interested in the possibility of wide resonances (indeed, this will be necessary to evade these limits), so it is necessary to recast these searches.

Such a recast was performed for ATLAS searches of resonances decaying to high p_T $\tau\tau$ final states using up to 13.2 fb^{-1} of the 13 TeV dataset [77, 80, 81] in [56]. This paper focused on Z' models with mixing through left-handed SM fermions and W' 's and Z' 's that couple primarily to the 3rd generation to avoid FCNCs. As a result, the cross sections are dominated by $bb \rightarrow Z' \rightarrow \tau\tau$, and [56] placed limits on the ratio

$$\eta \equiv \frac{|g_b g_\tau| v_L^2}{m_{Z'}^2}, \quad (2.31)$$

as a function of $m_{Z'}$ and $\Gamma_{Z'}/m_{Z'}$, where g_b (g_τ) denotes the coupling of left-handed b quarks (τ leptons) to Z' . For the couplings required to explain the R_D , R_{D^*} anomaly, [56] found that $\Gamma_{Z'}/m_{Z'} \gtrsim 30\%$ was required, leading to the conclusion that perturbatively calculable W' explanations of the anomaly were not viable. This is consistent with other works on W' explanations of the R_D/R_{D^*} anomaly [55, 54, 82].

This conclusion was a consequence of assuming MFV to suppress dangerous tree-level FCNCs which, in turn, implied a $1/V_{cb}$ enhancement of the Z' couplings to bb relative to the $W'bc$ coupling. In our model, on the other hand, we avoid FCNCs by having the W' and Z' only couple to right-handed fermions. Thus our $Z'\tau\tau$ and $Z'bb$ couplings will be the same order as the $W'bc$ coupling, and the bounds from LHC searches on $Z' \rightarrow \tau\tau$ will become much less constraining. Hence we expect a smaller

width to be sufficient to evade experimental bounds.

Indeed, we can see this explicitly from the formula for η in our model. As we have substantial $Z'cc$ couplings in addition to the coupling to b_R , the definition of the parameter η of Eq. (2.31) must be modified to

$$\eta = \frac{v_L^2}{m_Z^2} g_R^{Z'\tau\tau} \sqrt{(g_R^{Z'bb})^2 + \chi_c (g_R^{Z'cc})^2} \approx V_{cb} C_{RR}^V \sqrt{1 + \chi_c} + \mathcal{O}\left(\varepsilon^3 \times \left(\frac{v_L}{v_V}\right)^3\right), \quad (2.32)$$

where $g_R^{Z'ff}$ denotes the coupling of right-handed fermion f to Z' , Eq. (2.17), and the second equality only contains the leading order in v_L/v_V and ε . Note that the second equality also uses the assumption that all the mixing angles \mathcal{U}_{21}^f are equal. Here χ_c is the ratio of the production cross-section from initial cc and bb states assuming identical couplings. This captures the parton distribution function (p.d.f.) enhancement from the cc production channel. We obtain this ratio by simulating our model for each resonance mass using MADGRAPH5_AMC@NLO 2.5.5 [83]⁷. Over the ranges of $m_{Z'}$ that interests us, we find $\chi_c \sim 2$ –3. With these modifications we can apply the bounds on η in [56] to our model.

Interestingly, we learn that (under the simplifying assumption of equal mixings) the R_D/R_{D^*} anomaly uniquely predicts η and hence the rate of $bb \rightarrow Z' \rightarrow \tau\tau$ at the LHC in our model. Given the range of C_{RR}^V and χ_c in our model, Eq. (2.32) implies $\eta \in (0.026, 0.048)$. For this range of η and a generic Z' mass of ~ 1 TeV, Figure 4 of the recast [56] indicates that a minimum $\Gamma_{Z'}/m_{Z'}$ of ~ 3 –10% is required to evade the collider bounds.

To proceed further in applying collider limits to our model, we need a formula for $\Gamma_{Z'}$. This requires us to make a choice about the available decay channels for the Z' . The Z' can decay into SM fermions. If kinematically allowed, it can also decay to pairs of the heavy vector-like fermions, or a single heavy fermion and a SM

⁷We use the NNPDF23_lo_as_0130_qed p.d.f to calculate these production cross-sections. We also study the p.d.f and the scale uncertainties in the Z' production cross-section and find less than 10% error in the cross-section. This will not affect the collider bounds on our model significantly.

partner. The lower bound on new vector-like quarks is found to be above 1 TeV across a number of different searches with a variety of assumptions about decay channels [84–92]. We conservatively assume the new vector-like quarks are above 1.5 TeV to evade these tight bounds. As a result of these large masses (compared to the ~ 1 TeV Z'), decays to such fermions do not contribute significantly to the Z' width.

CMS has recently released a search [93] which significantly improves bounds on uncolored fermions. However, even these updated bounds are still far less constraining than the ones on the colored particles. The search in [93] targets the decay of a heavy new set of leptons into the SM charged leptons, plus W and/or Z gauge bosons that subsequently decay leptonically. In particular, the τ leptons in the chain should decay leptonically as well. The bounds from this search, however, are not that constraining for our model due to the following reasons.

- Given the particular mixing pattern chosen in our model, only the SM τ leptons appear in the decay chain. As indicated in [93], the bounds on this tau-phillic part of the parameter space are the loosest.
- Compared to their SM counterpart, the new gauge bosons W' and/or Z' in the decay chain have a lower BR into the light leptons (which is almost exclusively from the leptonic decay of a τ lepton) that further loosens the bounds on our model.

Multiplying all the BRs together, we get a relative suppression of the rate into light leptons compared to the model studied in [93]. Modifying the rates reported in [93] accordingly, the bounds on the new leptons in our model turn out far below 200 GeV, which is the smallest mass considered in [93] for the new leptons. We conservatively assume all heavy leptons in our model are around 250 GeV. To enhance the Z' width, we will allow there to be N_V generations of new vector-like leptons (only one of which has mixing with the SM fermions).

Given the complicated expressions for the couplings, the full expression for $\Gamma_{Z'}$ is lengthy but straightforward, and we omit it here. However, a simple approximate formula (that is nevertheless fairly accurate) can be obtained if we neglect phase space suppressions and keep only the leading order expressions in ε and v_L/v_V (e.g. Eq. (2.17) for the Z' couplings to SM fermions and its analogues for the heavy vector-like states):

$$\frac{\Gamma_{Z'}}{m_{Z'}} \approx \frac{g_V^2}{48\pi} \left((2N_V - 1) + \mathcal{U}_{22}^4 + \mathcal{U}_{22}^2 \mathcal{U}_{21}^2 + 4\mathcal{U}_{21}^4 \right). \quad (2.33)$$

Using $\mathcal{U}_{21}^2 + \mathcal{U}_{22}^2 = 1$ and Eq. (2.16), we can rewrite Eq. (2.33) in terms of $m_{W'}$ and C_{LL}^V .

The different terms in Eq. (2.33) are, respectively: the decay to a pair of heavy left-handed leptons and to a pair of the heavy right-handed leptons that did not mix with the SM-like leptons (there are $N_V - 1$ of these); the decay to the one pair of heavy right-handed leptons that did mix with the SM-like leptons; the decay to one heavy lepton and one SM lepton; and the decay to a pair of SM leptons and quarks. The factor of 4 in the last term is a consequence of the color factors for quarks.

The bounds from EWP measurements (m_W more specifically) and collider searches are summarized in Fig. 2.3, for two representative choices of the Wilson coefficient ($C_{RR}^V = 0.4$ and $C_{RR}^V = 0.6$) that can account for the $R_{D^{(*)}}$ anomaly. For every point below the red line, the required \mathcal{U}_{21} is larger than 1, hence the indicated Wilson coefficient is not attainable in that region. It can be seen that the contours of constant $\Gamma_{Z'}/m_{Z'}$ are approximately captured by Eq. (2.33). The contours of constant η are also indicated; they are mostly captured by the (constant) prediction of Eq. (2.32); the small residual variation is due to variations in χ_c and higher order terms in the ε and v_L/v_V expansion.

One sees that for $C_{RR}^V = 0.4$, η is always small enough compared to the width ($\eta \sim 0.02-0.025$), so that there is no bound from the searches recast by [56]. However, for $C_{RR}^V = 0.6$, η is large enough that there is a nontrivial bound. As we increase

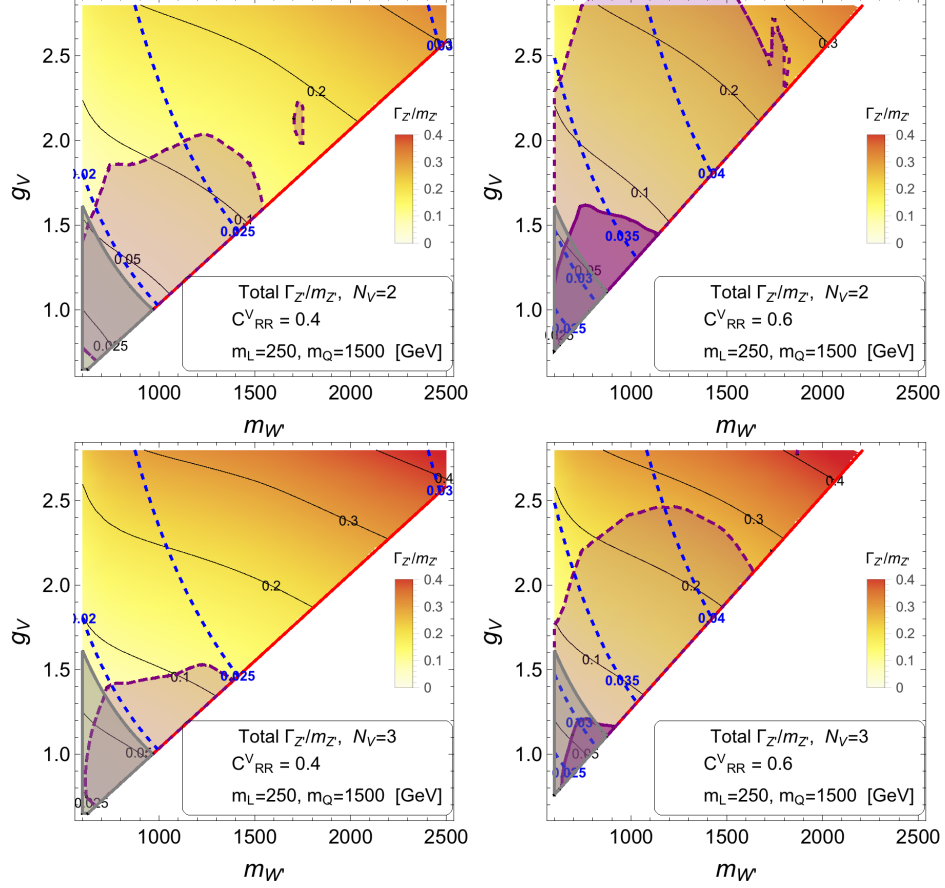


Figure 2.3: A summary of the bounds on our model. For the left (right) plots we are assuming $C_{RR}^V = 0.4$ ($C_{RR}^V = 0.6$), two benchmark values that can account for the $R_{D^{(*)}}$ anomaly. Those on the top (bottom) correspond to the case $N_V = 2$ ($N_V = 3$) generations of new vector-like fermions, only one of which has mixing with SM fermions. We are assuming all the new leptons (quarks) have $m_L = 250$ GeV ($m_Q = 1500$ GeV). The dashed blue curves denote the contours of constant η , while the solid black curves indicate contours of constant $\Gamma_{Z'}/m_{Z'}$. Points within the gray region have corrections to m_W which are outside 1σ observed range according to [69]. (The simple inequality in Eq. (2.30) explains the shape of the gray lines.) Bounds from [56] (obtained by recasting an older ATLAS search [77]) are indicated by the purple region (the colored region is ruled out) while a rough estimation of the bounds from a newer search [78] are denoted by dashed purple lines. As explained in the text, adding extra generations of vector-like matter alleviates the collider bounds.

g_V (holding fixed $m_{W'}$) we see that η increases slightly (it approaches its asymptotic value given in Eq. (2.32)), while the width increases more rapidly, as indicated in Eq. (2.33) – the coupling of Z' to SM fermions becomes stronger. So moving in this direction, the limit eventually disappears. Decreasing $m_{W'}$ at fixed g_V , we see that η decreases slightly due to subleading corrections in v_L/v_V . The width decreases more significantly, in part due to phase-space suppression, but also because to hold fixed C_{RR}^V , we see that the fermion mixings \mathcal{U}_{21} have to decrease according to Eq. (2.16). So we find that in this direction the limits grow stronger. The only exception is at very small $m_{W'}$, where according to the recast of Eq. (2.32), the limits disappear, presumably due to the kinematic thresholds of the LHC searches.

The results reported in [56] were obtained by recasting an older ATLAS search [77]. This was updated in [78]. Given that the limits in the new search on the cross-section are improved by a factor of ~ 3 , it is reasonable to assume that the η bounds on the grid of Fig. 2.3 will become a factor of $\sqrt{3}$ tighter. A crude estimate of the limits from the newer search [78] are shown as dashed lines in Fig. 2.3.

While the case $C_{RR}^V = 0.6$ seems to be fairly constrained (especially with the newer search as crudely estimated in Fig. 2.3), we observe that for $C_{RR}^V = 0.4$ the same region of the parameter space that is favored by EWP bounds is allowed by the limits on Z' . This region has the potential for discovery in upcoming LHC results.

2.4.3 Bounds on right-handed neutrinos

The right-handed neutrinos would be generated in the early Universe and so can be constrained by cosmology, assuming they are sufficiently long-lived. The lifetime depends on the right-left mixing. In a general model of right-handed neutrinos, the mass can arise from both a Dirac (M_D) and Majorana (M_N) mass term and the mixing angle θ is [94]

$$|\theta| \equiv \frac{M_D}{M_N}.$$

As seen in the mass matrix in Eq. (2.13), assuming a zero mass for left-handed neutrinos in the SM, there will be no mixing between the left-handed SM neutrinos and the new vector-like neutrinos at tree-level. Adding in the masses for the left-handed neutrinos contributes only a mixing at the level of $|\theta| \sim 10^{-20}$. However, even in the zero-mass limit for the left-handed neutrinos, there is no underlying symmetry prohibiting mixing at low energies. The dominant diagram giving rise to mixing between neutrinos is shown in Fig. 2.4. Other diagrams are significantly suppressed by the lack of tree-level mixing between ν_L and N_L in our model.

To estimate the contribution of this diagram we can assume the inner loop is a mass insertion between W - W' , proportional to $m_b \times m_c$. Then we approximate the diagram and divide it by the neutrino mass to get an estimation for its contribution to the mixing θ , as below

$$|\theta| \sim \frac{g_L^2 g_V^2 V_{cb}}{4(16\pi^2)^2} \frac{m_\tau m_b m_c}{m_{\nu_R} m_{W'} m_W}. \quad (2.34)$$

Inserting the range of masses and couplings in this equation suggests that our model prediction for θ is

$$|\theta| \sim 2 \times 10^{-5} \times \left(\frac{m_{\nu_R}}{1 \text{ keV}} \right)^{-1}, \quad (2.35)$$

Coupling a photon to one of the charged states in the mixing diagram results in the the loop-induced decay, $\nu_R \rightarrow \nu_L \gamma$, which has a lifetime [94, 95] of

$$\tau \approx (10^{30} \text{ s}) \left(\frac{m_{\nu_R}}{\text{keV}} \right)^{-3}. \quad (2.36)$$

The competing tree-level $\nu_R \rightarrow 3f\bar{f}$ (where f is any Standard Model fermion that couples to the Z and is kinematically accessible) requires a non-zero right-left mixing angle θ , and has a lifetime of

$$\tau \approx (10^{29} \text{ s}) \left(\frac{m_{\nu_R}}{\text{keV}} \right)^{-5} \left(\frac{\sin \theta}{2 \times 10^{-5}} \right)^{-2}. \quad (2.37)$$

where θ is the mixing parameter between right- and left-handed neutrinos. As seen in Eq. (2.35), the mixing angle is always small enough that we expect loop-induced

$\nu_R \rightarrow \nu_L \gamma$ decays to dominate, and the lifetime is generally large compared to the age of the Universe.

From this, we see that right-handed neutrinos below a GeV in mass are long-lived enough to be a component of dark matter (heavier ν_R are not viable replacements for the nearly-massless ν_L in the B -decays). Due to Z' -mediated pair-production and W' -mediated co-annihilation with τ leptons, the right-handed neutrinos would be thermally produced, in addition to any possible non-thermal production modes. These thermal processes would freeze-out around $T \sim 0.1 - 1$ GeV, shortly before the QCD phase transition. That is, the freeze-out occurs when the neutrinos are still relativistic. Such a dark matter candidate contributes a relic abundance directly proportional to its mass, with

$$\Omega h^2 \sim 10^{-1} [g_{*S}(T_f)]^{-1} \left(\frac{m_{\nu_R}}{\text{eV}} \right). \quad (2.38)$$

Assuming $T_f \sim 100$ MeV, $g_{*S} \sim 60$, and so m_{ν_R} must be less than 60 eV as to not saturate the dark matter density. This upper limit on the neutrino mass could be alleviated via non-standard cosmology, e.g. significant entropy injection [96, 95], but in any event, relativistic “hot” dark matter must constitute much less than 100% of the total [97], pointing toward an even lighter neutrino mass. A right-handed neutrino with a mass of ~ 10 eV is safe from these cosmological bounds without requiring dilution.

Assuming either $m_{\nu_R} \lesssim 60$ eV or significant entropy dilution which waters down this hot contribution to dark matter, the neutrinos act as a relativistic species. These affect the CMB power spectrum in a similar way as the SM left-handed neutrinos, shifting the time of matter-radiation equality and suppressing the power spectrum on small scales through free-streaming [98, 99]. The effect of N new neutrino-like light degrees of freedom which were in thermal equilibrium with SM at some point in their

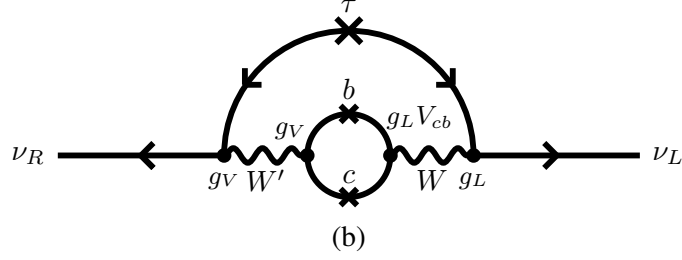


Figure 2.4: The only potentially dangerous loop-diagram mixing ν_R with the SM neutrinos. Other diagrams are suppressed by lack of tree-level mixing between left-handed fermions charged under different $SU(2)$ groups. Different sources of suppressions, e.g. loop factors, V_{cb} suppression, and heavy mediators, will make this diagram suppressed enough so that we can evade the bounds from neutrino mixing with light-enough new neutrinos.

history are usually quantified through the effective number of neutrinos:

$$\Delta N_{\text{eff}} = \left(\frac{g_*(T_\nu)}{g_*(T_{\nu_R})} \right)^{4/3} N, \quad (2.39)$$

where $g_*(T_\nu)$ and $g_*(T_{\nu_R})$ are the number of relativistic degrees of freedom at the time when SM neutrinos and right-handed neutrinos decoupled, respectively. Using $g_*(T_{\nu_R}) \sim 80$, and $g_*(T_\nu) \sim 10.7$, for our model, $\Delta N_{\text{eff}} \lesssim 0.07N$. The current experimental measurement is $N_{\text{eff}} = 3.12 \pm 0.23$ from baryon acoustic oscillations and CMB observations [100]. The SM prediction is $N_{\text{eff}} = 3.046$; therefore, we can easily accommodate up to three light right-handed neutrinos within 1σ of the cosmological bounds. Recall that only a single species of right-handed neutrino with small mixing to the left-handed neutrinos is required in our model.

2.4.4 Other bounds

Besides the bounds we have already discussed, there are other potential phenomenological constraints on our model. It is straightforward to see that our model can easily

evade the following bounds.

- **Flavor Constraints.** General mixing between the right-handed fermions could give rise to dangerous flavor-changing neutral currents. However, we have focused on a very specific mixing pattern that will suppress all the FCNCs due to Z' even beyond tree-level and only couples bc quarks through a W' , rendering the model immune to these flavor constraints. In particular, the severe bounds from neutral mesons mixing such as $K-\bar{K}$ or $B_s-\bar{B}_s$ mixing will not apply to our model since, due to lack of W' coupling to s quarks, there are no one-loop box diagrams that generate such a coupling. A recent summary of the most constraining flavor bounds for $R_{D^{(*)}}$ models can be found in [101]; we can easily see that most of these bounds are irrelevant for our model thanks to the specific fermion mixing that prohibits dangerous couplings. This pattern of couplings is *ad hoc* and is solely motivated by anomalies in bc interactions. It would be interesting to find a UV completion where these couplings were generated in a more natural way.

The only potential flavor constraints are those that need only a bc quark flavor-changing coupling. One such observable is B_c life-time. However, a symmetry similar to the one discussed in Sec. 2.2 applies to B_c life-time calculation and relates the contribution of C_{RR}^V to that of C_{LL}^V . As the latter is not constrained (by B_c life-time) for the range that explains $R_{D^{(*)}}$ [51], neither is the former.

- **Fermions coupling to Higgs.** Given the mixing of some SM fermions with new vector-like ones, they are effectively getting some of their mass from ϕ' instead of SM Higgs ϕ . This might raise the question of how much deviation will this phenomenon give rise to in the coupling of SM fermions to ϕ . After all, there are some constraining bounds on this deviation in the literature [102, 103]. However, the measured couplings are between ϕ and mass eigenstates and we

can essentially tune the couplings of fermions charged under $SU(2)_L$ to ϕ such that after integrating out all the heavy degrees of freedom the effective coupling (of mass eigenstates) matches the SM predictions.

- **LEP bounds.** Any vector mediator interacting with the first two generations of leptons can be subject to very stringent bounds from LEP data [104]. However, the fermion and gauge boson mixing in our model suppresses the coupling of Z' and W' to the first two generations, see Appendix B, so that (except for a small part of the parameter space in Fig. 2.3 that is already disfavored by m_W limits) we automatically evade these bounds.

2.5 Final Remarks

In this chapter we have considered an alternative, promising hypothesis concerning $R_{D(*)}$: that the anomalous measurements are the result of b quarks decaying to charm and tau leptons and a new, light right-handed neutrino. After first considering all possible effective operators which alter R_D and R_{D^*} involving both left- and right-handed neutrinos, we focus on one particular right-handed operator that has the potential to explain both anomalies simultaneously.

This single effective operator, $\mathcal{O}_{RR'}^V$, can result from integrating out a massive W' that must couple to $\tau_R \nu_R$ and $b_R c_R$. We embed this vector boson in an $SU(2)_V \times U(1)_X$ extension of the SM. However, in order to avoid an associated Z' with $1/V_{cb}$ enhanced couplings to bb , we do not charge the SM fermions under the $SU(2)_V$. Instead, we add a generation of vector-like fermions that mix with their right-handed SM counterparts. The only coupling between the right-handed chiral quarks and leptons and the W' and Z' occurs through this mixing. As we show, this model can explain both the R_D and R_{D^*} anomalies while respecting all existing collider, cosmological, and electroweak

precision bounds.

Our W' model makes several concrete predictions that will be tested in the upcoming LHC data. The W' and Z' are close in mass, and must be below ~ 2.5 TeV in order to fit the anomalies with perturbative gauge couplings. In order to avoid the LHC searches for $Z' \rightarrow \tau\tau$, we require a modestly wide Z' resonance ($\Gamma_{Z'} \sim 0.1m_{Z'}$). While this is safe from current limits with 30 fb^{-1} of integrated luminosity, the high-luminosity runs should be able to conclusively discover or exclude the majority of the viable parameter space. In addition, significant mixing with the right-handed quarks is achieved through vector-like quarks that are heavier than the existing limits (~ 1 TeV), but not beyond the kinematic reach of the LHC. The width of the Z' is achieved through relatively light (~ 250 GeV) vector-like leptons, which are also potentially accessible at the LHC.

Chapter 3

A New Solution Relying On C_{RL}^V

3.1 Motivation

As argued in Sec. 1.2, similar fluctuations as R_D and R_{D^*} have been observed in two other related observable, namely $R_{J/\psi}$ and $F_{D^*}^L$, see Sec. 1.2 for further details. While these seem to be interesting additions to the $R_{D^{(*)}}$ anomaly, they are in tension with not only the SM prediction, but also various new physics models that have been considered in the literature [26, 27, 29, 105, 106].¹ In fact, no model has been found to come even close to the observed values of $F_{D^*}^L$ or $R_{J/\psi}$.

So far, only minimal BSM models (single mediators) and simple combinations of WCs have been considered. Here, we will generalize the study of these observables to the full space of WCs for the dimension 6 effective Hamiltonian in Eq. (1.10).

We will show that (i) there are no combination of these operators that can explain the observed $R_{J/\psi}$, and (ii) one needs to generate the operator C_{RL}^V (or its equivalent with RH neutrinos, C_{LR}^V) in order to explain the observed $F_{D^*}^L$. In light of this result, we will build the first model in the literature generating this operator. This model is the first viable proposal for generating C_{RL}^V , thus, it should be a part of any explanations for the observed $F_{D^*}^L$.

Our model augments the SM by a pair of LQs. These two LQs can be embedded in a bifundamental of $SU(2) \times SU(2)$ custodial symmetry. Each of these LQs have

¹Ref. [107] considers the possibility of right-handed (RH) neutrinos as well and reports pairs of WCs that are claimed to explain the observed $R_{J/\psi}$. We were unable to reproduce their results in our calculations.

been studied before as a solution to these anomalies.

We will show that after the electroweak symmetry breaking these two new mediators can mix with each other. This mixing allows us to generate the C_{RL}^V operators from Eq. (1.10). We will further study various bounds from EWP tests, collider searches, and different flavor processes and show that our model can indeed generate a substantially large C_{RL}^V while respecting all these experimental bounds.

Finally, we will investigate the possibility of adding RH neutrinos to this setup. After the electroweak symmetry breaking our model can generate C_{LR}^V as well. This model is again the first viable model generating this WC. Nonetheless, we will show that it is not possible to generate both C_{RL}^V and C_{LR}^V simultaneously, owing to the severe constraints from the $b \rightarrow \nu\nu$ processes.

3.2 Explaining the Observed $F_{D^*}^L$

3.2.1 General setup

The observables of interest in this chapter are $\mathcal{O} = R_{J/\psi}, F_{D^*}^L, R_D, R_{D^*}, \text{Br}(B_c \rightarrow \tau\nu)$. The first four observables show discrepancies with the SM predictions, while the bounds on $\text{Br}(B_c \rightarrow \tau\nu)$ can be used to severely constrain various BSM explanations of these anomalies [49, 51, 50, 52]. Measurements of the total width of the B_c meson and $B_u \rightarrow \tau\nu$ decay have been used in [49, 51, 50] and [52] to put bounds of $\text{Br}(B_c \rightarrow \tau\nu) \lesssim 30\%$ and $\text{Br}(B_c \rightarrow \tau\nu) \lesssim 10\%$, respectively. Meanwhile the SM prediction is $\text{Br}(B_c \rightarrow \tau\nu) = 2.3\%$. We will use these three reference values for $\text{Br}(B_c \rightarrow \tau\nu)$ throughout the upcoming sections.

In our study of these observables, we use the numerical formulas in [105],

$$\begin{aligned}
R_D &= 0.299 (|C_{+L}^V|^2 + 1.02|C_{+L}^S|^2 + 0.9|C_{LL}^T|^2 \\
&\quad + \text{Re} [(C_{+L}^V)(1.49(C_{+L}^S)^* + 1.14(C_{LL}^T)^*)]) , \\
R_{D^*} &= 0.257 (0.95|C_{-L}^V|^2 + 0.05|C_{+L}^V|^2 + 0.04|C_{-L}^S|^2 + 16.07|C_{LL}^T|^2 \\
&\quad + \text{Re} [C_{-L}^V(0.11(C_{-L}^S)^* - 5.89(C_{LL}^T)^*)] + 0.77\text{Re} [C_{+L}^V(C_{LL}^T)^*]) , \\
R_{D^*} F_{D^*}^L &= 0.116 (|C_{-L}^V|^2 + 0.08|C_{-L}^S|^2 + 7.02|C_{LL}^T|^2 \\
&\quad + \text{Re} [(C_{-L}^V)(0.24(C_{-L}^S)^* - 4.37(C_{LL}^T)^*)]) , \\
\text{Br}(B_c \rightarrow \tau \nu) &= 0.023 (|C_{-L}^V|^2 + 4.33|C_{-L}^S|^2) ,
\end{aligned} \tag{3.1}$$

where we are defining $C_{\pm L}^S \equiv C_{RL}^S \pm C_{LL}^S$ and $C_{\pm L}^V \equiv C_{LL}^V \pm C_{RL}^V$. In deriving these formulas, the authors of [105] use the NLO results of the heavy quark effective theory from [108] for the hadronic matrix elements. Similar numerical formulas can be found in the literature, e.g. [109, 110, 42, 106].

We will be interested in calculating the following quantities:

$$\max F_{D^*}^L \Big|_{R_D, R_{D^*}, \text{Br}(B_c \rightarrow \tau \nu)}, \quad \max R_{J/\psi} \Big|_{R_D, R_{D^*}, \text{Br}(B_c \rightarrow \tau \nu)} \tag{3.2}$$

where the global maximum is taken over the full space of WCs with LH neutrinos (see the end of this section for a generalization to LH+RH neutrinos). This is a 10 real-dimensional space, making the maximization of $F_{D^*}^L$ and $R_{J/\psi}$ seem like a daunting, if not impossible task. Yet we will accomplish this task by leveraging several properties of the above numerical formulas:

- All these observables can be written as

$$\mathcal{O} = z_5^\dagger M_{\mathcal{O}} z_5 = x_5^T M_{\mathcal{O}} x_5 + y_5^T M_{\mathcal{O}} y_5, \tag{3.3}$$

where

$$z_5 = x_5 + iy_5 = (C_{-L}^V, C_{+L}^V, C_{-L}^S, C_{+L}^S, C_{LL}^T), \tag{3.4}$$

and the $M_{\mathcal{O}}$ matrices are real and positive semidefinite.

- There is one overall rephasing freedom in defining the WCs, i.e. by multiplying all the WCs by a common phase the prediction for these observables does not change.

Using these properties (in particular the first one), we can prove that the maxima (3.2) actually exist. We observe that the M_{R_D} and $M_{R_{D^*}}$ matrices in (3.3) have orthogonal null vectors corresponding to C_{-L}^S , C_{-L}^V and C_{+L}^S , respectively. Hence, fixing R_D and R_{D^*} results in a compact space in the full WC space. Any function on a compact space must have a maximum somewhere in that space.

We can also prove that the global maximum occurs at real values of the WCs (modulo the overall rephasing invariance). The proof uses the method of Lagrange multipliers. Let's define (for $\mathcal{O} = F_{D^*}^L$ and $R_{J/\psi}$):

$$\begin{aligned}\tilde{\mathcal{O}} &= \mathcal{O} - \lambda_1(R_D - R_D^{(0)}) - \lambda_2(R_{D^*} - R_{D^*}^{(0)}) - \lambda_3(\text{Br}(B_c \rightarrow \tau\nu) - \text{Br}(B_c \rightarrow \tau\nu)^{(0)}) \\ &= x_5^T(M_{\mathcal{O}} - \lambda_1 M_D - \lambda_2 M_{D^*} - \lambda_3 M_{B_c})x_5 \\ &+ y_5^T(M_{\mathcal{O}} - \lambda_1 M_D - \lambda_2 M_{D^*} - \lambda_3 M_{B_c})y_5 \\ &+ \lambda_1 R_D^{(0)} + \lambda_2 R_{D^*}^{(0)} + \lambda_3 \text{Br}(B_c \rightarrow \tau\nu)^{(0)}\end{aligned}\tag{3.5}$$

Setting the derivatives of $\tilde{\mathcal{O}}$ with respect to x_5 and y_5 to zero yields

$$(M_{\mathcal{O}} - \lambda_1 M_D - \lambda_2 M_{D^*} - \lambda_3 M_{B_c})x_5 = (M_{\mathcal{O}} - \lambda_1 M_D - \lambda_2 M_{D^*} - \lambda_3 M_{B_c})y_5 = 0 \tag{3.6}$$

The matrix $M_{\tilde{\mathcal{O}}} \equiv M_{\mathcal{O}} - \lambda_1 M_D - \lambda_2 M_{D^*} - \lambda_3 M_{B_c}$ must be degenerate for this equation to have non-trivial solutions. Yet we cannot tune the λ s to get more than one zero eigenvalue.² As a result, the null space is one-dimensional, which means x_5 and y_5 are parallel to each other. Using the rephasing invariance we can set $y_5 = 0$, i.e. the WCs at the global maximum can all be taken real.³

²A proof for generic matrices: in order for $M_{\tilde{\mathcal{O}}}$ to be rank less than 4, all of its first minors must be zero. There are 25 such minors, generically independent. So it is impossible to set them all to zero using just three parameters $\lambda_{1,2,3}$. We explicitly check that this argument is true for the matrix combination in (3.6).

³As a side note, we can check that the number of unknowns and number of equations match. There are three remaining constraints to satisfy, and three unknowns: λ_2 , λ_3 and the modulus of the null vector x_5 .

The proof trivially extends to the case of fixing a WC to a particular value. For instance, later we will be interested in fixing $|C_{RL}^V|$ to some value and maximizing the observables with respect to all the other WCs. In that case, we can simply add another quadratic constraint $|C_{RL}^V|^2 = (|C_{RL}^V|^2)^{(0)}$ to the mix and the above argument proceeds exactly as before.

So for the rest of this study we will restrict to real WCs without loss of generality. This reduces the parameter space from $10 \rightarrow 5$ real dimensional. With the three constraints $R_D = R_D^0$, $R_{D^*} = R_{D^*}^0$ and $\text{Br}(B_c \rightarrow \tau\nu) = B_c^0$ it amounts to maximizing in 2 real dimensions, or with an additional WC held fixed, in just 1 real dimension.

Finally, we comment on the generalization to LH+RH neutrinos. Since there is no interference between LH and RH neutrinos, all the numerical formulas in the presence of both types of neutrinos are of the form $z_5^\dagger M z_5 + \tilde{z}_5^\dagger M \tilde{z}_5$ where \tilde{z}_5 refers to the RH neutrino WCs [42]. So the Lagrange multiplier argument proceeds as before, and \tilde{z}_5 functions as “additional imaginary parts”, i.e. there is an enhanced $SO(4)$ symmetry at the global maximum that allows us to rotate x_5 , y_5 , \tilde{x}_5 and \tilde{y}_5 into one another. Thus the global maximum cannot be changed by including RH neutrinos and all of our conclusions derived below which assume only LH neutrinos will be robust.

3.2.2 Maximizing the observables: global maxima

After we have shown that the maximization problem can be restricted to the real parts of the (LH neutrino) WCs without loss of generality, the parameter space is already greatly reduced, and the remaining steps are straightforward if tedious. We perform a series of transformations to the WCs (rotations, shifts and rescalings) so that we can solve the constraints $R_D = R_D^0$, $R_{D^*} = R_{D^*}^0$ and $\text{Br}(B_c \rightarrow \tau\nu) = B_c^0$ analytically and simply. This allows the rest of the maximization (over just 2 real dimensions) to be handled numerically. We provide further details on these steps in App. C. Here we simply present the results.

C_{RL}^S	C_{LL}^S	C_{LL}^V	C_{RL}^V	C_{LL}^T	R_D	R_{D^*}	$F_{D^*}^L$	$R_{J/\psi}$	$\text{Br}(B_c \rightarrow \tau\nu)$
-0.669	-0.884	0.097	2.029	-0.329	0.407	0.304	0.620	0.406	0.023
-0.791	-0.739	0.118	1.977	-0.302	0.407	0.304	0.638	0.410	0.1
-0.972	-0.555	0.142	1.948	-0.298	0.407	0.304	0.662	0.412	0.3

Table 3.1: The combination of WCs that maximize $F_{D^*}^L$ for the global average of $R_{D^{(*)}}$ and with various values of $\text{Br}(B_c \rightarrow \tau\nu)$. All these combinations exhibit a large value of C_{RL}^V and C_{LL}^T ; the SM contribution of $C_{LL}^V = 1$ is also largely canceled.

C_{RL}^S	C_{LL}^S	C_{LL}^V	C_{RL}^V	C_{LL}^T	R_D	R_{D^*}	$F_{D^*}^L$	$R_{J/\psi}$	$\text{Br}(B_c \rightarrow \tau\nu)$
-0.659	-0.857	0.109	1.967	-0.286	0.407	0.304	0.620	0.409	0.023
-0.787	-0.726	0.124	1.948	-0.282	0.407	0.304	0.637	0.410	0.1
-0.967	-0.542	0.147	1.919	-0.277	0.407	0.304	0.660	0.413	0.3

Table 3.2: The combination of WCs that maximize $R_{J/\psi}$ for the global average of $R_{D^{(*)}}$ and with various values of $\text{Br}(B_c \rightarrow \tau\nu)$. Intriguingly, the WCs at the global maximum of $R_{J/\psi}$ exhibit very similar features to those at the global maximum of $F_{D^*}^L$.

Regarding the values of the WCs at the global maxima, there are a few interesting features. In particular, we find a large value of C_{RL}^V and C_{LL}^T ,⁴ and a substantial cancellation of the SM contribution to C_{LL}^V . These are in fact generic features we find in the combination of the WCs that maximize $F_{D^*}^L$ and $R_{J/\psi}$ for other values of $R_{D^{(*)}}$ and $\text{Br}(B_c \rightarrow \tau\nu)$ as well. This suggests that any NP origin of $F_{D^*}^L$ and $R_{J/\psi}$ may be nonminimal, in order to give rise to all of these WCs.

In Fig. 3.1, we find the maximum of $F_{D^*}^L$ or $R_{J/\psi}$ over all the WCs for different values of $\text{Br}(B_c \rightarrow \tau\nu)$ and $R_{D^{(*)}}$.

Meanwhile, we see that the observed value of $F_{D^*}^L$ is attainable everywhere in the

⁴Notice that all the existing models in the literature generate a tensor WC with association with a scalar WC of $C_{LL}^S \sim 8C_{LL}^T$ in the IR; hence, having $C_{LL}^T \sim 0.3$ in the IR implies scalar WCs of around 2.4.

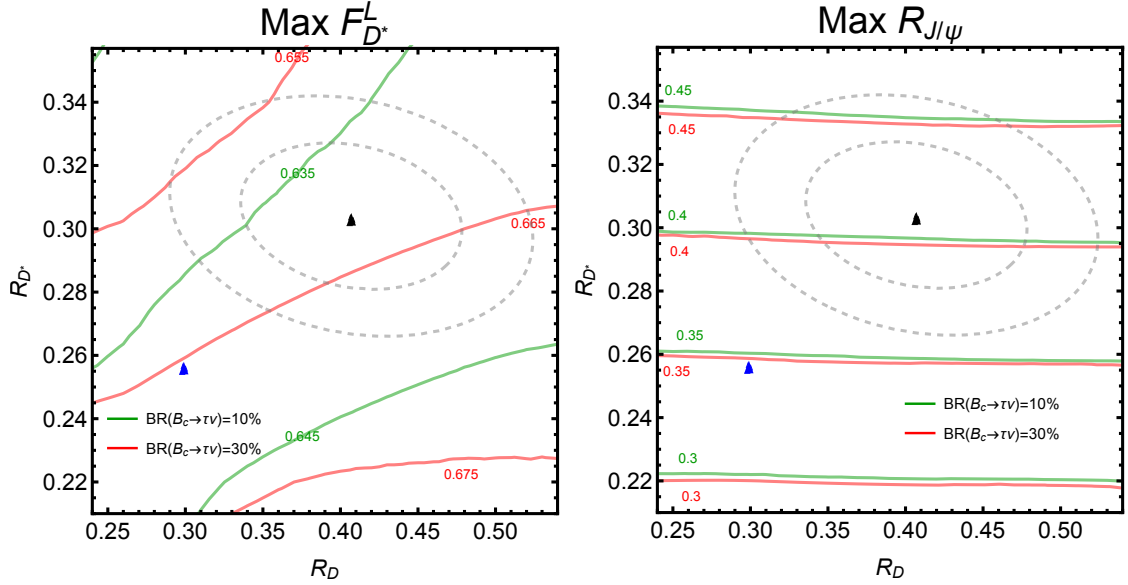


Figure 3.1: The maximum attainable $F_{D^*}^L$ (left) and the maximum attainable $R_{J/\psi}$ (right) for different values of $\text{Br}(B_c \rightarrow \tau \nu)$ and R_{D^*} . The green and red contours correspond to $\text{Br}(B_c \rightarrow \tau \nu) = 10\%$ and $\text{Br}(B_c \rightarrow \tau \nu) = 30\%$, respectively. The blue (black) triangle indicates the SM predictions (the world-averaged measured values) of R_{D^*} while the dashed gray ellipses are contours of 1 and 2 σ around the world-average measured values. These figures indicate that indeed there exists a combination of the WCs that can explain the observed value of $F_{D^*}^L$ from (1.7); yet, there are no combinations of these WCs that can reach the 1 σ range of the observed $R_{J/\psi}$ value in (1.5).

1 or 2σ ellipse of the measured world average R_D , R_{D^*} . However, no known models currently can give rise to such a large value of $F_{D^*}^L$ [105, 106]. This could be due to the fact that we seem to need a combination of all the WCs to have a large enhancement to $F_{D^*}^L$, as suggested by Tab. 3.1, which can not be achieved with any of the existing minimal models. It could also be due to the fact that enhanced $F_{D^*}^L$ seems to require a large value of C_{RL}^V , which is well-known to be challenging. We will discuss C_{RL}^V further in the next section.

3.2.3 Maximizing the observables: holding WCs fixed

We can also treat any of the WCs as a constant and go through a similar series of transformations as above, in order to maximize $F_{D^*}^L$ and $R_{J/\psi}$ when holding that WC fixed. This allows us to study that WC's contribution to $F_{D^*}^L$ and $R_{J/\psi}$ in further detail.

Going through the procedure above for all different WCs we find interesting results for the contributions of C_{LL}^T , C_{LL}^V , and C_{RL}^V to $F_{D^*}^L$. In Fig. 3.2 we show the maximum attainable value of $F_{D^*}^L$ as a function of these three WCs, and in Tab. 3.3 we report a few benchmark points maximizing $F_{D^*}^L$ for a fixed C_{RL}^V . These clearly suggest that in order to explain the observed $F_{D^*}^L$ in (1.7), we need non-zero values for all of these WCs from NP. In Fig. 3.2, if we go to larger values of the fixed WC in each plot, it becomes impossible to satisfy the constraints on $R_{D^{(*)}}$.

Most notably, Fig. 3.2 demonstrates that in order to explain the observed $F_{D^*}^L$ from (1.7), NP should give rise to sizable C_{RL}^V . There are currently no models in the literature generating this WC. In fact, there are strong general arguments against its existence. It violates $SU(2)_L$ and $U(1)_Y$ so it must be higher effective dimension (at least dimension 8).⁵

⁵As discussed in [111, 112], one can generate this operator at dimension 6 in SMEFT but only by integrating out an off-shell W ; since the couplings of the W to the leptonic side are flavor-universal, this can not explain our anomalies, which require some LFU violation.

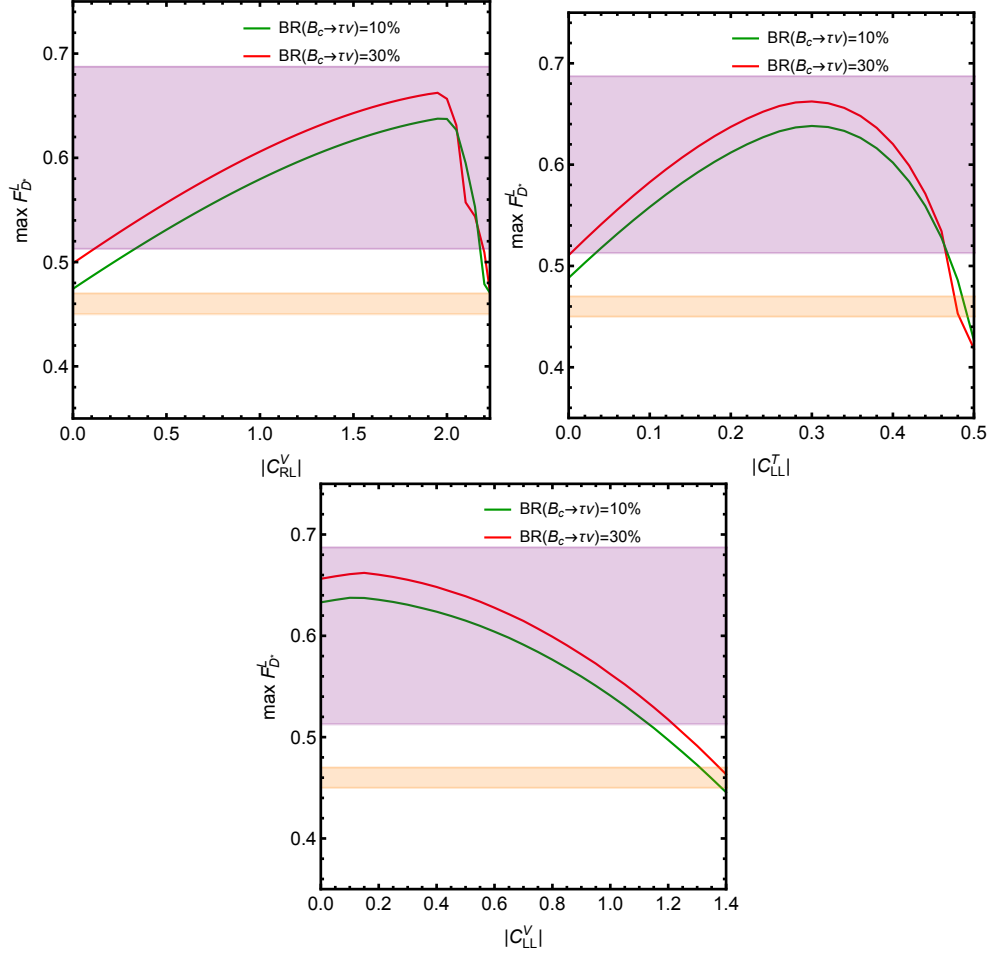


Figure 3.2: The maximum attainable F_D^L as a function of WCs C_{LL}^T , C_{RL}^V , or C_{LL}^V ; in each plot we marginalize over other WCs, given the constraints $R_D = 0.4$ and $R_{D^*} = 0.3$. The green and red curves correspond to $\text{Br}(B_c \rightarrow \tau \nu) = 10\%$ and $\text{Br}(B_c \rightarrow \tau \nu) = 30\%$, respectively. The purple (orange) band shows the 1σ error bar around the central observed value (SM prediction) of F_D^L . These figures highlight the necessity of NP with all of these WCs in order to explain the observed F_D^L .

C_{RL}^S	C_{LL}^S	C_{LL}^V	C_{RL}^V	C_{LL}^T	R_D	R_{D^*}	$F_{D^*}^L$	$R_{J/\psi}$	$\text{Br}(B_c \rightarrow \tau\nu)$
0.330	0.152	1.012	-0.3	0.092	0.400	0.300	0.510	0.340	0.1
0.481	0.321	0.890	-0.5	0.118	0.400	0.300	0.532	0.347	0.1
0.614	0.471	0.764	-0.7	0.143	0.400	0.300	0.552	0.355	0.1
0.785	0.665	0.567	-1	0.180	0.400	0.300	0.580	0.365	0.1

Table 3.3: Benchmark points that can reach the maximum $F_{D^*}^L$ with a particular C_{RL}^V and fixed $R_{D^{(*)}}$ and $\text{Br}(B_c \rightarrow \tau\nu)$. The $R_{J/\psi}$ with the same set of WCs is calculated as well; these values of $R_{J/\psi}$ are very close to the maximum attainable $R_{J/\psi}$ with the same C_{RL}^V , see fig. 3.3.

As we saw in Fig. 3.1, there is no point in the parameter space of the dimension 6 effective Hamiltonian consistent with the measured values of R_D and R_{D^*} that can explain the observed value of $R_{J/\psi}$. For completeness, we elaborate on this by studying the effect of each individual operator on $R_{J/\psi}$. The maximum $R_{J/\psi}$ attainable with fixed values of certain WCs is depicted in Fig. 3.3. We further include the prediction for $R_{J/\psi}$ with the WCs in Tab. 3.3 that maximize $F_{D^*}^L$ for any given C_{RL}^V ; these benchmark points can almost reach the maximum attainable $R_{J/\psi}$ as well.

3.3 A Model for C_{RL}^V

In light of the importance of C_{RL}^V in explaining $F_{D^*}^L$, in the rest of this chapter we propose a new LQ model that can generate this WC while being consistent with existing flavor, EWP and collider bounds. Our setup is the first model relying on C_{RL}^V to explain the $R_{D^{(*)}}$ anomalies.

To set the stage, we first report the range of the WC C_{RL}^V that can explain R_D and R_{D^*} up to 1σ of the current global average. This is depicted in Fig. 3.4. Here, we use the numerical formulas in [105] for the contribution of the LH neutrinos, which

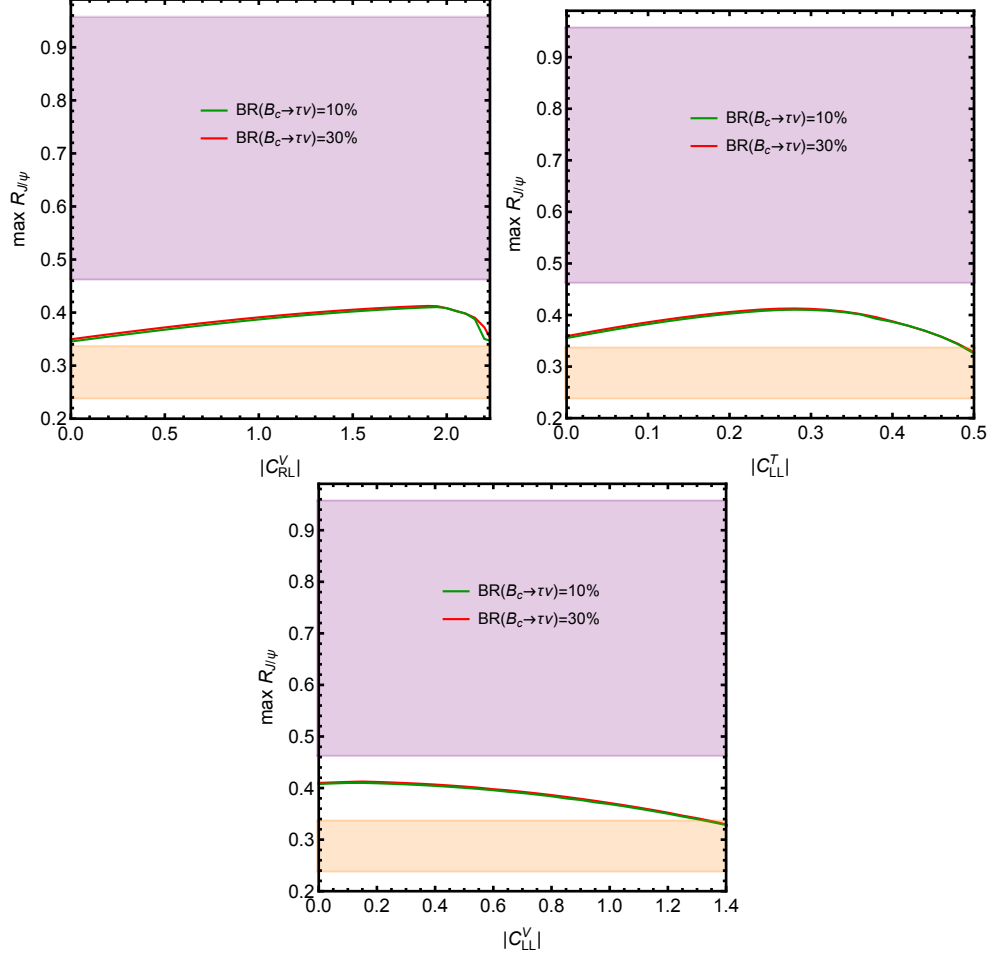


Figure 3.3: The maximum attainable $R_{J/\psi}$ as a function of WCs C_{LL}^T , C_{RL}^V , or C_{LL}^V ; in each plot we marginalize over other WCs. The colors and bands are as in fig. 3.2. We see that we can not even reach the 1σ range of the observed $R_{J/\psi}$ for any values of the WCs.

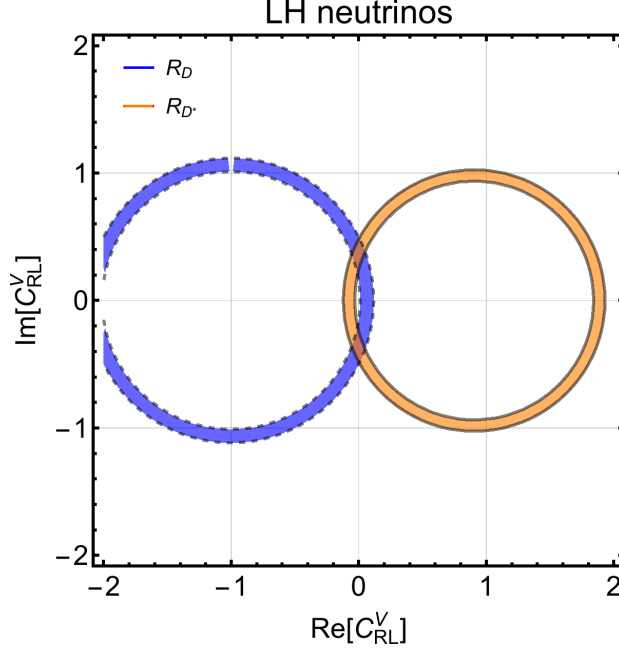


Figure 3.4: The contribution of C_{RL}^V to R_D and R_{D^*} . The orange and the blue bands denote the 1σ range from Eq. (1.3) for R_{D^*} and R_D , respectively.

include the NLO corrections in heavy quark effective theory from [108]. (Similar numerical formulas can be found in [109, 110, 42, 106]).

Since our mediators must couple to the Higgs field, the stringent constraints from EWPT, in particular the T parameter constraint, compel us to impose custodial symmetry on our model. We consider the symmetry group $G \equiv SU(3)_C \times SU(2)_L \times SU(2)_R \times U(1)_X$ which includes the $SU(2)_R$ custodial symmetry. The SM $U(1)_Y$ emerges from the $SU(2)_R \times U(1)_X \rightarrow U(1)_Y$ breaking. The $U(1)_X$ is introduced to realize LQs with appropriate $U(1)_Y$ charges.

The SM Higgs field can be written as $\mathcal{H} \equiv (\tilde{H}, H)$ where $\tilde{H} \equiv i\sigma_2 H^*$ and transforms as $(1, 2, 2)_0$ under the group G .

We introduce a scalar LQ, $\mathcal{R} \equiv (\tilde{R}_2, R_2)$ which transforms as $(3, 2, 2)_{2/3}$ under the group G . Here, two components of $SU(2)_R$, R_2 and \tilde{R}_2 , are doublets of $SU(2)_L$. We use the notation of [113] for these LQs. After the $SU(2)_R \times U(1)_X \rightarrow U(1)_Y$ breaking

the charge assignment of the new particles under the SM $SU(3) \times SU(2)_L \times U(1)_Y$ gauge group is $R_2 = (3, 2, 7/6)$ and $\tilde{R}_2 = (3, 2, 1/6)$,

$$R_2 = \begin{pmatrix} R_2^{5/3} \\ R_2^{2/3} \end{pmatrix}, \quad \tilde{R}_2 = \begin{pmatrix} \tilde{R}_2^{2/3} \\ \tilde{R}_2^{-1/3} \end{pmatrix}, \quad (3.7)$$

where the superscripts indicate the electric charges of different scalars in each $SU(2)_L$ doublet.

The $SU(2)_L \times SU(2)_R$ transformations for \mathcal{R} and \mathcal{H} are expressed as

$$\mathcal{H} \rightarrow U_L \mathcal{H} U_R^\dagger, \quad \mathcal{R} \rightarrow U_L \mathcal{R} U_R^\dagger, \quad (3.8)$$

where $U_{L,R}$ are $SU(2)_{L,R}$ rotations respectively.

The relevant terms in the Lagrangian of the model are

$$\mathcal{L} \supset \mathcal{L}_R + \mathcal{L}_{HR} + \mathcal{L}_{FR}, \quad (3.9)$$

where

$$\begin{aligned} \mathcal{L}_R &= |\partial R_2|^2 + |\partial \tilde{R}_2|^2 - M_{R_2}^2 |R_2|^2 - M_{\tilde{R}_2}^2 |\tilde{R}_2|^2, \\ \mathcal{L}_{HR} &= \lambda_R \text{Tr}(\mathcal{R}^\dagger \mathcal{H}) \text{Tr}(\mathcal{H}^\dagger \mathcal{R}) \\ &= \lambda_R \left\{ |R_2^\dagger H|^2 + |\tilde{R}_2^\dagger \tilde{H}|^2 + (\tilde{R}_2^\dagger \tilde{H} H^\dagger R_2 + \text{h.c.}) \right\}, \\ \mathcal{L}_{FR} &= g_1^{ij} \bar{u}_R^i R_2 \epsilon L^j + \tilde{g}_1^{ij} \bar{L}^j \epsilon \tilde{R}_2^\dagger d_R^i + \text{h.c.}, \end{aligned} \quad (3.10)$$

where ϵ is the anti-symmetric tensor with two $SU(2)_L$ indices and i and j are quark and lepton flavor indices, respectively. The first line of Eqs. (3.10) contain the mass terms M_{R_2} , $M_{\tilde{R}_2}$ for the LQs R_2 and \tilde{R}_2 . In our model the mass of the LQs of electric charge $5/3$ and $-1/3$ are equal to M_{R_2} and $M_{\tilde{R}_2}$, respectively. Although the custodial symmetry requires $M_{R_2} = M_{\tilde{R}_2}$, we assume they are different in general as a difference can be given rise to by any source of custodial symmetry breaking. We will discuss this point below. The quartic term in the second line respects the custodial symmetry. We can also write down single trace terms, $\text{Tr}(\mathcal{H} \mathcal{R}^\dagger \mathcal{R} \mathcal{H}^\dagger)$ and

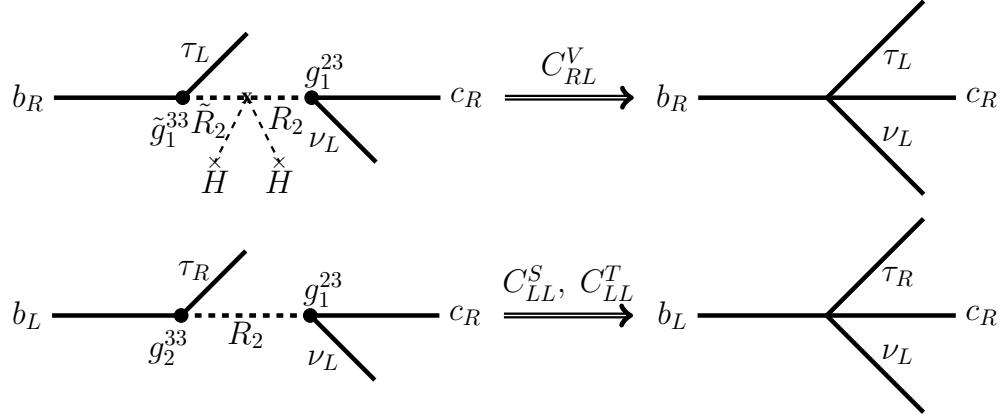


Figure 3.5: The diagrams generating C_{RL}^V (1st row) and C_{LL}^S, C_{LL}^T (2nd row) WCs in our model. After integrating the mediators out and Fierz transformation, the WC in Eqs. (3.13) is generated. The operator \mathcal{O}_{RL}^V is proportional to the mixing between the LQs. The relevant couplings from Eq. (3.10) are shown for each diagram.

$\text{Tr}(\mathcal{H}\mathcal{H}^\dagger\mathcal{R}\mathcal{R}^\dagger)$, but it is only relevant for us that these terms shift four leptoquark masses universally. This effect can be absorbed by the mass terms in the first line, so we ignore them in the following discussions. The last line contains the LQ couplings to the SM fermions and explicitly breaks the custodial symmetry.

A similar model without the extended symmetry had been used in the past [114] to explain two anomalies in the HERA experiment [115, 116]. It should be noted that each of these LQs have individually been proposed as solutions to $R_{D^{(*)}}$ in the past, see e.g. [68, 62], but our setup is the first model using their mixing to produce C_{RL}^V .

3.3.1 Generation of C_{RL}^V

After the EWSB, $R_2^{2/3}$ and $\tilde{R}_2^{2/3}$ mix via the third term in \mathcal{L}_{HR} . The mass matrix of the $R_2^{2/3}$ and $\tilde{R}_2^{2/3}$ is given by

$$M_{2/3}^2 = \begin{pmatrix} M_{R_2}^2 - \lambda_R v^2 & -\lambda_R v^2 \\ -\lambda_R v^2 & M_{\tilde{R}_2}^2 - \lambda_R v^2 \end{pmatrix}, \quad (3.11)$$

where v is the Higgs vev $v \approx 246\text{GeV}$. We can diagonalize this matrix by the rotation,

$$\begin{pmatrix} R_l \\ R_h \end{pmatrix} = \begin{pmatrix} \cos \varphi & -\sin \varphi \\ \sin \varphi & \cos \varphi \end{pmatrix} \begin{pmatrix} R_2^{2/3} \\ \tilde{R}_2^{2/3} \end{pmatrix}. \quad (3.12)$$

Both mass eigenstates R_l and R_h inherit a coupling to both RH and LH fermions of the SM after this rotation. After rewriting \mathcal{L}_{FR} in terms of these mass eigenstates and integrating them out at tree-level, we can generate the operator $(\bar{\tau}P_R b)(\bar{c}P_L \nu)$. After Fierz transformation this operator morphs into \mathcal{O}_{RL}^V with its WC given by

$$C_{RL}^V = -\frac{v^2}{4V_{cb}} g_1^{23} \tilde{g}_1^{33} \cos \varphi \sin \varphi \left(\frac{1}{M_{R_h}^2} - \frac{1}{M_{R_l}^2} \right), \quad (3.13)$$

where M_{R_l} and $M_{R_h}(> M_{R_l})$ are the mass eigenvalues corresponding to the eigenstates R_l and R_h in Eq. (3.12), respectively. The process of integrating out these mediators to generate C_{RL}^V is depicted in Fig. 3.5. At the leading order of v^2 , we can approximately obtain

$$\begin{aligned} C_{RL}^V &\approx -\frac{\lambda_R}{4V_{cb}} g_1^{23} \tilde{g}_1^{33} \frac{v^4}{M_{R_2}^2 M_{\tilde{R}_2}^2} \\ &\approx -0.47 \times \left(\frac{\lambda_R}{5} \right) \left(\frac{g_1^{23}}{1.3} \right) \left(\frac{\tilde{g}_1^{33}}{1.3} \right) \\ &\quad \times \left(\frac{M_{R_2}}{800 \text{ GeV}} \right)^{-2} \left(\frac{M_{\tilde{R}_2}}{800 \text{ GeV}} \right)^{-2}. \end{aligned} \quad (3.14)$$

We can see that there is an extra $v^2/\Lambda_{\text{NP}}^2$ suppression in this WC. The range of the WC C_{RL}^V that can explain R_D and R_{D^*} shown in Fig. 3.4 can be realized. We may wonder if the required size of λ_R is too large, but this is a scalar quartic coupling and the threshold for nonperturbativity is $\sim 16\pi^2$ (instead of $\sim 4\pi$ for Yukawa and gauge couplings) [117].

3.3.2 Other WCs

Let us briefly comment on other possible WCs which our LQs can generate. Under the SM gauge symmetry, the two LQs can further give rise to the following interactions

$$\mathcal{L} \supset g_2^{ij} \bar{e}_R^j Q_L^i R_2^\dagger + \text{h.c.}, \quad (3.15)$$

where again i and j are quark and lepton flavor indices, respectively. With these couplings and the couplings in (3.10), the LQ R_2 (\tilde{R}_2) can individually generate the WCs $C_{LL}^S = 4C_{LL}^T$ at the LQ scale [68, 62]:

$$C_{LL}^S = -\frac{v^2}{4V_{cb}} g_1^{23} g_2^{33} \left(\frac{\sin^2 \varphi}{M_{R_h}^2} + \frac{\cos^2 \varphi}{M_{R_l}^2} \right). \quad (3.16)$$

It should also be noted that different WCs in Eqs. (3.13) and (3.16) depend on different pairs of the couplings in Eq. (3.10) and (3.15), as indicated in Fig. 3.5. Since these WCs have been extensively explored in the literature, we do not further discuss these operators in our present model.

Further WCs can be generated if a new RH neutrino is added to our setup. We investigate this possibility in Sec. 3.5.

3.3.3 A cutoff scale

Since the required size of λ_R to generate C_{RL}^V is rather large, we need to see where such a λ_R coupling and the Higgs quartic coupling λ blow up and our effective theory breaks down. The dominant contributions to the one-loop renormalization group equations of λ and λ_R are given by

$$\begin{aligned} \mu \frac{d}{d\mu} \lambda &= \frac{1}{16\pi^2} (12\lambda^2 + 18\lambda_R^2), \\ \mu \frac{d}{d\mu} \lambda_R &= \frac{1}{16\pi^2} (\lambda\lambda_R - 4\lambda_R^2). \end{aligned} \quad (3.17)$$

The $SU(3)_C$ color factor gives an enhancement for the coefficient of the leptoquark contribution to the running of the Higgs quartic coupling λ . With this large coefficient and a large initial value of λ_R , the Higgs quartic first hits a Landau pole. Here, even the top quark contribution is subdominant and not shown. Assuming $\lambda_R \sim 5$ at the LQ mass scale, the Landau pole is $\mathcal{O}(10)$ TeV. Therefore, some UV completion of our model must appear at $\mathcal{O}(10)$ TeV or below. We comment on its possibility in the last section.

The cutoff scale of $\sim \mathcal{O}(10)$ TeV is also independently hinted at from considerations of fine-tuning. Since a new scalar particle with sizable couplings to the SM fermions is introduced, we encounter a new hierarchy problem as in the case of the SM Higgs field. Loops of the SM fermions can generate masses,

$$\delta M_{R_2}^2 \sim \frac{g_1^2 \Lambda^2}{16\pi^2}, \quad \delta M_{\tilde{R}_2}^2 \sim \frac{\tilde{g}_1^2 \Lambda^2}{16\pi^2}, \quad (3.18)$$

where Λ is a cutoff scale of the model. To avoid a significant fine-tuning, we should assume $\Lambda \lesssim \mathcal{O}(10)$ TeV.

Note that the radiative corrections to $M_{R_2}^2$ and $M_{\tilde{R}_2}^2$ do not respect the custodial symmetry, which is the reason why we do not assume the same mass for R_2 and \tilde{R}_2 in the first line of Eq. (3.10). Then, this source of custodial symmetry breaking contributes to a nonzero T parameter which we will estimate in the next section. Meanwhile, the quartic coupling λ_R is rather stable against custodial-symmetry-breaking radiative corrections, because relevant diagrams to generate C_{RL}^V involve the light quark Yukawa couplings. Then, if we keep the g_1^{33} coupling small, we can ignore custodial symmetry breaking in the quartic coupling.

3.4 Phenomenology

In this section we discuss the rich phenomenology in our model. We explore EWPT and collider bounds as well as flavor constraints and finally we identify the viable parameter space.

3.4.1 Flavor constraints

We here briefly comment on flavor constraints and the viability of our model. The branching ratio of $B_c \rightarrow \tau \nu$ can constrain the NP explaining the anomalies [49, 51, 50, 52]. The enhancement to this branching ratio is given by

$$Br(B_c \rightarrow \tau \nu) = 0.023 |C_{-L}^V + 4.33 C_{-L}^S|^2, \quad (3.19)$$

where we have defined $C_{\pm L}^S \equiv C_{RL}^S \pm C_{LL}^S$ and $C_{\pm L}^V \equiv C_{LL}^V \pm C_{RL}^V$. The most severe bound is at $\text{Br}(B_c \rightarrow \tau\nu) \leq 10\%$ [52]. This bound is most constraining when the NP only gives rise to scalar operators; it does not rule out the scenario of only C_{RL}^V . However, if we try to generate other WCs such as C_{LL}^S and C_{LL}^T , the bounds from this observable may become relevant.

Another constraint is from the flavor-changing $b \rightarrow s\nu\nu$ process [118, 119, 68, 120, 101]. Yet, the couplings required for C_{RL}^V do not contribute to this process.

Unlike C_{RL}^V , the WCs involving RH neutrinos are severely constrained from various flavor physics processes. We will further comment on these bounds in Sec. 3.5.

Lastly, it should also be noted that our LQs do not have any diquark terms that give rise to disastrous proton decays [113].

All in all, we observe that our model can generate a C_{RL}^V to explain the anomalies without any constraints from the flavor physics processes.

3.4.2 EWPT

The coupling between the new LQs and the Higgs field can contribute to the oblique parameters like S and T [121]. The T parameter constrains the assumption of $M_{\tilde{R}_2} \neq M_{R_2}$ in our model. The S parameter can put a strong constraint on the model parameter space regardless of custodial symmetry breaking.

The contributions to the S and T parameters in the present model have been studied in [122, 123]. We follow their results to translate the current bounds on these oblique parameters [3] into bounds on the parameters of our model. When we expand the expressions of the S and T parameters in terms of v^2 and then expand them also by the difference of the mass-squared parameters, $\Delta M^2 \equiv M_{\tilde{R}_2}^2 - M_{R_2}^2$, at the leading

order of these expansion parameters, we obtain

$$\begin{aligned}\Delta S &\approx -\frac{\lambda_R v^2}{2\pi M^2}, \\ \Delta T &\approx \frac{\lambda_R^2 v^2}{40\pi^2 \alpha} \frac{(\Delta M^2)^2}{M^6},\end{aligned}\tag{3.20}$$

where α is the fine-structure constant and $M^2 \equiv (M_{R_2}^2 + M_{\tilde{R}_2}^2)/2$ is the average of the mass-squared parameters. When we assume some value of M , the value of λ_R has an upper bound from the S parameter constraint and the degree of fine tuning in $\Delta M^2/M^2$ can be estimated from the T parameter constraint.

The constraints on the S and T parameters are described by an elliptic contour as shown in [3]. Since the sign of ΔS in (3.20) is negative with a positive λ_R , we here take the bounds as $|\Delta S| \lesssim 0.1$ and $\Delta T \lesssim 0.1$. Then, we obtain

$$\begin{aligned}\lambda_R &\lesssim 6.6 \times \left(\frac{|\Delta S|}{0.1}\right) \left(\frac{M}{800 \text{ GeV}}\right)^2, \\ \frac{\Delta M^2}{M^2} &\lesssim 0.35 \times \left(\frac{\Delta T}{0.1}\right)^{1/2} \left(\frac{\lambda_R}{5}\right)^{-1} \left(\frac{M}{800 \text{ GeV}}\right).\end{aligned}\tag{3.21}$$

We can see that the constraints are mild. The precise bounds are shown in Fig. 3.8. In this plot, we use the full expressions of the S and T parameters given in [122, 123] and the elliptic curve bounds on the oblique parameters [3]. As we diverge from the $M_{R_2} = M_{\tilde{R}_2}$ line the custodial symmetry is broken more severely and the bounds from the T parameter become more constraining. We still find a large available parameter space in this scenario as well.

3.4.3 Collider bounds

Given the extra $v^2/\Lambda_{\text{NP}}^2$ suppression in Eq. (3.14), even with a large quartic coupling λ_R , we need a sub-TeV LQ so as to generate a large enough C_{RL}^V . Since LQs are colored particles, extensive LHC searches give stringent bounds on these particles.

The signature of a light LQ can be looked for in direct pair production (PP) [124–128, 110, 129–131] and single production (SP) [132, 129], monojet [133, 129], and

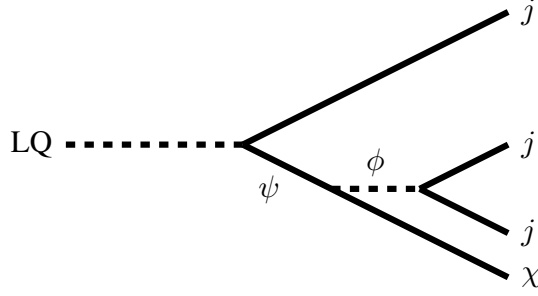


Figure 3.6: An example of a new decay channel for the LQ. This new channel allows the LQ to evade the *reducible* bounds. The new particles ψ and ϕ should be chosen almost degenerate in mass such that the missing particle χ is very soft and is not treated as MET in the searches. The final signature is three jets per LQ.

generic SUSY searches [134–142]. The bounds from these searches can rule out LQ masses below a TeV [110, 129]. However, these collider constraints are all *reducible*, meaning we can circumvent them by introducing a large branching ratio for each LQ into other final states [110] undetectable in various searches. As an example of such a channel we can consider the LQ decaying to three jets and a very soft (unmeasured) missing E_T (MET), see Fig. 3.6. This signature emulates the idea of stealth SUSY to hide signatures of the superpartners [143–145]. That is, we assume a sizable coupling of the LQ to a quark and a new color-neutral fermion ψ . The new fermion ψ subsequently decays to an electrically-neutral light fermion χ , which can be a dark matter candidate, and a scalar ϕ with appropriate SM charges. The key point is that the masses of the fermion ψ and the scalar ϕ are almost degenerate. Then, the momentum of χ in the rest frame of ψ is approximately given by $\Delta m \equiv m_\psi - m_\phi$. Taking account of a Lorentz boost factor in the laboratory frame, the amount of MET is estimated as $\sim (M_1/m_\psi)\Delta m$ and suppressed. The scalar ϕ is assumed to decay back to a pair of jets. In total, the LQ gives a signature with three jets and a very soft MET which is assumed here.

Description	Experiment	(ir)reducible	Diagrams
Direct LQ searches for $b\tau$ final state	ATLAS-35.9 fb ⁻¹ [131]	<i>reducible</i>	
Generic SUSY searches with MET	CMS-35.9 fb ⁻¹ [134, 136]	<i>reducible</i>	
Interference with the SM DY	ATLAS-36.1 fb ⁻¹ [129, 78]	<i>irreducible</i>	

Table 3.4: The searches which give the most constraining reducible and irreducible bounds and the relevant diagrams.

Our LQs also have an *irreducible* interference with the Drell-Yan (DY) processes of the SM through a t-channel diagram [56, 146, 147, 78, 110, 129]. Unlike reducible bounds mitigated by a new decay channel, the bounds from these processes are not alleviated by the new channel, hence *irreducible*.

Another potential *irreducible* signal is $bc \rightarrow \tau\nu$ studied in [148]. However, this study shows that the bounds from this process are not yet strong enough to constrain light LQs like the ones in our model.

We will discuss reducible and irreducible bounds below. For each case, the most stringent LHC searches and our simulation details are summarized.

Reducible bounds

In studying reducible bounds, we focus on one light LQ and decouple the other three. The lightest LQ comes from one of the states with electric charge 2/3 and couples to $b\tau$ and $c\nu$. The most constraining searches for this particle are summarized in the first and second rows of Tab. 3.4. For reducible bounds, they are direct LQ searches for the $b\tau$ final state and generic SUSY searches with MET. Direct LQ searches for the

$c\nu$ final state and SP and monojet searches give weaker bounds and are not shown in the table. The new channel depicted in Fig. 3.6 has been looked for in the context of RPV SUSY [149]; yet, the current bounds on the production cross-section are a factor of a few higher than the production cross-section of our LQ. We expect the next update of the aforementioned searches to probe parts of the currently available parameter space.

In studying generic SUSY searches with MET, we use MadGraph [83] and PYTHIA8 [150] for event generation and Delphes [151] for detector simulation. We here assume the masses of the particles in the new decay channel as $m_\psi = 300 \text{ GeV}$, $m_\phi = 295 \text{ GeV}$ and $m_\chi = 1 \text{ GeV}$ so that MET is sufficiently suppressed. We recast the most relevant CMS SUSY searches [134, 136] by using the code-base developed in [152] and find their limits on the lightest LQ. Some of these searches have recently been updated with the new LHC data, e.g. [142]; we leave a recast of these new searches and their effects on our model for a future study.

We show the reducible bounds on $\text{Br}(\text{LQ} \rightarrow b\tau)$ and $\text{Br}(\text{LQ} \rightarrow c\nu)$ from direct LQ searches and SUSY searches in Fig. 3.7. The figure indicates the region of the branching ratio into $b\tau$ or $c\nu$ that is allowed for different LQ masses; other than these two channels, we assume the LQ only decays to the new stealthy channel in Fig. 3.6. As we go to a larger branching ratio into $b\tau$ or $c\nu$, the LQ search targeting that final state becomes more constraining. As the SUSY searches target final states with MET, when the branching ratio into the new three jet channel increases, i.e. the bottom-left of the figure, the bounds from the SUSY searches are loosened and a light LQ mass is available. We see that with a large enough branching ratio into the new three jet channel we can have the LQ as light as 650 GeV, which is light enough to generate a large C_{RL}^V . The figure also indicates that most of the remaining branching ratio should be attributed to the $b\tau$ channel in order to evade the bounds.

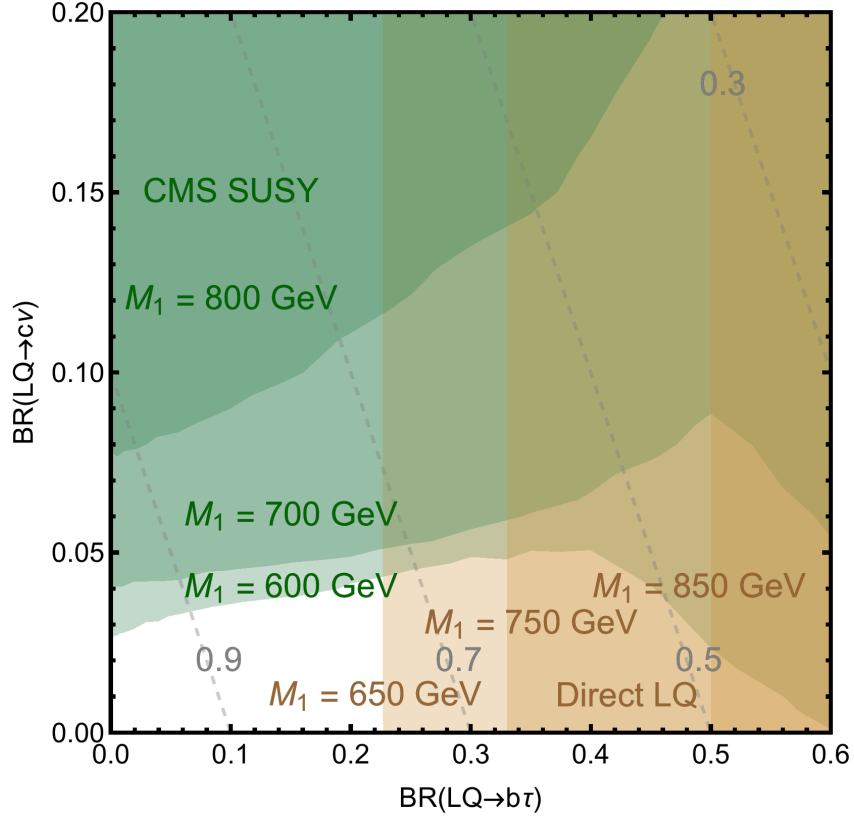


Figure 3.7: The bounds on $Br(LQ \rightarrow b\tau)$ and $Br(LQ \rightarrow c\nu)$ from direct LQ searches (brown) and SUSY searches (green). We include the LQ mass M_1 of 650 GeV, 750 GeV, and 850 GeV. For each LQ mass, the colored region is excluded. The (gray) dashed lines denote the branching ratio of the new decay channel.

It is straightforward to see

$$\text{Br}(\text{LQ} \rightarrow b\tau) / \text{Br}(\text{LQ} \rightarrow c\nu) = (\tan \varphi \tilde{g}_1^{33} / g_1^{23})^2, \quad (3.22)$$

thus we can modify the branching ratio into these two channels via the yukawa couplings g and \tilde{g} or by adjusting the mixing angle φ .

There are further SUSY searches that can constrain our model as well. In particular, [153] can in principle be used to constrain the branching ratio to $b\tau$. However, this search only looks for events with large m_T to cut on the SM background; this will actually discard the signal from our model as it gives rise to SM like m_T . We also recasted a few other SUSY searches [135, 137–141] using the code-base developed in [152]; we find that the bounds from these searches are sub-dominant to those from [134, 136] included in Fig. 3.7.

Irreducible bounds

Our LQs also have an *irreducible* interference with the Drell-Yan (DY) processes of the SM through t-channel diagrams [56, 146, 147, 78, 110, 129]. See the bottom row of Tab. 3.4. Unlike reducible bounds mitigated by a new stealthy decay channel, the bounds from these processes are not alleviated by the new channel. In [129] a search strategy is devised to look for this signature. We use their result to estimate the bounds on our model. As [129] only reports the bound relevant for the lightest LQ coupling to $b\tau$, we incorporate a Parton Distribution Function (PDF) factor to scale the cross section and calculate the bound on the heavier LQ with electric charge $5/3$ coupling to $c\tau$. We show the irreducible constraints from DY processes in Fig. 3.8.

3.4.4 Benchmarks

Fig. 3.8 summarizes all the constraints (EWPT, reducible bounds and irreducible bounds) and identifies the viable parameter space of $M_{R_2} = M^{5/3}$ and $M_{\tilde{R}_2} = M^{-1/3}$.

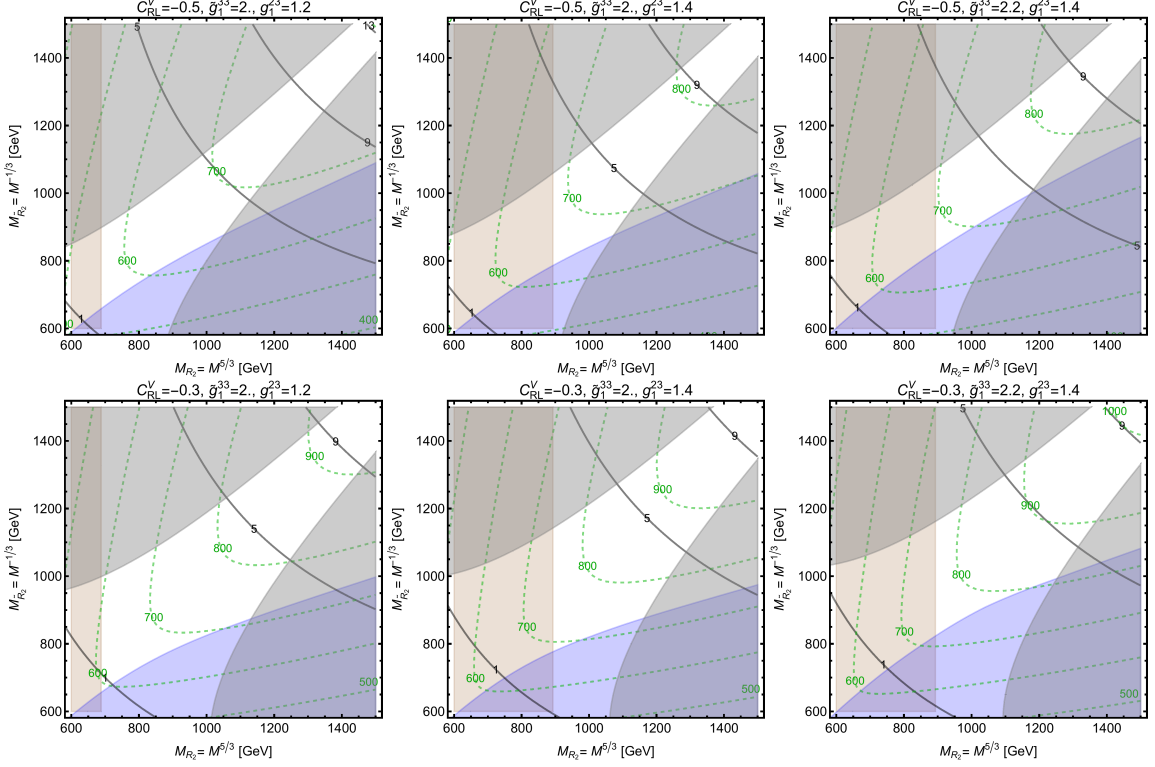


Figure 3.8: The constraints on the plane of $M_{R_2} = M^{5/3}$ and $M_{\tilde{R}_2} = M^{-1/3}$ from EWPT (gray regions) and DY irreducible bounds for $c\tau$ (brown) and $b\tau$ (blue). We keep the WC C_{RL}^V and the couplings \tilde{g}_1^{33} and g_1^{23} fixed on each plot. Then, λ_3 (black curves) and the lighter mass eigenstate of charge 2/3 LQs (green) are determined. For reducible bounds, we assume the coupling into the new channel is 4π , i.e. maximum allowed by unitarity arguments; with this coupling, the BR into the new decay channel from Fig. 3.6 dominates and all the reducible bounds are sub-dominant to the EWPT and DY bound. The white region is allowed.

In this figure, we fix the WC C_{RL}^V and the couplings \tilde{g}_1^{33} and g_1^{23} . The value of λ_R is determined from the values of M_{R_2} , $M_{\tilde{R}_2}$, C_{RL}^V , and the g couplings. Once λ_R is fixed, the masses of charge 2/3 LQs are determined as well. From the figure, we observe that with the help of (1) a new decay channel, like Fig. 3.6, without MET, (2) proper branching ratios of the lightest LQ decays into $b\tau$ or $c\nu$, attainable by adjusting the ratio $\tilde{g}_1^{33}/g_1^{23}$, and (3) the lightest LQ at 600 GeV or higher, we can evade various

collider and EWPT bounds and still explain the anomalies. As a further proof of this claim, in Tab. 3.5 we report a few benchmark points in the parameter space of our model that respects all these bounds and generates a large $|C_{RL}^V|$. Although the EWPT constraints are mild, we here concentrate on the case of $M_{R_2} = M_{\tilde{R}_2}$ which gives a maximum mixing for the LQs of electric charge 2/3.

3.5 Comments on RH Neutrinos

Finally, let us briefly comment on the possibility of generating operators with RH neutrinos in our setup.

We here show that our setup can generate a non-zero C_{LR}^V by introducing RH neutrinos coupled to our LQ but various bounds from flavor physics prevent a simultaneous generation of both C_{RL}^V and C_{LR}^V .

One of the $SU(2)_L$ doublet LQs can further give rise to the following interactions,

$$\mathcal{L} \supset \tilde{g}_2^i \tilde{R}_2 \bar{Q}_L^i \nu_R + \text{h.c.}, \quad (3.23)$$

where again i is the quark flavor index and ν_R is a new SM singlet RH neutrino. Similar to the earlier discussion on C_{RL}^V , it can be shown that these couplings and the

$M_{R_l}[\text{GeV}]$	$M_{R_h}[\text{GeV}]$	$M_{-1/3}[\text{GeV}]$	$M_{5/3}[\text{GeV}]$	λ_R	g_1^{23}	\tilde{g}_1^{33}	$ C_{RL}^V $
795.3	860	860	860	2	1.3	2.6	0.41
734.4	950	950	950	3	1.4	2.25	0.44
700.7	950	950	950	3.4	1.0	1.73	0.30
726.2	1049.3	1100	950	4	1.40	2.24	0.53
754.0	1100	1100	1100	5.3	1.30	2.08	0.47
914.5	1250	1250	1250	6	1.62	2.98	0.50

Table 3.5: Benchmark points satisfying all the constraints while generating a large $|C_{RL}^V|$. In light of the results in Fig. 3.7 we focus on the case of $\tilde{g}_1^{33} \geq g_1^{23}$.

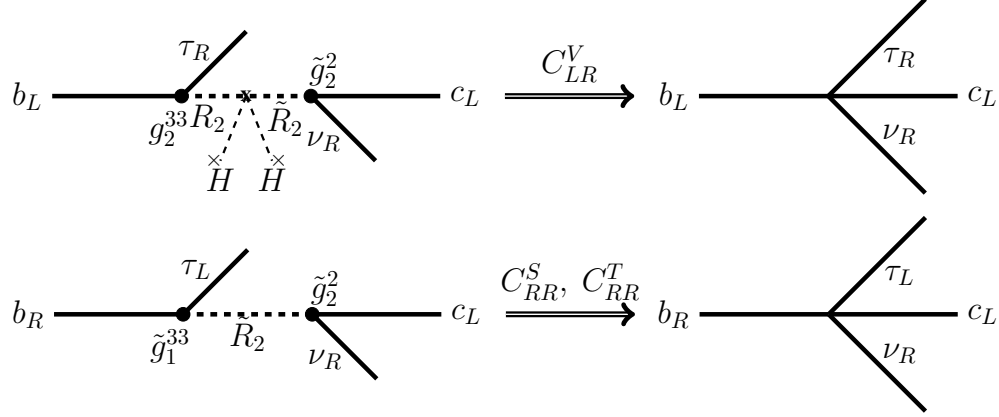


Figure 3.9: The diagrams generating C_{LR}^V (1st row) and C_{RR}^S, C_{RR}^T (2nd row) WCs. The relevant couplings from Eqs. (3.10), (3.16) and (3.23) are shown for each diagram.

couplings of (3.16) can generate

$$C_{LR}^V = -\frac{v^2}{4V_{cb}} g_2^{33} \tilde{g}_2^2 \cos \varphi \sin \varphi \left(\frac{1}{M_{R_h}^2} - \frac{1}{M_{R_l}^2} \right), \quad (3.24)$$

from the diagram shown in Fig. 3.9. In addition, with the \tilde{g} couplings in (3.10) and (3.23), the LQ \tilde{R}_2 can also generate the WCs $C_{RR}^S = 4C_{RR}^T$ at the LQ scale:

$$C_{RR}^S = -\frac{v^2}{4V_{cb}} \tilde{g}_1^{33} \tilde{g}_2^2 \left(\frac{\cos^2 \varphi}{M_{R_h}^2} + \frac{\sin^2 \varphi}{M_{R_l}^2} \right). \quad (3.25)$$

The flavor constraints are now much more stringent than in the case of the LH neutrinos, because now the left-handed quark doublets are involved. The flavor-changing $b \rightarrow s\nu\nu$ process [118, 119, 68, 120, 101] now gives a stringent constraint on the present possibility as the same combination of couplings generating $C_{RR}^S = 4C_{RR}^T$ can give rise to this process, see Fig. 3.10. Given the experimental result, e.g. [154, 155], this constraint puts an upper bound $\mathcal{O}(0.01)$ on C_{RR}^S [156], severely constraining its contribution to $R_{D^{(*)}}$. A small value for $\tilde{g}_2^2 \tilde{g}_1^{33}$ allows us to evade this bound. The coupling combination $\tilde{g}_2^2 \tilde{g}_1^{33}$ can have further contributions to B_s - \bar{B}_s mixing, $b \rightarrow s\gamma$, $B \rightarrow K\tau\tau$, and $B_s \rightarrow \tau\tau$, and $D_s \rightarrow \tau\nu$ as well, see Fig. 3.10. The experimental bounds on these processes [157–159, 3] are not as constraining as the

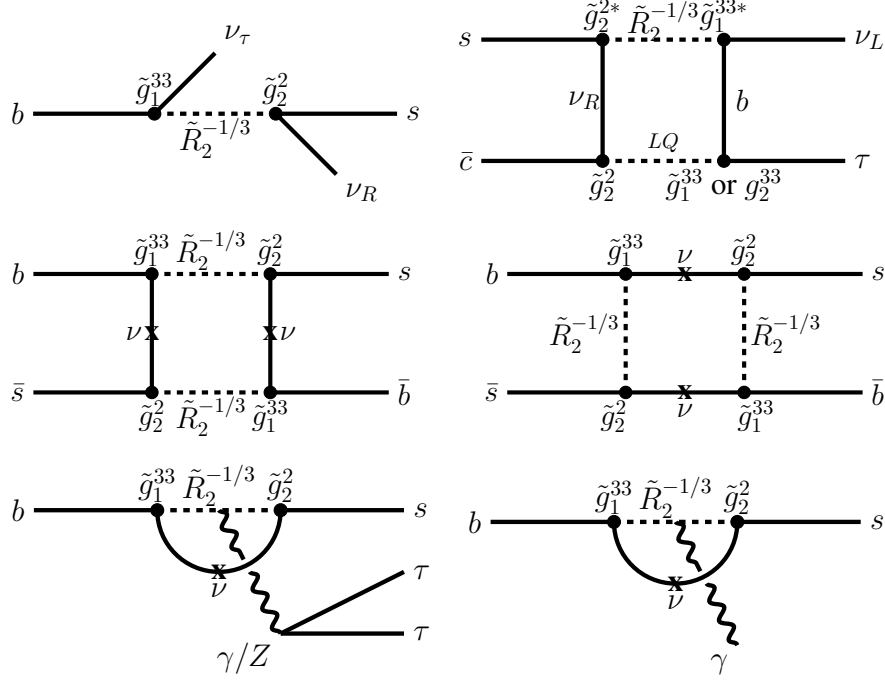


Figure 3.10: The diagrams giving rise to various flavor constraints. The most relevant constraint is from $b \rightarrow s\nu\nu$ (the top-left diagram), which only constrains C_{RR}^S and C_{RR}^T . The other processes include : $D_s \rightarrow \tau\nu$ (top-right), the B_s - \bar{B}_s mixing diagrams (middle row), $B \rightarrow K\tau\tau$ or $B_s \rightarrow \tau\tau$ (bottom-left) and $b \rightarrow s\gamma$ (bottom-right). With the exception of the top diagrams, all the diagrams here are suppressed by the neutrino mixing and will not put tight constraints on our model. The relevant couplings for each process are shown as well; this combination of couplings severely constrains the C_{RR}^S operator in Eq. (3.25) and prevents us from generating both C_{RL}^V and C_{LR}^V simultaneously in our setup. All these bounds can be circumvented by suppressing $\tilde{g}_2^2\tilde{g}_1^{33}$.

$b \rightarrow s\nu\nu$ process. With the fact that the $\tilde{g}_2^2\tilde{g}_1^{33}$ combination must be suppressed, we conclude that C_{RL}^V and C_{LR}^V cannot be generated simultaneously without any issues in flavor constraints.

3.6 Final Remarks

In this chapter we first investigated anomalies observed in $F_{D^*}^L$ and $R_{J/\psi}$ model-independently. We showed that $R_{J/\psi}$ can not be explained by any combination of the possible WCs, while $F_{D^*}^L$ requires all the WCs with a certain neutrino chirality.

We also proposed a LQ scenario that can generate the WC C_{RL}^V to explain $R_{D^{(*)}}$ for the first time. This WC has different effects on polarization observables and is essential for other anomalies in the charged currents such as $F_{D^*}^L$ [61, 160]. The model has a $SU(2)_L \times SU(2)_R$ bidoublet scalar LQ which contains a pair of $SU(2)_L$ doublet LQs. We have studied its phenomenology: flavor constraints, EWPT and collider bounds.

The most constraining limit on this setup comes from collider searches. However, we found that the lightest LQ can be as light as 600 GeV with the help of the new decay channel. An example of such a channel is the LQ decaying to three jets and a very soft MET. With such a low scale of NP and a relatively large quartic coupling between the LQ and the Higgs, we could produce a large enough WC C_{RL}^V to explain the flavor anomalies $R_{D^{(*)}}$.

It is interesting to note that according to [61] the present model and a U_1 LQ generate all the WCs which explain $F_{D^*}^L$, and $R_{D^{(*)}}$.

Since there is an additional scalar in the present model which leads to a new hierarchy problem and our low-energy theory breaks down at $\mathcal{O}(10)$ TeV, we are tempted to consider some UV completion near the TeV scale. One direction is to make our new scalar, as well as the Higgs, composites of new strong dynamics. In the

minimal composite Higgs scenario [161], the Higgs field is a pseudo-Nambu-Goldstone boson (pNGB) transforming as $\mathbf{4}$ under the unbroken $SO(4) \simeq SU(2)_L \times SU(2)_R$ which the global $SO(5)$ in a strong sector is spontaneously broken to. It may be interesting to embed our scalar LQ into a pNGB also transforming as $\mathbf{4}$ under the $SO(4)$ which some larger global symmetry is broken to. In this scenario, the relatively large value of the scalar quartic coupling is rather natural. However, one issue is that if we assume elementary quarks and leptons the LQ couplings to the fermions are naturally suppressed due to the large dimension of the scalar composite. We may need partial compositeness of quarks and leptons [162] as in the case of the top quark Yukawa in composite Higgs models.

Chapter 4

Discerning Different Solutions

In the previous chapters we introduced two new solutions to the charge current anomalies observed in flavor experiments. There are a few other proposals that can explain these anomalies as well. A natural question to ask at this stage is, if we establish that these anomalies are due to some NP, is there anyway we can tell different possible solutions apart?

As the ratios $R_{D^{(*)}}$ are both explained by various models, we need to carry out further measurements to discern different models from one another. In this chapter, we first review the existing minimal solutions to $R_{D^{(*)}}$ and the experimental bounds on each of them; then we study a few asymmetry observables that received different contributions from different models. We will show that by measuring these observables we will be able to distinguish almost all different solutions of $R_{D^{(*)}}$.

4.1 Simplified Models for $R_{D^{(*)}}$

The set of all possible dimension-6 operators modifying the $b \rightarrow c\tau\nu$ decay are already reported in Eq. (1.10). We saw that these operators can be generated by integrating out heavy new mediators; the WCs C_{MN}^X parametrize the most general contribution.¹ Different UV models can be categorized using the operators they give rise to (typically more than one), see Sec. 4.1.2.

In the operator basis of (1.10), the contribution of new physics to the ratios $R_{D^{(*)}}$

¹The tensor operators with $M \neq N$, \mathcal{O}_{RL}^T and \mathcal{O}_{LR}^T , are identically zero.

can be calculated in terms of the ten (possibly complex) WCs: five involving a SM left-handed neutrino, and five requiring a new right-handed neutrino. The numerical contribution of all the operators from (1.10) to the ratios were shown in Eq. (2.1). Further details on deriving these numerical equations are included in App. D.

4.1.1 Single Operator Solutions

The range of $R_{D^{(*)}}$ that each individual operator can generate (with general complex WCs) is indicated in Fig. 4.1, along with the present-day experimental and theoretical combined uncertainty in the $R_{D^{(*)}}$ measurements, showing the 1, 2, and 5σ contours (gray-dashed ellipses). For a review of experimental correlations in the measurements of $R_{D^{(*)}}$, see [6, 8]. In Fig. 4.1, we use the current average of the correlations, $\rho_{\text{corr}} = -0.2$ [13]. We see that out of all ten effective operators in (1.10), there are only six that can explain both anomalies simultaneously: \mathcal{O}_{LL}^V , \mathcal{O}_{RL}^V , \mathcal{O}_{LL}^S , \mathcal{O}_{LL}^T , \mathcal{O}_{RR}^V , and \mathcal{O}_{LR}^V .

4.1.2 Simplified Model Solutions

We can now enumerate the full set of “simplified” models that can explain both the $R_{D^{(*)}}$ anomalies. In this context, “simplified” means a single new mediator particle that can be integrated out to provide one or more of the effective operators which modify $R_{D^{(*)}}$.

An over-complete list of all the simplified models that can generate the operators in (1.10) with LH or RH neutrinos can be found in [68, 163, 156]. We gather these mediators in Tab. 4.1. Notice that the S_1 and U_1 LQs and uncolored mediators can couple to either LH or RH fermions and so give rise to operators involving either type of neutrinos. In this work we consider these possibilities as separate solutions to the anomalies and will try to distinguish them from one another.

The factor of x in Tab. 4.1 relates the WCs of scalar and tensor operators in some

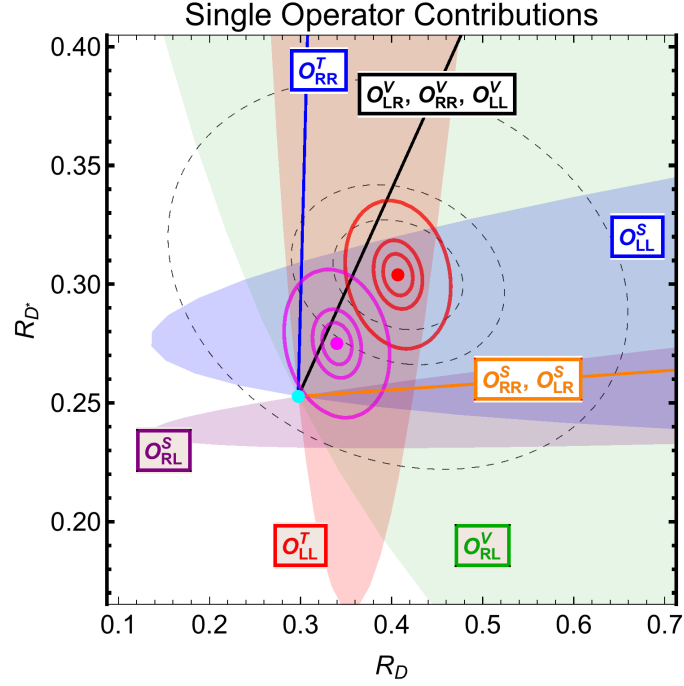


Figure 4.1: Ranges of $R_{D^{(*)}}$ spanned by single operators with complex WCs. The SM prediction is denoted by a cyan dot. No other experimental constraints are imposed in this figure. The 1, 2, and 5σ contours around the current global average are shown as gray-dashed lines. We also show these contours with the projected Belle II precision [2] around the current global average (red ellipses) and a hypothetical average after Belle II that still barely allows a 5σ discovery (magenta ellipses), assuming the current correlation $\rho_{\text{corr}} = -0.2$. (See Sec. 4.1.4 for details.)

models after Fierz transformation. At the mediator scale, $x = 1/4$ for all the models in Tab. 4.1; as we run down to the GeV scale x changes to $\sim 1/8$ [164, 165, 110], with the exact value depending on the mediator scale. For simplicity, we use the fiducial value $x = 1/8$ in our analysis.

In Fig. 4.2, we show the values of R_D and R_{D^*} which can be obtained by each of the relevant mediators in Tab. 4.1, scanning over complex Wilson coefficient(s). In these plots the superscripts L and R on S_1 and U_1 LQs refer to the neutrino chirality they couple to. Some mediators yield lines in this parameter space; these are single-coefficient models whose contribution to R_D and R_{D^*} are independent of the phase of the coefficient. Other operators can cover a region of $R_{D^{(*)}}$ as the coefficients are varied, either because the $R_{D^{(*)}}$ values depend on both magnitude and phase of single operator, or the model results in two independent WCs.

4.1.3 Additional Constraints and Final List of Viable Models

In addition to explaining $R_{D^{(*)}}$, a viable mediator must also avoid a number of other stringent constraints. In this subsection we will review these and then list the surviving viable solutions.

A subset of the couplings which modify the $\bar{B} \rightarrow D^{(*)}\tau\nu$ decay can enhance the branching ratio $B_c \rightarrow \tau\nu$ [49, 51, 50, 52, 109]. In terms of the WCs in (1.10),

$$\begin{aligned} \frac{Br(B_c \rightarrow \tau\nu)}{Br(B_c \rightarrow \tau\nu)|_{\text{SM}}} &= \left| (C_{LL}^V - C_{RL}^V) + \frac{m_{B_c}^2}{m_\tau(m_b + m_c)} (C_{RL}^S - C_{LL}^S) \right|^2 \\ &+ \left| (C_{RR}^V - C_{LR}^V) + \frac{m_{B_c}^2}{m_\tau(m_b + m_c)} (C_{LR}^S - C_{RR}^S) \right|^2. \end{aligned} \quad (4.1)$$

Given the mass ratios above, these equations imply tighter bounds on the scalar operators than the vector ones. The SM prediction is $Br(B_c \rightarrow \tau\nu)|_{\text{SM}} \sim 2\%$. The $B_u \rightarrow \tau\nu$ decay in LEP at the Z boson peak can be used to place the constraint [52]

$$Br(B_c \rightarrow \tau\nu) \leq 10\%, \quad (4.2)$$

Mediator	Operator Combination	Viability (V or NV)
Colorless Scalars	\mathcal{O}_{XL}^S	NV ($Br(B_c \rightarrow \tau\nu)$)
W'^μ (LH fermions)	\mathcal{O}_{LL}^V	NV (collider bounds)
S_1 LQ ($\bar{3}, 1, 1/3$) (LH fermions)	$\mathcal{O}_{LL}^S - x\mathcal{O}_{LL}^T, \quad \cancel{\mathcal{O}_{LL}^V}$	V
U_1^μ LQ ($3, 1, 2/3$) (LH fermions)	$\mathcal{O}_{RL}^S, \quad \mathcal{O}_{LL}^V$	V
R_2 LQ ($3, 2, 7/6$)	$\mathcal{O}_{LL}^S + x\mathcal{O}_{LL}^T$	V
S_3 LQ ($\bar{3}, 3, 1/3$)	\mathcal{O}_{LL}^V	NV ($b \rightarrow s\nu\nu$)
U_3^μ LQ ($3, 3, 2/3$)	\mathcal{O}_{LL}^V	NV ($b \rightarrow s\nu\nu$)
V_2^μ LQ ($\bar{3}, 2, 5/6$)	\mathcal{O}_{RL}^S	NV ($R_{D^{(*)}}$ value)
Colorless Scalars	\mathcal{O}_{XR}^S	NV ($Br(B_c \rightarrow \tau\nu)$)
W'^μ (RH fermions)	\mathcal{O}_{RR}^V	V
\tilde{R}_2 LQ ($3, 2, 1/6$)	$\mathcal{O}_{RR}^S + x\mathcal{O}_{RR}^T$	NV ($b \rightarrow s\nu\nu$)
S_1 LQ ($\bar{3}, 1, 1/3$) (RH fermions)	$\mathcal{O}_{RR}^V, \quad \cancel{\mathcal{O}_{RR}^S - x\mathcal{O}_{RR}^T}$	V
U_1^μ LQ ($3, 1, 2/3$) (RH fermions)	$\mathcal{O}_{LR}^S, \quad \mathcal{O}_{RR}^V$	V

Table 4.1: A complete list of the simplified mediator models and resulting effective operators that are possibly relevant for the $R_{D^{(*)}}$ anomalies. The U_1^μ and S_1 LQs as well as the colorless scalars can give rise to two independent WCs, while the rest of the mediators can generate only one. We use $x = 1/8$ in this work, see the text for more details. We indicate in the last column if the model is still viable (by V) or not (by NV), and if not, what experimental constraint rules it out (see Sec. 4.1.3 for discussion of these constraints). The operators with a line crossed over them are severely constrained by the $b \rightarrow s\nu\nu$ constraints as well.

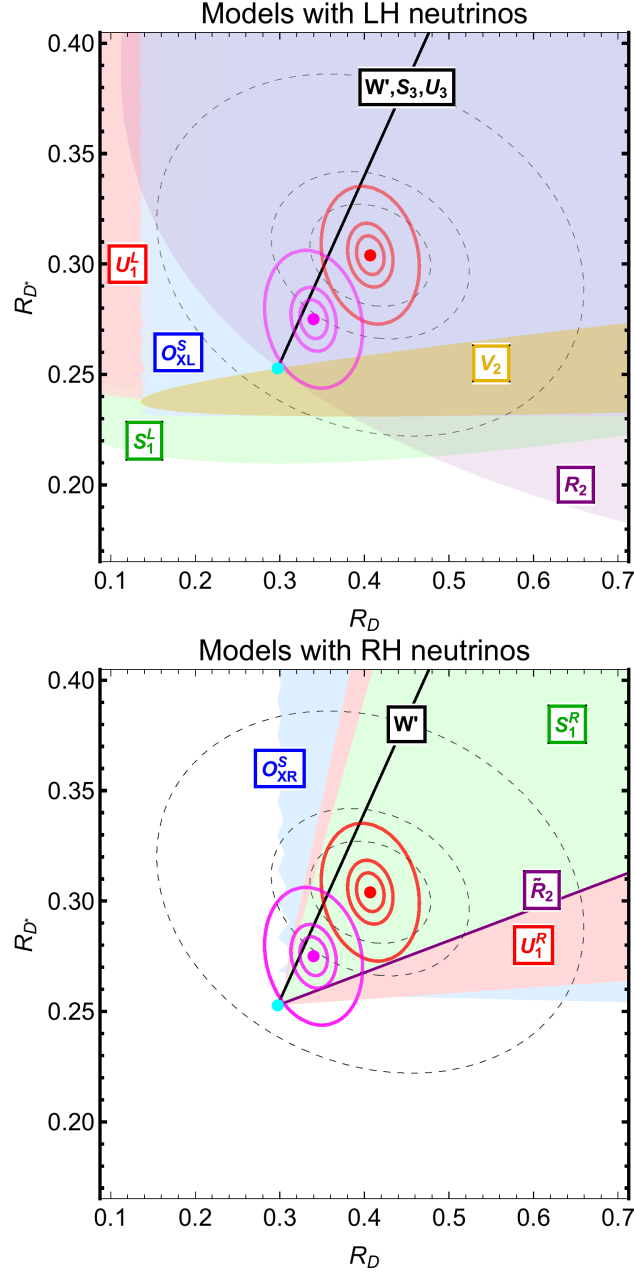


Figure 4.2: The range of $R_{D^{(*)}}$ spanned by the simplified models from Tab. 4.1 with complex WCs. The superscript on S_1 and U_1 LQ refers to the neutrino chirality which they are coupled to in each figure. No other experimental constraints are imposed in this figure. The other features are as in Fig. 4.1.

which in turn puts a constraint on the possible WCs in (4.1). Using the theoretical calculation of the B_c lifetime and its uncertainties, a looser bound of $Br(B_c \rightarrow \tau\nu) \leq 30\%$ can be obtained as well [51]. These branching ratio constraints put particularly severe bounds on models relying on \mathcal{O}_{MN}^S operators to explain the anomalies – to the extent that if a model relies solely on a scalar operator to explain the anomalies, it is ruled out by the constraint (4.2). This remains true even if the global average of the anomalies reduces to the magenta dot in Fig. 4.2 after Belle II.

The other relevant flavor constraint is from $b \rightarrow s\nu\nu$ decay and the meson decays it enables [118, 119, 68], in particular the inclusive $B \rightarrow X_s\nu\nu$ and the exclusive $B \rightarrow K^{(*)}\nu\nu$. The current bound on the inclusive branching ratio of $B \rightarrow X_s\nu\nu$ is from the ALEPH Collaboration [166],

$$Br(B \rightarrow X_s\nu\nu) \leq 6.4 \times 10^{-4} \quad (4.3)$$

at 90% CL, whereas the bound on the exclusive decay rates above are [155]

$$Br(B \rightarrow K\nu\nu) \leq 1.6 \times 10^{-5}, \quad Br(B \rightarrow K^*\nu\nu) \leq 2.7 \times 10^{-5}. \quad (4.4)$$

While the mediators introduced for $R_{D^{(*)}}$ generate charged currents, the $b \rightarrow s\nu\nu$ decay requires a neutral current beyond the SM. However, in some models that rely on leptoquarks [68, 120, 156], there is an inevitable neutral current due to the SM $SU(2)_L$ symmetry.

If both the neutrinos in the $b \rightarrow s\nu\nu$ decay are LH, Lorentz invariance implies that the dimension six effective operator can only be a vector current. The associated charged current then can only give rise to \mathcal{O}_{LL}^V . Thus, for the models with LH neutrinos, this bound may only constrain the C_{LL}^V Wilson coefficient.

For instance, the S_3 LQ can give rise to the following terms (among others) [120]

$$\mathcal{L} \supset g_L^{ij} \bar{Q}_L^{c,i} i\sigma_2 \sigma^a L_L^j S_3^a, \quad (4.5)$$

where i, j are flavor indices and a is an $SU(2)$ adjoint index. After Fierz transformation, this LQ can give rise to \mathcal{O}_{LL}^V with

$$C_{LL}^V = -\frac{V_{tb}}{V_{cb}} \frac{g_L^{3j_1} g_L^{23,*}}{4\sqrt{2}G_F M_{S_3}^2}, \quad (4.6)$$

where G_F is the fermi constant and M_{S_3} is the S_3 LQ mass. Due to the $SU(2)_L$ symmetry, this term will contribute to $b \rightarrow s\nu\nu$ as well.² The contribution of this LQ to the neutral $b \rightarrow s\nu\nu$ processes can be captured by the following effective Hamiltonian [119]

$$\mathcal{H}_{\text{eff}} \supset -\sqrt{2} \frac{\alpha_{em}}{\pi} G_F V_{ts}^* V_{tb} C_L^\nu (\bar{s} \gamma^\mu P_L b) (\bar{\nu} \gamma_\mu P_L \nu), \quad (4.7)$$

where C_L^ν is a Wilson coefficient and α_{em} is the fine structure constant. After integrating out a S_3 LQ, the generated C_L^ν Wilson coefficient will be

$$C_L^\nu = \frac{\pi}{2\sqrt{2}\alpha_{em} G_F V_{ts}^* V_{tb}} \frac{g_L^{2j_1} g_L^{3j_2,*}}{M_{S_3}^2}, \quad (4.8)$$

where j indices refer to different generations of neutrinos. Using the numerical formulas reported in [119] and the bound on $Br(B \rightarrow K\nu\nu)$, which is the most constrained branching ratio in (4.3)-(4.4), we find

$$|g_L^{3j_1} g_L^{2j_2,*}| \frac{1\text{TeV}^2}{M_{S_3}^2} \lesssim 0.017, \quad (4.9)$$

which when combined with (4.6) yields the following bound on the contribution on NP to C_{LL}^V :

$$(C_{LL}^V)_{NP} \lesssim 0.006. \quad (4.10)$$

This bound is severe enough that we can safely neglect the contribution of C_{LL}^V from the S_3 LQ to the anomalies. A similar bound also applies to the U_3 and S_1 LQs that are coupled to LH fermions [120]. S_3 and U_3 can only generate \mathcal{O}_{LL}^V and

²It is possible to generate C_{LL}^V with these leptoquarks by invoking $g_L^{i \neq 3, j}$ couplings as well. In this case, however, we will have a substantial CKM suppression and will need non-perturbative couplings to explain the anomalies. As a result, we discard this possibility.

are therefore completely ruled out. Since S_1 can generate \mathcal{O}_{LL}^S and \mathcal{O}_{LL}^T operators from other couplings in the Lagrangian, it can still be a viable explanation of the anomalies despite this severe bound on C_{LL}^V . Finally, due to the $SU(2)$ structure of the operators that it gives rise to, this bound does not apply to U_1 LQ [118, 120], even though this LQ does generate \mathcal{O}_{LL}^V .

If instead we allow for one of the neutrinos in the $b \rightarrow s\nu\nu$ process to be RH, then the dimension six effective operator can be either a scalar or a tensor current. In particular, the same couplings that generate $\mathcal{O}_{RR}^S \pm x\mathcal{O}_{RR}^T$ operators in S_1 and \tilde{R}_2 LQs also give rise to the operators [156]

$$(\bar{s}_L b_R)(\bar{\nu}_L \nu_R), \quad (\bar{s}_L \sigma^{\mu\nu} b_R)(\bar{\nu}_L \sigma_{\mu\nu} \nu_R), \quad (4.11)$$

which contribute to the $b \rightarrow s\nu\nu$ processes. The bound on these operators WCs translates into $\mathcal{O}(0.01)$ bounds on the \mathcal{O}_{RR}^S in S_1 and \tilde{R}_2 models [156], hence we can safely discard their contribution to the anomalies too.³ The \tilde{R}_2 is thus ruled out, while the S_1 LQ model becomes degenerate with a W' and the single operator C_{RR}^V .

Other than these flavor constraints, there are some bounds from direct searches for these mediators. For the case of leptoquarks, the current bounds are not severe enough to rule out any further models [156, 110, 167]. On the other hand, the bounds on the W' are fairly constraining [60, 168, 56, 101]. In particular, if the W' couples to LH fermions, the bounds on the accompanying Z' effectively rule out the explanations of the anomalies [56, 101].

The combination of these constraints significantly reduces the viable explanations of the $R_{D^{(*)}}$ anomalies. In the last column of Tab. 4.1 we indicate which models survive. In all, there are three viable simplified models (S_1 , R_2 , and U_1 LQs) that couple to LH neutrinos, and three that couple to RH (W' , U_1 and S_1 LQs). Note however

³Notice that since these models do not have any interference with the SM, the contribution to the anomalies is quadratic in their Wilson coefficient and a $\mathcal{O}(0.01)$ bound on a Wilson coefficient implies order 10^{-4} improvement in the $R_{D^{(*)}}$ ratios.

that the W' and S_1 LQ with RH neutrinos generate the same Wilson coefficient, which is a subset of the parameter space generated by the U_1 LQ with RH neutrinos. In the rest of this chapter, we will focus on these surviving simplified models, along with the viable single operators \mathcal{O}_{LR}^V , \mathcal{O}_{RL}^V , and \mathcal{O}_{LL}^T .

4.1.4 Benchmark Belle II Scenarios

Belle II will measure $R_{D^{(*)}}$ with much smaller errors compared to the present, thus greatly reducing the possible range of WCs in each model. As can be seen in Figs. 4.1–4.2, central values near the present averages would by themselves rule out at high significance many models which are presently under consideration. Meanwhile, values closer to the SM prediction (while still allowing a 5σ discovery at Belle II) would leave all the mediators and single operators we currently consider as possibilities, before constraints from the asymmetry observables are applied. Aside from having a potentially huge impact on the list of models that explain the anomalies, this can also greatly affect our ability to distinguish between these models with further measurements (such as the asymmetries).

As a result, we will consider two different outcomes of the Belle II measurement of $R_{D^{(*)}}$ as benchmarks for our study.

1. *The 10σ scenario:* Belle II measures $R_{D^{(*)}}$ with central values equal to the present average. With the projected Belle II sensitivities, this would correspond to a $\mathcal{O}(10\sigma)$ discovery. We then consider ranges of $R_{D^{(*)}}$ within the 2σ Belle II error ellipse about this central value (the second innermost red ellipse in Fig. 4.1–4.2). As we will show, in the 10σ scenario, the task of discerning different models is simplified considerably.
2. *The 5σ scenario:* The measured $R_{D^{(*)}}$ values are closer to the SM expectation while still allowing a 5σ discovery; specifically, we assume the central value of

the anomalies after Belle II shifts to $R_D = 0.34$ and $R_{D^*} = 0.275$. This point was chosen to have 5σ significance with Belle II projected error bars, to be within $\sim 2\sigma$ of the current global average, and (crucially) to allow for all of the simplified models to continue to explain the $R_{D^{(*)}}$ anomalies (see Fig. 4.2). Compared to the 10σ scenario, distinguishing between different models is much more challenging here.

These two benchmark scenarios are meant to bracket the range of possibilities that we can expect from Belle II, assuming that the $R_{D^{(*)}}$ anomalies are fully confirmed. The 10σ scenario is meant to illustrate how easy it can be to distinguish different models using the τ asymmetries, while the 5σ scenario is meant to provide a “worst-case scenario” from the point of view of distinguishing between different models.

4.2 Asymmetry Observables

The relevant models for $R_{D^{(*)}}$ and their predictions for these ratios were reviewed in the previous section. However, one can extract more information from the decay processes than just the total decay rate and the ratios $R_{D^{(*)}}$. Shown in Fig. 4.3 is a diagram of the detailed kinematics of the decay process. Many of these angles and momenta can be measured or reconstructed, and they provide a much finer probe of the effective Hamiltonian responsible for the decay.

In particular, using the event kinematics, we can construct asymmetry observables which are sensitive to the different WCs in (1.10). Four such observables are the forward-backward asymmetry of the τ lepton with respect to $\vec{p}_{D^{(*)}}$ in Fig. 4.3, denoted by $\mathcal{A}_{FB}^{(*)}$, and its polarization asymmetry in all three of the \hat{e} directions in Fig. 4.3, denoted by $\mathcal{P}_{\hat{e}}^{(*)}$. All of these asymmetries are defined in the leptonic center of mass frame, which we will also refer to as the “ q^2 frame”, where $q = p_B - p_{D^{(*)}} = p_\tau + p_\nu$ denotes the four-momentum transferred to the leptonic system by the decaying B

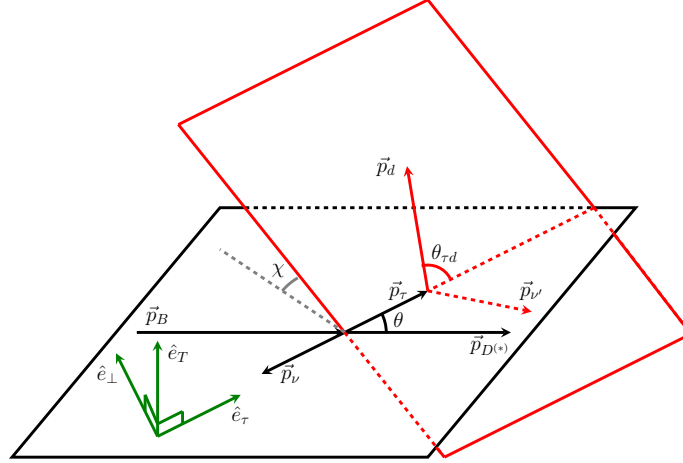


Figure 4.3: The kinematics of $\bar{B} \rightarrow D^{(*)} \tau \nu$ and subsequent $\tau \rightarrow d \nu'$ decay processes, in the center-of-mass frame of the leptonic system (the “ q^2 frame”). The black plane indicates the original decay plane, defined by the B momentum \vec{p}_B (or the $D^{(*)}$ momentum $\vec{p}_{D^{(*)}}$) and the leptonic pair. The red plane is the decay plane of the τ , defined by the visible daughter meson d and invisible daughter neutrino ν' of the τ . The three directions in which we will project the τ polarization asymmetries are indicated in green.

meson. As we will see, models with LH and RH neutrinos have a qualitatively different contribution to these asymmetry observables.

We will calculate the dependence of these observables on all the WCs in (1.10) and report the result in the form of numerical formulas (like (2.1) for R_D and R_{D^*}). In particular, we carry out the calculation including the contribution of the operators with right-handed sterile neutrinos with negligible masses compared to the other energy scales in the decay. Full analytic versions are available in the appendices. Wherever possible, we have checked that parts of our calculations (results from the numerical equations, q^2 distributions, the SM predictions, etc.) are in agreement with previous studies, e.g. [39, 40, 58, 169]. A further consistency check is that the numerical equations for the observables will manifest a symmetry between left- and

right-handed neutrinos such that by applying the following transformations,

$$h_\tau \rightarrow -h_\tau, \quad C_{LL}^{S,V,T} \leftrightarrow \left(C_{RR}^{S,V,T}\right)^*, \quad C_{RL}^X \leftrightarrow \left(C_{LR}^X\right)^*, \quad (4.12)$$

(where h_τ refers to the τ helicity) the observables will transform as

$$R_{D^{(*)}} \rightarrow R_{D^{(*)}}, \quad \mathcal{P}_x \rightarrow -\mathcal{P}_x, \quad \mathcal{A}_{FB} \rightarrow \mathcal{A}_{FB}. \quad (4.13)$$

In writing C_{LL}^V in (4.12) (and in all the up-coming numerical equations), we are including the contribution of the SM operator.⁴ These symmetries indicate that if we flip the spin of all the external particles and the associated WCs, we should get the same result for the decay rate in a particular q^2 and θ direction. The interference between the SM term in (4.12) and the sign flip in (4.13) are the two sources of the qualitatively different contributions from different types of neutrinos.

4.2.1 Forward-backward Asymmetry

The first observable of interest is the forward-backward asymmetry in the τ lepton decay with respect to the $D^{(*)}$ direction. This observable and its correlation with $R_{D^{(*)}}$ have been studied previously [39, 34, 36, 37, 32, 33, 35, 38, 40, 41]. It is defined as

$$\mathcal{A}_{FB}^{(*)} = \frac{1}{\Gamma^{(*)}} \left(- \int_{\theta=0}^{\theta=\pi/2} + \int_{\theta=\pi/2}^{\theta=\pi} \right) d\theta \frac{d\Gamma^{(*)}}{d\theta}, \quad (4.14)$$

where θ is the angle between the τ and $D^{(*)}$ momenta in the leptonic system rest frame, see Fig. 4.3, and $\Gamma^{(*)}$ is the total decay rate of $\bar{B} \rightarrow D^{(*)}\tau\nu$. The full analytic expression for $\frac{d\Gamma^{(*)}}{d\theta}$ in terms of all the WCs is included in App. D. The numerical

⁴The complex conjugate in the way the WCs are transformed is only relevant for the study of $\mathcal{P}_T^{(*)}$ observables and is essentially an artifact of the definition in (D.2) and how the τ spin transforms under this symmetry.

formula for $\mathcal{A}_{FB}^{(*)}$ that follows from this is:

$$\begin{aligned}
\mathcal{A}_{FB} &\approx \frac{1}{R_D} \left\{ -0.11 \left(|C_{LL}^V + C_{RL}^V|^2 + |C_{RR}^V + C_{LR}^V|^2 \right) \right. \\
&\quad - 0.35 \mathcal{R}e \left[(C_{LL}^S + C_{RL}^S)(C_{LL}^T)^* + (C_{RR}^S + C_{LR}^S)(C_{RR}^T)^* \right] \\
&\quad - 0.24 \mathcal{R}e \left[(C_{LL}^V + C_{RL}^V)(C_{LL}^T)^* + (C_{RR}^V + C_{LR}^V)(C_{RR}^T)^* \right] \\
&\quad \left. - 0.15 \mathcal{R}e \left[(C_{LL}^V + C_{RL}^V)(C_{LL}^S + C_{RL}^S)^* + (C_{RR}^V + C_{LR}^V)(C_{RR}^S + C_{LR}^S)^* \right] \right\}, \\
\end{aligned} \tag{4.15}$$

$$\begin{aligned}
\mathcal{A}_{FB}^* &\approx \frac{1}{R_{D^*}} \left\{ -0.813 \left(|C_{LL}^T|^2 + |C_{RR}^T|^2 \right) \right. \\
&\quad + 0.016 \left(|C_{LL}^V|^2 + |C_{RR}^V|^2 \right) - 0.082 \left(|C_{RL}^V|^2 + |C_{LR}^V|^2 \right) \\
&\quad + 0.066 \mathcal{R}e \left[C_{RL}^V (C_{LL}^V)^* + (C_{LR}^V)^* C_{RR}^V \right] \\
&\quad + 0.095 \mathcal{R}e \left[(C_{RL}^S - C_{LL}^S)(C_{LL}^T)^* + (C_{LR}^S - C_{RR}^S)^* C_{RR}^T \right] \\
&\quad + 0.395 \mathcal{R}e \left[(C_{LL}^V - C_{RL}^V)(C_{LL}^T)^* + (C_{RR}^V - C_{LR}^V)^* (C_{RR}^T) \right] \\
&\quad + 0.023 \mathcal{R}e \left[(C_{LL}^S - C_{RL}^S)(C_{LL}^V - C_{RL}^V)^* + (C_{RR}^S - C_{LR}^S)^* (C_{RR}^V - C_{LR}^V) \right] \\
&\quad \left. - 0.142 \mathcal{R}e \left[(C_{LL}^T)(C_{LL}^V + C_{RL}^V)^* + (C_{RR}^T)^* (C_{RR}^V + C_{LR}^V) \right] \right\}, \\
\end{aligned}$$

The factor of $R_{D^{(*)}}$ in the denominators are the result of normalizing to the total decay rate $\Gamma^{(*)}$ in (4.14).

4.2.2 Tau Polarization Asymmetries

Our second set of observables is comprised of the different polarization asymmetries of the τ lepton in the decay. Such asymmetries are defined as

$$\mathcal{P}_{\hat{e}}^{(*)} = \frac{\Gamma_{+\hat{e}}^{(*)} - \Gamma_{-\hat{e}}^{(*)}}{\Gamma_{+\hat{e}}^{(*)} + \Gamma_{-\hat{e}}^{(*)}}, \tag{4.16}$$

where \pm refer to the two possible outcomes of measuring τ spin along direction \hat{e} . The vector \hat{e} can be in any arbitrary direction. We consider the three directions [41],

$$\hat{e}_\tau = \frac{\vec{p}_\tau}{|\vec{p}_\tau|}, \quad \hat{e}_T = \frac{\vec{p}_{D^{(*)}} \times \vec{p}_\tau}{|\vec{p}_{D^{(*)}} \times \vec{p}_\tau|}, \quad \hat{e}_\perp = \hat{e}_T \times \hat{e}_\tau, \tag{4.17}$$

where \vec{p}_τ ($\vec{p}_{D^{(*)}}$) is the spatial momentum of the τ ($D^{(*)}$) in the final state (all in the q^2 frame). $\mathcal{P}_\tau^{(*)}$ indicates the polarization asymmetry along the longitudinal direction of the τ lepton, and $\mathcal{P}_\perp^{(*)}$ the asymmetry in the decay plane and perpendicular to \vec{p}_τ , while $\mathcal{P}_T^{(*)}$ is the polarization asymmetry along the direction normal to the decay plane including τ and $D^{(*)}$, see Fig. 4.3. The first two are CP-even while the latter is CP-odd. The details of calculating each $\mathcal{P}_\epsilon^{(*)}$ and their analytic results are included in App. D.

Longitudinal polarization

The numerical expression for the contribution of all the WCs to $\mathcal{P}_\tau^{(*)}$ is:

$$\begin{aligned}
\mathcal{P}_\tau \approx & \frac{1}{R_D} \left\{ 0.402 \left(|C_{LL}^S + C_{RL}^S|^2 - |C_{RR}^S + C_{LR}^S|^2 \right) \right. \\
& + 0.013 \left[|C_{LL}^T|^2 - |C_{RR}^T|^2 \right] + 0.097 \left[|C_{LL}^V + C_{RL}^V|^2 - |C_{RR}^V + C_{LR}^V|^2 \right] \\
& + 0.512 \mathcal{Re} \left[(C_{LL}^V + C_{RL}^V)(C_{LL}^S + C_{RL}^S)^* - (C_{RR}^V + C_{LR}^V)(C_{RR}^S + C_{LR}^S)^* \right] \\
& - 0.099 \mathcal{Re} \left[(C_{LL}^V + C_{RL}^V)(C_{LL}^T)^* - (C_{RR}^V + C_{LR}^V)(C_{RR}^T)^* \right] \left. \right\}
\end{aligned} \tag{4.18}$$

$$\begin{aligned}
\mathcal{P}_\tau^* \approx & \frac{1}{R_{D^*}} \left\{ -0.127 \left(|C_{LL}^V|^2 + |C_{RL}^V|^2 - |C_{RR}^V|^2 - |C_{LR}^V|^2 \right) \right. \\
& + 0.011 \left(|C_{LL}^S - C_{RL}^S|^2 - |C_{RR}^S - C_{LR}^S|^2 \right) + 0.172 \left(|C_{LL}^T|^2 - |C_{RR}^T|^2 \right) \\
& + 0.031 \mathcal{Re} \left[(C_{LL}^V - C_{RL}^V)(C_{RL}^S - C_{LL}^S)^* - (C_{RR}^V - C_{LR}^V)(C_{LR}^S - C_{RR}^S)^* \right] \\
& + 0.350 \mathcal{Re} \left[(C_{LL}^V)(C_{LL}^T)^* - (C_{RR}^V)(C_{RR}^T)^* \right] \\
& - 0.481 \mathcal{Re} \left[(C_{RL}^V)(C_{LL}^T)^* - (C_{LR}^V)(C_{RR}^T)^* \right] \\
& + 0.216 \mathcal{Re} \left[(C_{LL}^V)(C_{RL}^V)^* - (C_{RR}^V)(C_{LR}^V)^* \right] \left. \right\}.
\end{aligned}$$

Perpendicular polarization

Similar to the previous section we include the numerical expression for contribution of all the WCs to $\mathcal{P}_\perp^{(*)}$.

$$\begin{aligned}
\mathcal{P}_\perp \approx & \frac{1}{R_D} \mathcal{R}e \left\{ -0.350 \left[(C_{LL}^T) (C_{LL}^S + C_{RL}^S)^* - (C_{RR}^T)^* (C_{RR}^S + C_{LR}^S) \right] \right. \\
& - 0.357 \left[(C_{LL}^V + C_{RL}^V) (C_{LL}^S + C_{RL}^S)^* - (C_{RR}^V + C_{LR}^V)^* (C_{RR}^S + C_{LR}^S) \right] \\
& - 0.247 \left[(C_{LL}^V + C_{RL}^V)^* (C_{LL}^T) - (C_{RR}^V + C_{LR}^V) (C_{RR}^T)^* \right] \\
& \left. - 0.250 \left[|C_{LL}^V + C_{RL}^V|^2 - |C_{RR}^V + C_{LR}^V|^2 \right] \right\}
\end{aligned} \tag{4.19}$$

$$\begin{aligned}
\mathcal{P}_\perp^* \approx & \frac{1}{R_D^*} \mathcal{R}e \left\{ (C_{RR}^S - C_{LR}^S) \left[0.099 C_{RR}^T - 0.054 (C_{RR}^V - C_{LR}^V) \right]^* \right. \\
& - (C_{LL}^S - C_{RL}^S)^* \left[0.099 C_{LL}^T - 0.054 (C_{LL}^V - C_{RL}^V) \right] \\
& + (C_{RR}^T) \left[0.146 C_{RR}^V - 0.478 C_{LR}^V - 1.855 C_{RR}^T \right]^* \\
& - (C_{LL}^T)^* \left[0.146 (C_{LL}^V) - 0.478 C_{RL}^V - 1.855 C_{LL}^T \right] \\
& + (C_{LR}^V) \left[-0.081 C_{RR}^T + 0.025 C_{LR}^V - 0.075 C_{RR}^V \right]^* \\
& - (C_{RL}^V)^* \left[-0.081 C_{LL}^T + 0.025 C_{RL}^V - 0.075 (C_{LL}^V) \right] \\
& + (C_{RR}^V) \left[-0.071 C_{RR}^T - 0.075 C_{LR}^V + 0.126 C_{RR}^V \right]^* \\
& \left. - (C_{LL}^V)^* \left[-0.071 C_{LL}^T - 0.075 C_{RL}^V + 0.126 (C_{LL}^V) \right] \right\}.
\end{aligned}$$

Transverse polarization

Finally, we present the numerical formulas for $\mathcal{P}_T^{(*)}$:

$$\begin{aligned}\mathcal{P}_T \approx & \frac{1}{R_D} \text{Im} \{ -0.350 [(C_{LL}^T) (C_{LL}^S + C_{RL}^S)^* - (C_{RR}^T)^* (C_{RR}^S + C_{LR}^S)] \\ & - 0.357 [(C_{LL}^V + C_{RL}^V) (C_{LL}^S + C_{RL}^S)^* - (C_{RR}^V + C_{LR}^V)^* (C_{RR}^S + C_{LR}^S)] \\ & - 0.247 [(C_{LL}^V + C_{RL}^V)^* (C_{LL}^T) - (C_{RR}^V + C_{LR}^V) (C_{RR}^T)^*] \} \end{aligned} \quad (4.20)$$

$$\begin{aligned}\mathcal{P}_T^* \approx & \frac{1}{R_D^*} \text{Im} \{ (C_{RR}^S - C_{LR}^S) [0.099 C_{RR}^T - 0.054 (C_{RR}^V - C_{LR}^V)]^* \\ & - (C_{LL}^S - C_{RL}^S)^* [0.099 C_{LL}^T - 0.054 (C_{LL}^V - C_{RL}^V)] \\ & + (C_{RR}^T) [0.146 C_{RR}^V - 0.478 C_{LR}^V]^* - (C_{LL}^T)^* [0.146 (C_{LL}^V) - 0.478 C_{RL}^V] \\ & - (C_{LR}^V) [0.081 C_{RR}^T]^* + (C_{RL}^V)^* [0.081 C_{LL}^T] \\ & - (C_{RR}^V) [0.071 C_{RR}^T]^* + (C_{LL}^V)^* [0.071 C_{LL}^T] \} \end{aligned}$$

The $\mathcal{P}_T^{(*)}$ observables are particularly interesting to measure as they can provide us with a way to hunt for CP-violation in B -meson decays. The SM prediction for these observables is zero. In this work we focus on the $\mathcal{P}_T^{(*)}$ observables for the \bar{B} meson decay. Due to its CP-odd nature, the associated observables in the decay of B mesons can be obtained by complex conjugation of all the WCs, i.e. an overall sign.

4.2.3 Overview of the Experimental Results and Proposals

So far the only asymmetry observable studied experimentally is \mathcal{P}_τ^* , by Belle in a series of works [9, 170, 171]. The missing energy in these decays prevents us from fully reconstructing all the momenta and thus complicates the measurement of different angular observables. However, Belle was able to extract \mathcal{P}_τ^* from single-prong τ decays, $\tau \rightarrow d\nu$ with $d = \pi, \rho$, using the observation that the differential decay rate of $\bar{B} \rightarrow D^* \tau \nu$, $\tau \rightarrow d\nu$ can be written as

$$\frac{1}{\Gamma} \frac{d\Gamma}{d\theta_{\text{hel}}} = \frac{1}{2} (1 + \alpha_d \mathcal{P}_\tau^* \cos \theta_{\text{hel}}), \quad (4.21)$$

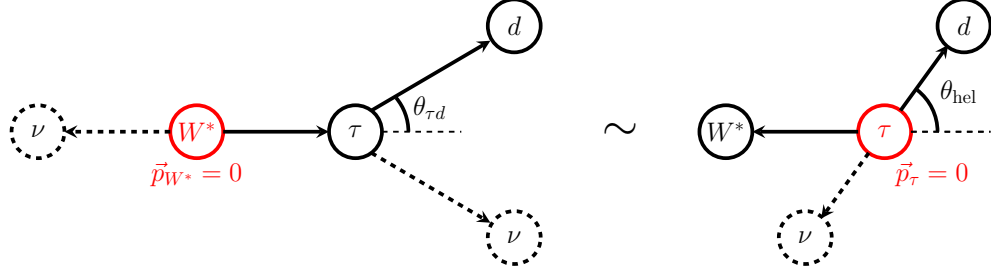


Figure 4.4: A schematic showing the Lorentz boost that relates the angles $\theta_{\tau d}$ in the q^2 frame on the left and θ_{hel} in the τ rest frame on the right. The former angle is reconstructible at the B -factories, while the latter is used to extract $\mathcal{P}_\tau^{(*)}$. Although the τ momentum vector cannot be fully reconstructed at the B factories, its magnitude is measurable, and this is sufficient to relate the two frames.

where θ_{hel} is the angle between d and the opposite of the W^* direction in the τ rest frame, see Fig. 4.4. The constant α_d captures the sensitivity to \mathcal{P}_τ^* of the particular τ decay channel under study.

Unfortunately, the τ rest frame is not reconstructible, even at the B -factories. What is reconstructible is the q^2 frame, i.e. the leptonic center of mass frame, by boosting to the frame where the (fully measurable) B and D^* momenta are pointed in the same direction. Furthermore, in the q^2 frame, the angle $\theta_{\tau d}$ between the τ and its daughter meson d is given by

$$\cos \theta_{\tau d} = \frac{2E_\tau E_d - m_\tau^2 - m_d^2}{2|\vec{p}_\tau||\vec{p}_d|}. \quad (4.22)$$

The RHS is completely known, because the magnitude of the τ momentum is a function of q^2 in the q^2 frame

$$|\vec{p}_\tau| = \frac{q^2 - m_\tau^2}{2\sqrt{q^2}}. \quad (4.23)$$

As evident from Fig. 4.4, the angle $\theta_{\tau d}$ is related to θ_{hel} via a boost along the τ momentum direction. Although we do not know the direction, it is enough to know

the magnitude:

$$|\vec{p}_d^\tau| \cos \theta_{\text{hel}} = -\gamma \frac{|\vec{p}_\tau|}{E_\tau} E_d + \gamma |\vec{p}_d| \cos \theta_{\tau d}, \quad (4.24)$$

where $|\vec{p}_d^\tau| = (m_\tau^2 - m_d^2)/(2m_\tau)$ is the momentum of the daughter meson in the τ rest frame, and $\gamma = E_\tau/m_\tau$. This relation determines θ_{hel} in terms of all measurable quantities, and allowed Belle to obtain a measurement of $\mathcal{P}_\tau^* = -0.38 \pm 0.51_{-0.16}^{+0.21}$ (compared to a SM prediction of $(\mathcal{P}_\tau^*)_{\text{SM}} = -0.497$).

Although this method works, it resulted in an enormous uncertainty, and has so far only been applied to \mathcal{P}_τ^* . There are further proposals in the literature on how we can infer additional asymmetry observables from the angular distribution of the visible daughter mesons in the τ lepton decays. In particular, [41] puts forward methods for measuring \mathcal{P}_τ , \mathcal{P}_\perp , and \mathcal{A}_{FB} in $B \rightarrow D\tau\nu$ decays (with $\tau \rightarrow d\nu$), claiming a better attainable precision than the Belle procedure described above.

In their method, q^2 , E_d , and the angle θ_d between d and D – all evaluated in the q^2 frame, and all directly measurable – are used to express the differential decay rates,

$$\frac{d^3\Gamma}{dq^2 dE_d d\cos\theta_d} = \mathcal{B}_d \frac{\mathcal{N}}{2m_\tau} \left(I_0(q^2, E_d) + I_1(q^2, E_d) \cos\theta_d + I_2(q^2, E_d) \cos^2\theta_d \right), \quad (4.25)$$

where \mathcal{B}_d is the branching ratio of τ into the daughter meson under study, \mathcal{N} is a normalization factor, and $I_{0,1,2}$ are functions of q^2 and E_d defined in [41]. After integrating over θ_d , adding together or subtracting the decay rates into the two spatial hemispheres give rise to double distributions, from which \mathcal{P}_τ , \mathcal{P}_\perp and \mathcal{A}_{FB} can be extracted.

In Tab. 4.2, we list the projected Belle II sensitivity claimed in [41] (which we also adopt in this work), as well as our calculation for the SM predictions. Although there are currently no analogous proposals to measure the D^* asymmetry observables in the literature, we believe that a similar method to the one proposed in [41] should be applicable.

Observable	\mathcal{A}_{FB}	\mathcal{A}_{FB}^*	\mathcal{P}_τ	\mathcal{P}_τ^*	\mathcal{P}_\perp	\mathcal{P}_\perp^*	\mathcal{P}_T	\mathcal{P}_T^*
SM value	-0.360	0.063	0.325	-0.497	-0.842	-0.499	0	0
Projected Precision [41]	10%	—	3%	—	10%	—	—	—

Table 4.2: The Asymmetry Observables studied in this work, our numerical calculation for the prediction in the SM, and the projected Belle II sensitivity (assuming the 50 ab^{-1} full data set) where available. We use these observables to identify different explanations of the anomalies. In the upcoming sections we will assume the observables in $B \rightarrow D^* \tau \nu$ are measured with the same uncertainty as in $B \rightarrow D \tau \nu$.

At present, there is no substantiative experimental proposal for how to measure $\mathcal{P}_T^{(*)}$ at Belle II.⁵ However, we have included it in our study, owing to the important role it can play in distinguishing certain models from one another (see the next section), and in the hopes that viable proposals for how to measure it will emerge in the future.

4.3 Distinguishing Different Solutions

Having calculated these asymmetry observables, we now use them to distinguish between different simplified models for the $R_{D^{(*)}}$ anomalies (see Sec. 4.1). As the range of possible WCs depends on the value of R_D and R_{D^*} after the Belle II data set is collected, we consider the two benchmark scenarios described in Sec. 4.1.4 and indicated in Figs. 4.1 and 4.2.

⁵In [40] it has been shown that the total decay rates above and their dependence on the azimuthal angle χ between the two planes in Fig. 4.3 contains information about $\mathcal{P}_T^{(*)}$. We cannot confirm the claim that this angle is experimentally accessible and are not aware of any experimental proposals for its measurement at Belle II.

4.3.1 10σ Scenario

In this scenario, for the models involving the LH neutrinos, the LQ U_1 , as well as the single operators \mathcal{O}_{LL}^T and \mathcal{O}_{RL}^V , will be able to explain the anomalies while satisfying the experimental bounds mentioned above. Among the RH neutrino proposals, only U_1 LQ will remain viable.

Fig. 4.5 shows the ranges of CP-even asymmetry observables that are achievable in each model, projected here into 2D plots, one for each pair of observables. In each model, we have scanned over the (complex) WCs of the model, subject to the following constraints: R_D and R_{D^*} should be within the 2σ Belle II error ellipse for this scenario; $Br(B_c \rightarrow \tau\nu) < 10\%$. The gray regions in each plot denote the Belle II projected relative uncertainty from Tab. 4.2 centered around the SM prediction; for the observables in the $\bar{B} \rightarrow D^*\tau\nu$ process, as there are no available projection, we assume the same relative uncertainties as in the $\bar{B} \rightarrow D\tau\nu$ decay. Models affected by the $b \rightarrow s\nu\nu$ bounds are already ruled out in this scenario and are not included in Fig. 4.5.

It is obvious from Fig. 4.5 that by measuring all these observables we can distinguish well each individual model. In particular, the observables $\mathcal{P}_\tau^{(*)}$ and \mathcal{A}_{FB}^* are the most promising discriminators. This conclusion would remain unchanged even if we had applied the looser $Br(B_c \rightarrow \tau\nu) < 30\%$ bound.

4.3.2 5σ Scenario

In our second scenario for the outcome of Belle II measurements, we study the situation in which the observed values of the $R_{D^{(*)}}$ anomalies in the Belle II data are reduced significantly from the present average, but still significant enough to be claimed as a 5σ discovery, see Section 4.1.4 for details. With the reduced values of $R_{D^{(*)}}$, many more models become viable. The minimal models with the R_2 , S_1 , or U_1 LQs, as well as the individual operators C_{LL}^T and C_{RL}^V can explain the anomalies

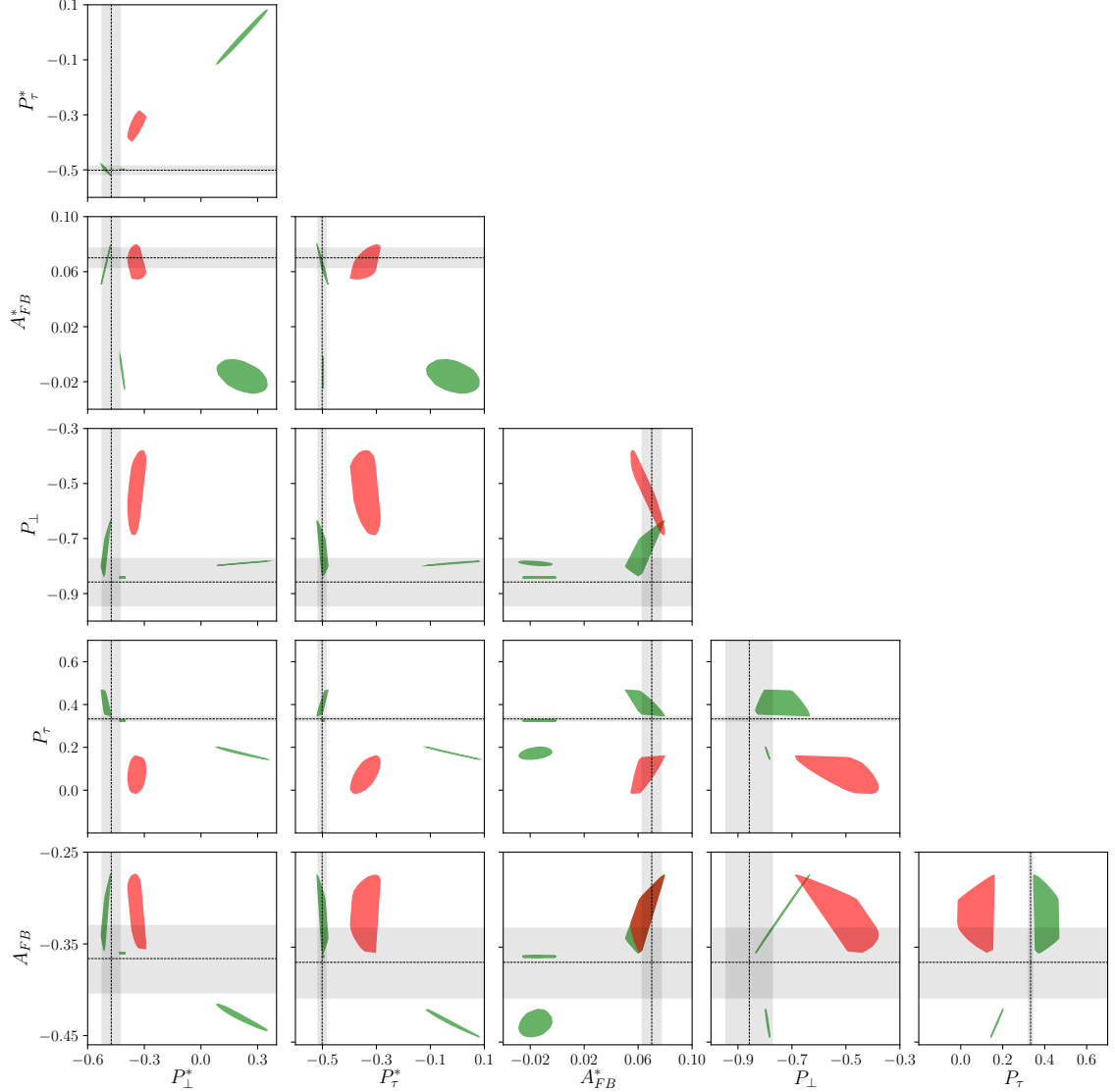


Figure 4.5: Two-dimensional plots of asymmetry observables for the 10σ scenario. We scan over WCs that result in $R_{D^{(*)}}$ values within the 2σ Belle II error ellipse centered on the present-day world averages. We also impose the $Br(B_c \rightarrow \tau\nu) \leq 10\%$ bound [52]. The projected Belle II precision for each observable, centered on the SM prediction, is indicated by the dashed gray lines, see the text. Regions which can be realized by models with LH SM neutrinos (shown in green) are from U_1 LQ and single operators \mathcal{O}_{LL}^T and \mathcal{O}_{RL}^V , while the one requiring new RH neutrinos (shown in red) corresponds to U_1 LQ. We can distinguish all the models from one another by measuring these asymmetry observables.

with a LH neutrino in the decay. For the solutions with the RH neutrinos, a U_1 or a S_1 LQ, a W' , or the single operator C_{LR}^V are viable. Given the severe constraints from the $b \rightarrow s\nu\nu$ processes, the S_1 LQ and the W' mediators coupled to RH neutrinos are degenerate; since these two mediators generate a subset of operators generated by a U_1 LQ (C_{RR}^V), it is impossible to distinguish these three mediators from one another.

Similar 2D plots for this scenario as in the previous one are included in Fig. 4.6. We see immediately that the various regions are much closer together than in Fig. 4.5, as expected from the reduced requirement from $R_{D^{(*)}}$. Combining the results in different plots shows that we can still distinguish different neutrino chiralities (the green regions vs. the red ones) from each other. The best plots that can collectively illustrate this point (again, highly contingent on the projected precision of the Belle II measurement) are $\mathcal{P}_\tau - \mathcal{A}_{FB}^*$, $\mathcal{P}_\tau - \mathcal{P}_\tau^*$, $\mathcal{A}_{FB}^* - \mathcal{P}_\tau^*$, and $\mathcal{A}_{FB}^* - \mathcal{P}_\perp^*$.

While we can still discern models with different neutrino chiralities, it is not immediately obvious if we can distinguish models with the same type of neutrinos from each other. To quantify how well we can separate these models, we use a crude χ^2 measure that includes the six CP-even asymmetry observables from Fig. 4.6 as well as the $R_{D^{(*)}}$ ratios themselves, for a total of 8 *d.o.f.*. As there are no data available at this point, the correlation between different asymmetry observables (and $R_{D^{(*)}}$) is not known; we neglect these correlations in this χ^2 estimation and only use the current $\rho_{\text{corr}} = -0.2$ between the $R_{D^{(*)}}$ ratios. We calculate this χ^2 between all pairs of scanned points from the models that we want to distinguish. We use the relative uncertainties from Tab. 4.2 in this calculation; as there are no projections for the precision in measuring the quantities in $\bar{B} \rightarrow D^* \tau \nu$, we use the same relative uncertainty as their counterparts in $\bar{B} \rightarrow D \tau \nu$ from Tab. 4.2 in our calculation.

Our χ^2 estimation corroborates the conclusion from Fig. 4.6 that with measuring all CP-even observables we can distinguish models with different neutrinos from

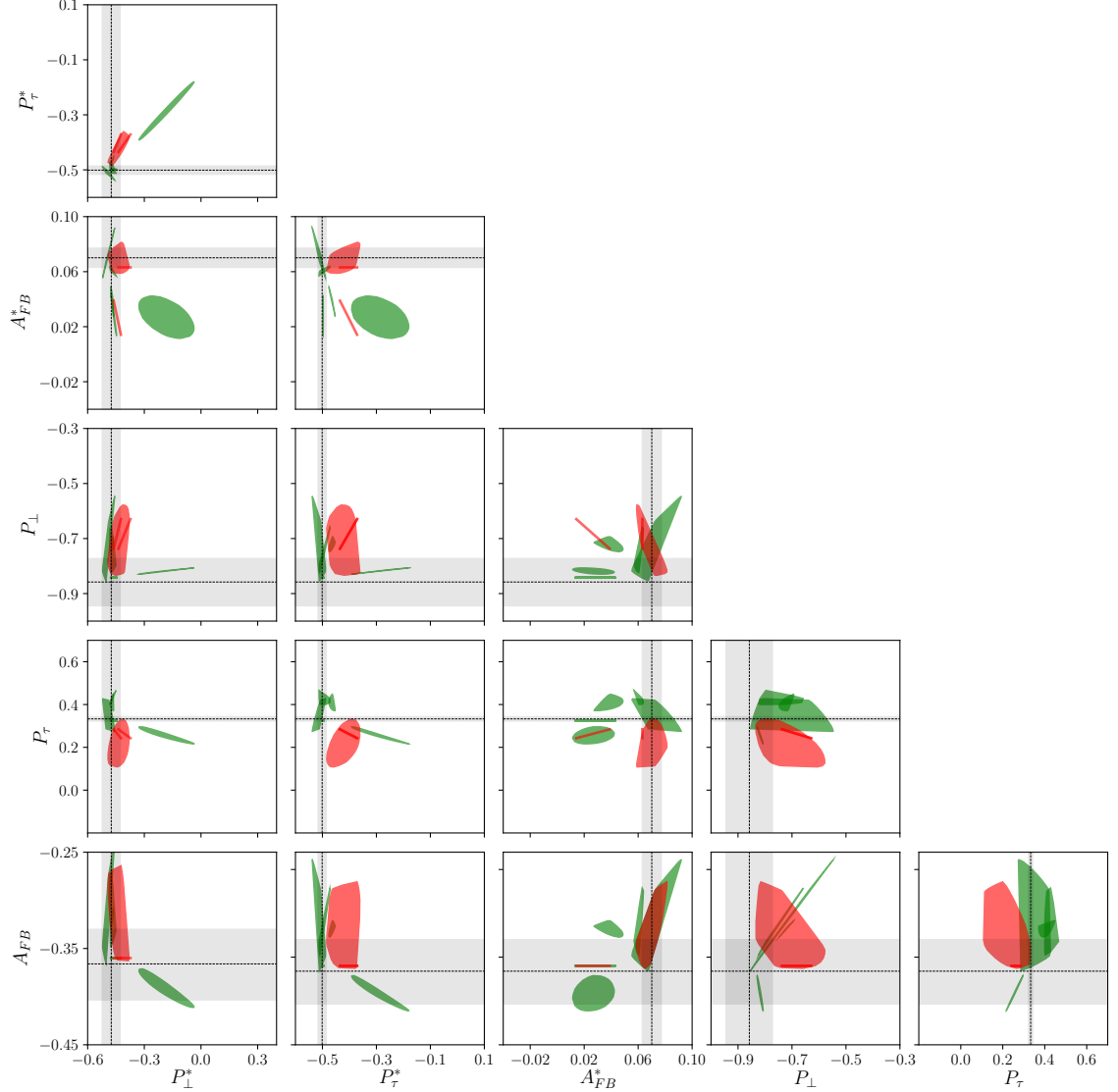


Figure 4.6: Two-dimensional plots of asymmetry observables in the 5σ scenario. We scan over WCs which result in $R_{D^{(*)}}$ values within the 2σ Belle II error ellipse centered at $R_D = 0.34$ and $R_{D^*} = 0.275$. We also impose the $b \rightarrow s\nu\nu$ bound [119, 155] and the $Br(B_c \rightarrow \tau\nu) \leq 10\%$ bound [52]. The projected Belle II precision for each observable, centered on the SM prediction, is indicated by the dashed gray lines, see the text. All the currently viable models and single operators remain viable in this scenario. Regions which can be realized by models with LH SM neutrinos are shown in green, while those requiring new RH neutrinos are in red.

each other.⁶ However, depending on the outcome of the measurements, it may not be possible to discern individual models with similar neutrino chiralities from one another.

As noted before, the three possible mediators coupled to RH neutrinos (U_1 and S_1 LQs, and a W') give rise to identical or overlapping parameter spaces, and thus cannot be distinguished from one another on the basis of this effective Hamiltonian alone. Our χ^2 measure, however, indicates that we can distinguish them from the single operator C_{LR}^V .

Our χ^2 estimate further shows that we can distinguish all the viable mediators with LH neutrinos (U_1 , S_1 , and R_2 LQs) from the individual operators with the same type of neutrinos (C_{LL}^T and C_{RL}^V). However, there exist some outcomes where different viable heavy mediators (U_1 , S_1 , and R_2 LQs) can not be told apart.

In Tab. 4.3 we list benchmark pairs of measurement outcomes in which pairs of mediators S_1 , U_1 , or R_2 coupled to LH neutrinos, are not distinguishable. Here we take one of the operators to have real WCs without loss of generality, since the observables are insensitive to an overall rephasing of all the WCs. The C^S and C^V refer to different scalar and vector WCs for the different models; see Tab. 4.1 for details.

These benchmark points illustrate that the six CP-even asymmetry observables are not enough to completely break the degeneracy between the S_1 , U_1 , and R_2 LQs when they are coupled to LH neutrinos. However, we still have a pair of observables at our disposal that could distinguish these models: \mathcal{P}_T and \mathcal{P}_T^* . After our χ^2 estimation with all eight CP-even observables, we keep the points from pairs of these LQ models that are less than 1σ apart from each other and study their contribution to the CP-odd

⁶The closest points from two solutions with different neutrino chiralities belong to the C_{LL}^T and the C_{LR}^V individual operator solutions, with a minimum separation of $2.1 \chi^2/d.o.f.$ For the heavy mediator solutions the closest pair of points belong to the U_1 LQ models coupled to different types of neutrinos, with the minimum separation of $3.4 \chi^2/d.o.f.$

Model	(C^S, C^V)	$R_D [\pm 0.010]$	$\mathcal{A}_{FB} [\pm 0.037]$	$\mathcal{P}_\tau [\pm 0.010]$	$\mathcal{P}_\perp [\pm 0.086]$	$\Delta\chi^2/d.o.f$
		$R_{D^*} [\pm 0.005]$	$\mathcal{A}_{FB}^* [\pm 0.007]$	$\mathcal{P}_\tau^* [\pm 0.015]$	$\mathcal{P}_\perp^* [\pm 0.048]$	
S_1^L LQ	$(0.062 + 0.065i, 1.005)$	0.333	-0.347	0.402	-0.823	1.14
		0.262	0.060	-0.510	-0.478	
U_1^L LQ	$(0.041 + 0.076i, 1.017)$	0.332	-0.354	0.376	-0.830	
		0.263	0.060	-0.498	-0.514	
Model	(C^S, C^V)	$R_D [\pm 0.010]$	$\mathcal{A}_{FB} [\pm 0.037]$	$\mathcal{P}_\tau [\pm 0.010]$	$\mathcal{P}_\perp [\pm 0.086]$	$\Delta\chi^2/d.o.f$
		$R_{D^*} [\pm 0.005]$	$\mathcal{A}_{FB}^* [\pm 0.007]$	$\mathcal{P}_\tau^* [\pm 0.015]$	$\mathcal{P}_\perp^* [\pm 0.048]$	
S_1^L LQ	$(0.011 + 0.371i, 1.006)$	0.362	-0.288	0.441	-0.697	1.16
		0.265	0.061	-0.484	-0.466	
R_2 LQ	$(-0.002 - 0.37i, .)$	0.352	-0.320	0.428	-0.727	
		0.261	0.048	-0.474	-0.475	
Model	(C^S, C^V)	$R_D [\pm 0.010]$	$\mathcal{A}_{FB} [\pm 0.037]$	$\mathcal{P}_\tau [\pm 0.010]$	$\mathcal{P}_\perp [\pm 0.086]$	$\Delta\chi^2/d.o.f$
		$R_{D^*} [\pm 0.005]$	$\mathcal{A}_{FB}^* [\pm 0.007]$	$\mathcal{P}_\tau^* [\pm 0.015]$	$\mathcal{P}_\perp^* [\pm 0.048]$	
U_1^L LQ	$(0.052 + 0.113i, 1.013)$	0.338	-0.350	0.393	-0.819	1.13
		0.261	0.059	-0.495	-0.515	
R_2 LQ	$(-0.022 - 0.335i, .)$	0.331	-0.326	0.396	-0.746	
		0.263	0.046	-0.473	-0.477	

Table 4.3: Pairs of benchmark points for the LQ models S_1 , U_1 , and R_2 coupled to LH neutrinos that are less than 1σ apart in our estimation. The approximate uncertainties using Tab. 4.2 are quoted in the first row as well. We need further measurements to distinguish these models in these cases.

observables $\mathcal{P}_T^{(*)}$. The results are depicted in Fig. 4.7. Given a reasonable precision, say $\delta\mathcal{P}_T^{(*)} \sim 0.1$, these observables are able to resolve the different degenerate models, apart from the special case where the models are CP even.

To recap, in this scenario, measurement of the CP-even asymmetry observables at Belle II, for which theoretical proposals exist [41], can easily discern the models of different types of neutrinos. Models with the same type of neutrinos can be distinguished in many (but not all) cases using the same CP-even measurements or with the additional measurement of CP-odd polarization asymmetries $\mathcal{P}_T^{(*)}$.

4.4 Final Remarks

In this chapter we studied various τ asymmetry observables that can potentially be measured at Belle II and that could help to resolve the BSM origin of the long-standing $R_{D^{(*)}}$ anomalies. In (4.15) and (4.18)–(4.20), we reported numerical formulas for the τ forward-backward asymmetry $\mathcal{A}_{FB}^{(*)}$ and polarization asymmetries $P_\tau^{(*)}$, $P_\perp^{(*)}$, and $P_T^{(*)}$, as a function of all relevant dimension 6 Wilson coefficients (including those for RH neutrinos). The analytic formulas from which our numerical results are derived are included in App. D. While similar analytic formulas existed in the literature previously, here we report the contribution of the massless RH neutrinos as well.

We also catalogued all the simplified models involving both LH and RH neutrinos that explain the $R_{D^{(*)}}$ anomalies and are not ruled out by the severe $Br(B_c \rightarrow \tau\nu)$ and $b \rightarrow s\nu\nu$ constraints, see Tab. 4.1. We then showed that, using the CP-even asymmetry observables $\mathcal{A}_{FB}^{(*)}$, $P_\tau^{(*)}$, $P_\perp^{(*)}$ for which proposed measurement methods exist, it is possible to tell apart solutions with different types of neutrinos (SM LH vs. RH sterile ones) from one another, see Fig. 4.5 and Fig. 4.6. In most instances, it is even possible to tell apart different mediators with the same neutrino chirality. The most useful observables for this purpose were $P_\tau^{(*)}$, followed by $P_\perp^{(*)}$ and $\mathcal{A}_{FB}^{(*)}$.

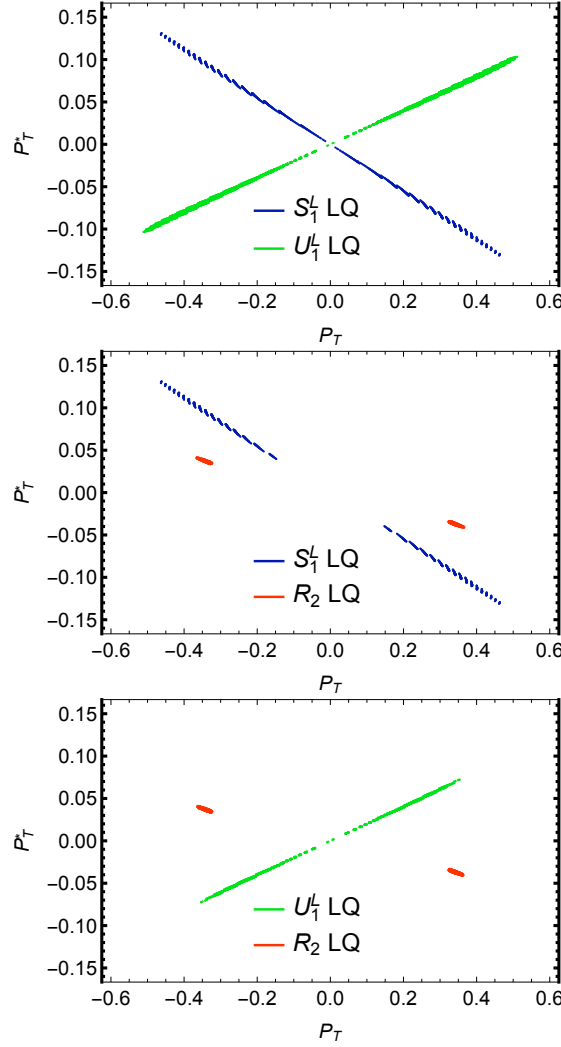


Figure 4.7: The \mathcal{P}_T and \mathcal{P}_T^* observables for the points from Fig. 4.6 that are less than 1σ apart in our estimation. These figures indicate that the CP-odd asymmetries \mathcal{P}_T and $\mathcal{P}_T^{(*)}$ may be useful for further distinguishing the R_2 , U_1 , and S_1 leptoquark models coupled to LH neutrinos; however, the fact that they cross at the origin in the left figure also indicates that these asymmetries cannot resolve the difference in all cases.

In some of the most difficult cases, the CP-even asymmetries are not enough. Here we show that the information carried in the CP-odd asymmetries $\mathcal{P}_T^{(*)}$ plays a further, crucial role in distinguishing different models. As these observables do not yet have a fully-developed experimental strategy, our results provide a strong motivation to construct one.

Our ability to distinguish between different BSM models for the $R_{D^{(*)}}$ anomalies depends on what Belle II actually measures for $R_{D^{(*)}}$. If Belle II measures the $R_{D^{(*)}}$ ratios near the present values, see Eq. (1.3), with much smaller error bars, then this measurement alone will greatly reduce the number of viable new physics models with either left- or right-handed neutrinos, compared to the present situation. In this case, it will be relatively straightforward to distinguish different models from one another using asymmetry observables. If instead, Belle II finds $R_{D^{(*)}}$ ratios which are closer to the Standard Model prediction, while still constituting a 5σ discovery of new physics, then more models remain viable, and distinguishing between them becomes more difficult. However, in either scenario, we show that it is at least possible to distinguish between models with LH neutrinos and models with RH neutrinos through measurement of CP-even asymmetry observables.

Additionally, although we have focused on measuring these observables at Belle II in this chapter, one can also consider the possibilities of doing this at LHCb. There are various reasons that suggest that LHCb will have significant difficulty in measuring these quantities with reasonable precision – in particular lack of knowledge of the initial rest frame and generally higher background. However, it is conceivable that high statistics at LHCb and lower-background decay channels like $\tau \rightarrow l\nu\nu$ may be leveraged to obtain comparable precision in the measurement of these angular asymmetries.

Furthermore, in this chapter we focused on the asymmetry observables in the $B \rightarrow D^{(*)}\tau\nu$. Similar observables can be measured in the related decay of $B_c \rightarrow J/\psi\tau\nu$. As

there is already a fluctuation in this decay, captured by the ratio $R_{J/\psi}$ defined earlier, it is interesting to investigate the τ polarization and forward-backward asymmetry in that decay too.

Chapter 5

Outlook

The charged current anomalies in various flavor experiments are one of our best guides for BSM physics. These anomalies are observed in the measurement of R_D , R_{D^*} , $R_{J/\psi}$, and $F_{D^*}^L$, the underlying hard process for all of which is $b \rightarrow c\tau\nu$. Motivated by these observations, various extensions of the SM have been proposed.

With the LHCb and Belle II working on these anomalies, we expect to have enough data in 2-3 years to be able to decide if these anomalies are due to NP or not. Given these experimental activities, the theory community should carry out an in-depth study of all the relevant models and observables to catalog different signatures that the experimental studies could be focusing on.

In this work we introduced two possible new solutions to these anomalies. Each of these new solutions leverages interesting, and hitherto unexplored, ideas in BSM model buildings and can have further predictions for other observables.

The novel point in the first proposal is the introduction of a new W' and RH neutrinos as the missing energy in the decay. While a W' mediator or RH neutrinos had been studied in the literature before, our model is the first proposal that combines the interesting features of these two extensions of the SM to generate a viable solution for these anomalies. The W' in our model originates from breaking of a new $SU(2) \times U(1)$ gauge group down to the SM $U(1)_Y$. We showed that our setup gives rise to very unique signatures not only in the flavor experiments, but also in various other collider studies.

In the second model we extend the $SU(2)_L$ symmetry of the SM to $SU(2)_L \times$

$SU(2)_R \times U(1)_X$ and rely on a bifundamental of the two $SU(2)$ s to generate the dimension six operators \mathcal{O}_{RL}^V or \mathcal{O}_{LR}^V to explain the anomalies. Prior to our model, there were no models in the literature generating these operators.

This model is specially interesting in the light of the recent measurement of $F_{D^*}^L$. We showed in Chap. 3 that any proposal trying to explain $F_{D^*}^L$ should envision a way for generating \mathcal{O}_{RL}^V or \mathcal{O}_{LR}^V . Our setup is the only viable proposal generating these operators, which automatically makes it the only viable solution to the observed $F_{D^*}^L$ fluctuation.

Both these models can evade various experimental constraints. These constraints include direct collider searches, precision measurements of the electroweak processes, and various flavor physics bounds ($B_c \rightarrow \tau\nu$ branching ratio, $B \rightarrow K^{(*)}\nu\nu$ branching ratios, $B - \bar{B}$ and $D_s - \bar{D}_s$ meson mixings, etc.).

Finally, we proposed a way to discern various solutions from one another through further measurement of other related observables. In particular, we studied the polarization asymmetry and forward-backward asymmetry of the τ lepton in the $B \rightarrow D^{(*)}\tau\nu$ process and showed that if the observed anomalies are due to NP, these observables can distinguish between almost all different BSM solutions.

Of all these asymmetry observables, so far only the longitudinal τ polarization asymmetry in $B \rightarrow D^*\tau\nu$ (\mathcal{P}_τ^*) has been measured. Our study highlighted the importance of measuring the rest of these observables in Belle II and LHCb. In particular, we indicated the important role of the CP-odd observables $\mathcal{P}_T^{(*)}$ for which there are no viable measurement proposals yet. We hope our results motivate the experimental community to start studying this observable as a viable measure of CP-violation in these decays.

There are various possible ways the theoretical studies around $R_{D^{(*)}}$ can be extended. We conclude this thesis with listing a handful of such possibilities.

- It is always interesting to think about possible new solutions and what other

novel signatures they can give rise to.

- In particular, it would be interesting to investigate the relationship between these anomalies and the hierarchy problem, unification of SM gauge groups, the yukawa hierarchy problem, the nature of dark matter and its portal to the SM, the origin of the neutrinos mass, or any other shortcoming of the SM listed in Chap. 1.
- There are a handful of other anomalies observed in the flavor experiments. A unified explanation of the anomalies studied here and other flavor anomalies is indeed well-motivated. While a few studies have been done in this front, a comprehensive study of all possible joint explanations of different anomalies in the data is still undelivered.
- Given the on-going experimental efforts, it is interesting to look for related observables, how we can measure them, and how precisely this measurement can be done. For instance, while there are projections for how precisely the asymmetry observables from Chap. 4 in $B \rightarrow D\tau\nu$ can be measured, the equivalent study for the $B \rightarrow D^*\tau\nu$ decay is in order.
- Furthermore, as we argued in Chap. 4, there are currently no proposals for measuring the CP-odd observables $\mathcal{P}_T^{(*)}$. Given the importance of this observable in distinguishing different models and the fact that there are currently no other handles on CP-violation in these decays, it is interesting to further investigate new proposals for this measurement.
- In this thesis we focused on the prospects of the Belle II experiment for measuring different asymmetry observables. It would be interesting to study the prospects of similar measurements at LHCb as well.
- Any new solution to the anomalies will require new mediators beyond the SM.

These mediators will have further signatures in other collider searches. It is interesting to study all the possible signatures of different mediators to catalog different collider signals that should be looked for in any of the solutions of the anomalies.

Appendix A

Leptonic and Hadronic Functions

In [58, 68], the physics of the leptonic and the hadronic side of the processes in the $R_{D^{(*)}}$ anomalies are factorized and the relevant matrix elements are calculated. We use the leptonic and the hadronic matrix elements reported therein in our work. However, as we are working with right-handed neutrinos, one needs to calculate a few more matrix elements. In this appendix we report the new leptonic matrix elements involving right-handed neutrinos, and the new hadronic matrix element with tensor current.

The leptonic matrix elements are defined as

$$Lr^{\lambda_\tau} = 2\langle\tau(p_\tau, \lambda_\tau)\bar{\nu}|\bar{\tau}P_R\nu|0\rangle, \quad (\text{A.1})$$

$$Lr_{\bar{\lambda}}^{\lambda_\tau} = 2\epsilon_\mu(\bar{\lambda})\langle\tau(p_\tau, \lambda_\tau)\bar{\nu}|\bar{\tau}\gamma^\mu P_R\nu|0\rangle, \quad (\text{A.2})$$

$$Lr_{\bar{\lambda}\bar{\lambda}'}^{\lambda_\tau} = -2i\epsilon_\mu(\bar{\lambda})\epsilon_\nu(\bar{\lambda}')\langle\tau(p_\tau, \lambda_\tau)\bar{\nu}|\bar{\tau}\sigma^{\mu\nu}P_R\nu|0\rangle, \quad (\text{A.3})$$

where $\bar{\lambda}$ (λ_τ) denotes the polarization of the mediator (τ lepton). We use the same convention for the ϵ as [70]. Explicitly carrying out the calculation, we find the following results for different polarizations.

$$Lr^+ = 0, \quad (\text{A.4})$$

$$Lr^- = 2\sqrt{q^2}v. \quad (\text{A.5})$$

$$Lr_{\pm}^{+} = -\sqrt{2}\sqrt{q^2}v(1 \mp \cos \theta) \quad (\text{A.6})$$

$$Lr_0^{+} = -2\sqrt{q^2}v \sin \theta \quad (\text{A.7})$$

$$Lr_t^{+} = 0 \quad (\text{A.8})$$

$$Lr_{\pm}^{-} = \mp \sqrt{2}m_{\tau}v \sin \theta \quad (\text{A.9})$$

$$Lr_0^{-} = -2m_{\tau}v \cos \theta \quad (\text{A.10})$$

$$Lr_t^{-} = 2m_{\tau}v, \quad (\text{A.11})$$

$$Lr_{\lambda\lambda}^{\pm} = 0, \quad (\text{A.12})$$

$$Lr_{\lambda\lambda'}^{\pm} = -Lr_{\lambda'\lambda}^{\pm}, \quad (\text{A.13})$$

$$Lr_{0\pm}^{+} = \mp \sqrt{2}m_{\tau}v(1 \mp \cos \theta), \quad (\text{A.14})$$

$$Lr_{+-}^{+} = -Lr_{t0}^{+} = 2m_{\tau}v \sin \theta, \quad (\text{A.15})$$

$$Lr_{\pm t}^{+} = \sqrt{2}m_{\tau}v(1 \mp \cos \theta), \quad (\text{A.16})$$

$$Lr_{0\pm}^{-} = -\sqrt{2}\sqrt{q^2}v \sin \theta, \quad (\text{A.17})$$

$$Lr_{+-}^{-} = -Lr_{t0}^{-} = 2\sqrt{q^2}v \cos \theta, \quad (\text{A.18})$$

$$Lr_{\pm t}^{-} = \pm \sqrt{2}\sqrt{q^2}v \sin \theta, \quad (\text{A.19})$$

where θ is again the angle between the τ lepton and the $D^{(*)}$ in the leptonic system rest-frame, see Fig. 4.3, and $v = \sqrt{1 - m_{\tau}^2/q^2}$. The subscript t refers to the fourth polarization of a virtual W . These leptonic functions are related to the ones involving the LH neutrinos in [58] through parity transformation.

For the hadronic side of the matrix element, we use the notation from [68] and define

$$\begin{aligned} H_{V,0}^s(q^2) &\equiv H_{V1,0}^s(q^2) = H_{V2,0}^s(q^2), \\ H_{V,t}^s(q^2) &\equiv H_{V1,t}^s(q^2) = H_{V2,t}^s(q^2), \\ H_S^s(q^2) &\equiv H_{S1}^s(q^2) = H_{S2}^s(q^2), \\ H_T^s(q^2) &\equiv H_{T,+-}^s(q^2) = H_{T,0t}^s(q^2) = -H_{T2,+-}^s(q^2) = H_{T2,0t}^s(q^2). \end{aligned} \quad (\text{A.20})$$

$$\begin{aligned}
H_{V,\pm}(q^2) &\equiv H_{V1,\pm}^\pm(q^2) = -H_{V2,\mp}^\mp(q^2), \\
H_{V,0}(q^2) &\equiv H_{V1,0}^0(q^2) = -H_{V2,0}^0(q^2), \\
H_{V,t}(q^2) &\equiv H_{V1,t}^0(q^2) = -H_{V2,t}^0(q^2), \\
H_S(q^2) &\equiv H_{S1}^0(q^2) = -H_{S2}^0(q^2), \\
H_{T,\pm}(q^2) &\equiv H_{T,\pm 0}^\pm = \pm H_{T,\pm t}^\pm(q^2), \\
H_{T2,\pm}(q^2) &\equiv H_{T2,\pm 0}^\pm = \mp H_{T2,\pm t}^\pm(q^2), \\
H_{T,0}(q^2) &\equiv H_{T,+-}^0(q^2) = H_{T,0t}^0(q^2) = H_{T2,+-}^0(q^2) = -H_{T2,0t}^0(q^2).
\end{aligned} \tag{A.21}$$

The hadronic functions in (A.20) correspond to the $\bar{B} \rightarrow D\tau\nu$ decay, while those in (A.21) correspond to the $\bar{B} \rightarrow D^*\tau\nu$ decay. The superscripts 0 and \pm in (A.21) stand for the D^* polarization, while the subscripts 0, \pm , and t refer to the virtual mediator polarization. The subscripts S , V , and T refer to the scalar, vector, and tensor currents, respectively.

In the $\bar{B} \rightarrow D\tau\nu$ hadronic functions, we use the same form factors as in [39] (derived from the available lattice results [17] and from [71]); for the $\bar{B} \rightarrow D^*\tau\nu$ decay, following [39, 68], we use the heavy quark effective theory form factors based on [72].

When working with the right-handed neutrino models for $R_{D^{(*)}}$, there is one new hadronic function, namely

$$\langle D^{(*)} | \bar{c}\sigma^{\mu\nu}(1 + \gamma^5)b | B \rangle, \tag{A.22}$$

where $\sigma^{\mu\nu} = i/2[\gamma^\mu, \gamma^\nu]$. To calculate this matrix element, we can simply borrow the results in [68] for the hadronic side of the operator \mathcal{O}_{LL}^T ($\bar{c}\sigma^{\mu\nu}(1 - \gamma^5)b$ operator) and merely flip the sign of the axial current. The resulting hadronic functions, denoted by H_{T2} , will be

$$H_{T2,+-}^s(q^2) = -H_{T2,0t}^s(q^2) = -H_{T,+-}^s(q^2), \tag{A.23}$$

where the superscript s indicates that these functions are corresponding to D meson

and H_T functions are defined in [68], and

$$\begin{aligned}
H_{T2,+ -}^0(q^2) &= -H_{T2,0t}^0(q^2) = H_{T,+ -}^0(q^2), \\
H_{T2,\pm 0}^\pm(q^2) &= \mp H_{T2,\pm t}^\pm(q^2) \\
&= \frac{\sqrt{m_B m_{D^*}}}{\sqrt{q^2}} A_1(w) \left(\pm(m_b - m_c)(w + 1) - (m_b + m_c)\sqrt{w^2 - 1} R_1(w) \right), \\
H_{T2,\lambda_1 \lambda_2}^{\lambda_M}(q^2) &= -H_{T2,\lambda_2 \lambda_1}^0(q^2),
\end{aligned} \tag{A.24}$$

for D^* where again the H_T functions and the form factors $A_1(w)$ and $R_1(w)$ are defined in [58, 68], m_M is the final meson (here D^*) mass, and

$$w = \frac{m_B^2 + m_M^2 - q^2}{2m_M m_B}. \tag{A.25}$$

Appendix B

Details of Fermion-Gauge Boson Couplings

In this appendix we go through the details of the Z boson couplings to the SM fermions in the model of Chap. 2, which is used in our study of the EWP tests. The relevant part of the Lagrangian is

$$\mathcal{L} \supset \bar{F}\gamma^\mu(g_X X_F B_\mu + g_V T_3^V W_\mu^{3,V})F + \bar{f}_L\gamma^\mu(g_X X_{f_L} B_\mu + g_L T_3^L W_\mu^{3,L})f_L + \bar{f}_R\gamma^\mu(g_X X_{f_R} B_\mu)f_R \quad (\text{B.1})$$

where f_R , f_L correspond to the SM-like fermions, and F to the new, heavy vector-like fermions, in the interaction basis. B_μ is the $U(1)_X$ gauge boson and $X_{F,f}$ are the $U(1)_X$ charges (given in Table 2.2).

Going to the mass basis for the gauge bosons and the fermions via Eqs. (2.11) and (2.14) respectively, we obtain the couplings of Z to SM fermions:

$$\mathcal{L} \supset g_L^{Zf} Z_\mu \bar{f}_L \gamma^\mu f_L + g_R^{Zf} Z_\mu \bar{f}_R \gamma^\mu f_R \quad (\text{B.2})$$

where

$$g_L^{Zf} = g_L(T_3^L)_f \mathcal{R}_{22}^\dagger + g_X X_{f_L} \mathcal{R}_{12}^\dagger \quad (\text{B.3})$$

and

$$\begin{aligned} g_R^{Zf} &= (g_V(T_3^V)_F \mathcal{R}_{32}^\dagger + g_X X_F \mathcal{R}_{12}^\dagger) |\mathcal{U}_{21}^f|^2 + g_X X_{f_R} \mathcal{R}_{12}^\dagger |\mathcal{U}_{22}^f|^2 \\ &= (g_V(T_3^V)_F \mathcal{R}_{32}^\dagger + g_X (X_F - X_{f_R}) \mathcal{R}_{12}^\dagger) |\mathcal{U}_{21}^f|^2 + g_X X_{f_R} \mathcal{R}_{12}^\dagger \\ &= (T_3^V)_F (g_V \mathcal{R}_{32}^\dagger - g_X \mathcal{R}_{12}^\dagger) |\mathcal{U}_{21}^f|^2 + g_X Q_f \mathcal{R}_{12}^\dagger. \end{aligned} \quad (\text{B.4})$$

Note that for the left-handed fermions, there is essentially no mixing with the vector-like states, so the coupling to the Z is relatively simple. For the right-handed fermions,

we have to take into account mixing with the vector-like states. The choice of F in Eq. (B.4) is dictated by the fermion mixing. For instance, if $f_R = c_R$ (b_R) then $F = U$ (D) and $(T_3^V)_F = \frac{1}{2}$ ($-\frac{1}{2}$). In the second line of Eq. (B.4), we have used $|\mathcal{U}_{21}^f|^2 + |\mathcal{U}_{22}^f|^2 = 1$. In the third line we have used $Q_f = X_{f_R} = X_F + (T_3^V)_F$ for right-handed fermions and the vector-like fermions that they mix with.

To proceed further, we require more explicit formulas for the gauge boson mixing matrix elements \mathcal{R}_{i2}^\dagger . By diagonalizing the mass matrix Eq. (2.10), it is straightforward to verify that

$$\mathcal{R}_{12}^\dagger = -\frac{g_Y}{g_X}c_\alpha s_w - \frac{g_Y}{g_V}s_\alpha, \quad \mathcal{R}_{22}^\dagger = c_\alpha c_w, \quad \mathcal{R}_{32}^\dagger = \frac{g_Y}{g_X}s_\alpha - \frac{g_Y}{g_V}c_\alpha s_w, \quad (\text{B.5})$$

where the Weinberg angle is defined in terms of g_Y and g_L in the same way as the SM, and

$$\tan(2\alpha) = \frac{2v_L^2 g_X^2 \sqrt{g_V^2 g_L^2 + g_X^2 g_L^2 + g_V^2 g_X^2}}{-v_V^2 (g_V^2 + g_X^2)^2 + v_L^2 (g_V^2 g_L^2 + g_X^2 g_L^2 + g_V^2 g_X^2 - g_X^4)}, \quad (\text{B.6})$$

is the effective $Z - Z'$ mixing angle (which vanishes in the $v_V \rightarrow \infty$ limit).

Then Eq. (B.3) becomes

$$g_L^{Zf} = \sqrt{g_L^2 + g_Y^2} c_\alpha \left((T_3^L)_f - Q_f \frac{g_Y^2}{g_L^2 + g_Y^2} \right) - X_{f_L} \frac{g_X g_Y}{g_V} s_\alpha \quad (\text{B.7})$$

and Eq. (B.4) becomes

$$g_R^{Zf} = -Q_f g_Y c_\alpha s_w - Q_f \frac{g_X g_Y}{g_V} s_\alpha + (T_3^V)_F s_\alpha \sqrt{g_V^2 + g_X^2} |\mathcal{U}_{21}^f|^2. \quad (\text{B.8})$$

Expanding these at large v_V and g_V we reproduce Eqs. (2.21)–(2.23) in the text.

Appendix C

Details on Maximizing the Observables

We now provide some details to our procedure. We hope these details will prove useful to others who may be interested in maximizing other observables in the future (or replicating our analysis).

The first step is to solve the equation of $\text{Br}(B_c \rightarrow \tau\nu)$ for C_{-L}^S ,

$$C_{-L}^S = \frac{1}{4.33} (e^{i\xi} \mathcal{R}_{B_c} - C_{-L}^V), \quad (\text{C.1})$$

where ξ is an arbitrary phase and we have defined

$$\mathcal{R}_{B_c} \equiv \sqrt{\frac{\text{Br}(B_c \rightarrow \tau\nu)}{\text{Br}(B_c \rightarrow \tau\nu)^{SM}}}. \quad (\text{C.2})$$

We can use the phase invariance mentioned earlier to fix the value of ξ to any number in order to simplify the calculation; in our analysis, we use $\xi = \pi$. With this choice of ξ we explicitly break the symmetry between the contribution of real and imaginary parts of the WCs to various observables and exhaust the freedom in rephasing the WCs.

Next, we perform the following transformation (which is a combination of rotations, shifts and rescalings) on the WCs:

$$\begin{pmatrix} C_{+L}^S \\ C_{+L}^V \\ C_{-L}^V \\ C_{LL}^T \end{pmatrix} = \begin{pmatrix} 1.8108 & 3.7863 & -2.1150 & 0 \\ 0 & -5.1839 & 2.8958 & 0 \\ 0 & 13.3846 & -0.4787 & -1 \\ 0 & 4.2232 & -0.1510 & 0 \end{pmatrix} \begin{pmatrix} \tilde{C}_{+L}^S \\ \tilde{C}_{+L}^V \\ \tilde{C}_{-L}^V + 0.0114\mathcal{R}_{B_c} \\ \tilde{C}_{LL}^T \end{pmatrix}, \quad (\text{C.3})$$

in order to simultaneously diagonalize the quadratic terms in R_D and R_{D^*} :

$$\begin{aligned} R_D &= (\tilde{C}_{+L}^S)^2 + \tilde{x}_3^T M_D \tilde{x}_3 \\ R_{D^*} &= \tilde{x}_3^T \tilde{M}_{D^*} \tilde{x}_3 + v_{D^*}^T \tilde{x}_3 + A_{D^*} \end{aligned} \quad (\text{C.4})$$

Here $\tilde{x}_3 \equiv (\tilde{C}_{+L}^V, \tilde{C}_{-L}^V, \tilde{C}_{LL}^T)^T$ and

$$\tilde{M}_D = \begin{pmatrix} 1 & 0 & 0 \\ 0 & 1 & 0 \\ 0 & 0 & 0 \end{pmatrix}, \quad \tilde{M}_{D^*} = \begin{pmatrix} 26.7838 & 0 & 0 \\ 0 & 0.0553 & 0 \\ 0 & 0 & 0.2388 \end{pmatrix}, \quad (\text{C.5})$$

$$v_{D^*} = \begin{pmatrix} -0.0727\mathcal{R}_{B_c} \\ 0.0026\mathcal{R}_{B_c} \\ 0 \end{pmatrix}, \quad A_{D^*} = 0.0005\mathcal{R}_{B_c}^2. \quad (\text{C.6})$$

Under this transformation, the observables become:

$$\begin{aligned} R_{D^*} F_{D^*}^L &= \tilde{x}_3^T \tilde{M}_F \tilde{x}_3 + v_F^T \tilde{x}_3 + A_F \\ R_{J/\psi} &= \tilde{x}_3^T \tilde{M}_{J/\psi} \tilde{x}_3 + v_{J/\psi}^T \tilde{x}_3 + A_{J/\psi} \end{aligned} \quad (\text{C.7})$$

where

$$\begin{aligned} \tilde{M}_F &= \begin{pmatrix} 5.6079 & -0.2005 & -0.4042 \\ -0.2005 & 0.0072 & 0.0145 \\ -0.4042 & 0.0145 & 0.1105 \end{pmatrix}, \quad v_F = \begin{pmatrix} -0.0639\mathcal{R}_{B_c} \\ 0.0023\mathcal{R}_{B_c} \\ 0.0029\mathcal{R}_{B_c} \end{pmatrix}, \\ \tilde{M}_{J/\psi} &= \begin{pmatrix} 18.8505 & -0.3420 & -0.5463 \\ -0.3420 & 0.0368 & 0.0195 \\ -0.5463 & 0.0195 & 0.2756 \end{pmatrix}, \quad v_{J/\psi} = \begin{pmatrix} -0.0945\mathcal{R}_{B_c} \\ 0.0034\mathcal{R}_{B_c} \\ 0.0017\mathcal{R}_{B_c} \end{pmatrix}, \\ A_F &= 0.0004\mathcal{R}_{B_c}^2, \quad A_{J/\psi} = 0.0007\mathcal{R}_{B_c}^2. \end{aligned} \quad (\text{C.8})$$

We can go to spherical coordinates in $(\tilde{C}_{+L}^S, \tilde{C}_{+L}^V, \tilde{C}_{-L}^V)$ and solve the R_D constraint for the radial coordinate. Then we can solve the R_{D^*} constraint for \tilde{C}_{LL}^T which only appears as $(\tilde{C}_{LL}^T)^2$. This leaves behind two angles which we can then easily numerically maximize over and verify explicitly with a plot.

Appendix D

Analytic Expressions for the Observables

In order to get an expression for the polarization asymmetries, we write the total decay rate with the spin of the final state τ lepton in the arbitrary direction \hat{s} as [30]

$$d\Gamma^{(*)}(\hat{s}) = \frac{1}{2} \left(d\Gamma_{\text{tot}}^{(*)} + \left(d\Gamma_{\tau}^{(*)} \hat{e}_{\tau} + d\Gamma_{\perp}^{(*)} \hat{e}_{\perp} + d\Gamma_T^{(*)} \hat{e}_T \right) \cdot \hat{s} \right), \quad (\text{D.1})$$

where we have suppressed all other final state indices, e.g. D^* polarization, and

$$\begin{aligned} d\Gamma_{\text{tot}}^{(*)} &= \frac{1}{2m_B} (|\mathcal{M}_+|^2 + |\mathcal{M}_-|^2) d\Phi, \\ d\Gamma_{\tau}^{(*)} &= \frac{1}{2m_B} (|\mathcal{M}_+|^2 - |\mathcal{M}_-|^2) d\Phi, \\ d\Gamma_{\perp}^{(*)} &= \frac{1}{2m_B} 2\mathcal{R}e \left(\mathcal{M}_+^{\dagger} \mathcal{M}_- \right) d\Phi, \\ d\Gamma_T^{(*)} &= \frac{1}{2m_B} 2\mathcal{I}m \left(\mathcal{M}_+^{\dagger} \mathcal{M}_- \right) d\Phi, \end{aligned} \quad (\text{D.2})$$

where \mathcal{M}_{\pm} are the corresponding matrix elements with $\pm \tau$ helicity. The phase space element $d\Phi$ is given by

$$d\Phi = \frac{\sqrt{((m_B + m_M)^2 - q^2)((m_B - m_M)^2 - q^2)}}{256\pi^3 m_B^2} \left(1 - \frac{m_{\tau}^2}{q^2} \right)^2 dq^2 d\cos\theta, \quad (\text{D.3})$$

with m_M being the final meson ($D^{(*)}$) mass, q^2 being the four-momentum transferred to the leptonic side, and θ being the angle between the τ momentum and the final meson M in the q^2 frame. Using (D.2) in (4.16) we find an expression for the integrated asymmetries in every direction

$$\mathcal{P}_x^{(*)} = \frac{1}{\Gamma_{\text{tot}}^{(*)}} \int d\Gamma_x^{(*)}, \quad (\text{D.4})$$

where $x = \tau, \perp, T$. Similarly, the forward-backward symmetry defined in (4.14) can be written as

$$\mathcal{A}_{FB}^{(*)} = \frac{1}{\Gamma_{\text{tot}}^{(*)}} \int_{q^2} \left(- \int_{\cos(\theta)=0}^{\cos(\theta)=1} + \int_{\cos(\theta)=-1}^{\cos(\theta)=0} \right) d\Gamma_{\text{tot}}^{(*)} \quad (\text{D.5})$$

In this appendix we use (D.4) for the polarization asymmetries, as well as (D.5) for the forward-backward asymmetry $\mathcal{A}_{FB}^{(*)}$, to find analytic formulas for different decay rates used in Sec. 4.2. As indicated in the previous appendix, we use the convention and the notation in [68] for the hadronic functions.

We start with $\Gamma_{\text{tot}}^{(*)}$ and $\Gamma_{\tau}^{(*)}$. For the LH neutrinos contribution to the $\bar{B} \rightarrow D\tau\nu$ we have

$$\begin{aligned} \frac{d\Gamma_{\text{tot}}}{dq^2} = & \frac{G_F^2 V_{cb}^2}{192 m_B^3 \pi^3 q^2} \sqrt{((m_B - m_D)^2 - q^2)((m_B + m_D)^2 - q^2)} (m_\tau^2 - q^2)^2 \\ & \left\{ |C_{LL}^V + C_{RL}^V|^2 \left[(H_{V,0}^s)^2 \left(\frac{m_\tau^2}{2q^2} + 1 \right) + \frac{3m_\tau^2}{2q^2} (H_{V,t}^s)^2 \right] \right. \\ & + \frac{3}{2} (H_S^s)^2 |C_{RL}^S + C_{LL}^S|^2 + 8 |C_{LL}^T|^2 (H_T^s)^2 \left(1 + \frac{2m_\tau^2}{q^2} \right) \\ & + 3\mathcal{R}e \left[(C_{LL}^V + C_{RL}^V)(C_{RL}^S + C_{LL}^S)^* \right] \frac{m_\tau}{\sqrt{q^2}} H_S^s H_{V,t}^s \\ & \left. - 12\mathcal{R}e \left[(C_{LL}^V + C_{RL}^V)(C_{LL}^T)^* \right] \frac{m_\tau}{\sqrt{q^2}} H_T^s H_{V,0}^s \right\}, \end{aligned} \quad (\text{D.6})$$

$$\begin{aligned} \frac{d\Gamma_{\tau}}{dq^2} = & \frac{G_F^2 V_{cb}^2}{192 m_B^3 \pi^3 q^2} \sqrt{((m_B - m_D)^2 - q^2)((m_B + m_D)^2 - q^2)} (m_\tau^2 - q^2)^2 \\ & \left\{ |C_{LL}^V + C_{RL}^V|^2 \left[(H_{V,0}^s)^2 \left(\frac{m_\tau^2}{2q^2} - 1 \right) + \frac{3m_\tau^2}{2q^2} (H_{V,t}^s)^2 \right] \right. \\ & + \frac{3}{2} (H_S^s)^2 |C_{RL}^S + C_{LL}^S|^2 + 8 |C_{LL}^T|^2 (H_T^s)^2 \left(1 - \frac{2m_\tau^2}{q^2} \right) \\ & + 3\mathcal{R}e \left[(C_{LL}^V + C_{RL}^V)(C_{RL}^S + C_{LL}^S)^* \right] \frac{m_\tau}{\sqrt{q^2}} H_S^s H_{V,t}^s \\ & \left. + 4\mathcal{R}e \left[(C_{LL}^V + C_{RL}^V)(C_{LL}^T)^* \right] \frac{m_\tau}{\sqrt{q^2}} H_T^s H_{V,0}^s \right\}. \end{aligned}$$

Similarly, the contribution of the RH neutrinos to these rates are

$$\begin{aligned}
\frac{d\Gamma_{\text{tot}}}{dq^2} = & \frac{G_F^2 V_{cb}^2}{192 m_B^3 \pi^3 q^2} \sqrt{((m_B - m_D)^2 - q^2)((m_B + m_D)^2 - q^2)} (m_\tau^2 - q^2)^2 \\
& \left\{ |C_{LR}^V + C_{RR}^V|^2 \left((H_{V,0}^s)^2 \left(\frac{m_\tau^2}{2q^2} + 1 \right) + \frac{3m_\tau^2}{2q^2} (H_{V,t}^s)^2 \right) \right. \\
& + \frac{3}{2} |C_{RR}^S + C_{LR}^S|^2 (H_S^s)^2 + 8 |C_{RR}^T|^2 (H_T^s)^2 \left(1 + \frac{2m_\tau^2}{q^2} \right) \\
& + 3 \mathcal{R}e \left[(C_{RR}^S + C_{LR}^S) (C_{LR}^V + C_{RR}^V)^* \right] \frac{m_\tau}{\sqrt{q^2}} H_S^s H_{V,t}^s \\
& \left. - 12 \mathcal{R}e \left[(C_{RR}^V + C_{LR}^V) (C_{RR}^T)^* \right] \frac{m_\tau}{\sqrt{q^2}} H_T^s H_{V,0}^s \right\} \quad (\text{D.7})
\end{aligned}$$

$$\begin{aligned}
\frac{d\Gamma_\tau}{dq^2} = & \frac{G_F^2 V_{cb}^2}{192 m_B^3 \pi^3 q^2} \sqrt{((m_B - m_D)^2 - q^2)((m_B + m_D)^2 - q^2)} (m_\tau^2 - q^2)^2 \\
& \left\{ |C_{LR}^V + C_{RR}^V|^2 \left((H_{V,0}^s)^2 \left(-\frac{m_\tau^2}{2q^2} + 1 \right) - \frac{3m_\tau^2}{2q^2} (H_{V,t}^s)^2 \right) \right. \\
& - \frac{3}{2} |C_{RR}^S + C_{LR}^S|^2 (H_S^s)^2 + 8 |C_{RR}^T|^2 (H_T^s)^2 \left(-1 + \frac{2m_\tau^2}{q^2} \right) \\
& - 3 \mathcal{R}e \left[(C_{RR}^S + C_{LR}^S) (C_{LR}^V + C_{RR}^V)^* \right] \frac{m_\tau}{\sqrt{q^2}} H_S^s H_{V,t}^s \\
& \left. - 4 \mathcal{R}e \left[(C_{RR}^V + C_{LR}^V) (C_{RR}^T)^* \right] \frac{m_\tau}{\sqrt{q^2}} H_T^s H_{V,0}^s \right\}.
\end{aligned}$$

The dependence of all the hadronic functions H on q^2 is implicit. These equations can be used to calculate the contribution of each type of neutrinos to R_D and \mathcal{P}_τ .

For the LH neutrinos contribution to $\bar{B} \rightarrow D^* \tau \nu$ we have

$$\begin{aligned}
\frac{d\Gamma_{\text{tot}}^*}{dq^2} = & \frac{G_F^2 V_{cb}^2}{192 m_B^3 \pi^3 q^2} \sqrt{((m_B - m_{D^*})^2 - q^2)((m_B + m_{D^*})^2 - q^2)} (m_\tau^2 - q^2)^2 \\
& \left\{ (|C_{LL}^V|^2 + |C_{RL}^V|^2) \left[(H_{V,+}^2 + H_{V,-}^2 + H_{V,0}^2) \left(\frac{m_\tau^2}{2q^2} + 1 \right) + \frac{3m_\tau^2}{2q^2} H_{V,t}^2 \right] \right. \\
& - 2\mathcal{R}e [(C_{LL}^V)(C_{RL}^V)^*] \left[(2H_{V,+}H_{V,-} + H_{V,0}^2) \left(\frac{m_\tau^2}{2q^2} + 1 \right) + \frac{3m_\tau^2}{2q^2} H_{V,t}^2 \right] \\
& + \frac{3}{2} (H_S)^2 |C_{RL}^S - C_{LL}^S|^2 + 8|C_{LL}^T|^2 \left(1 + \frac{2m_\tau^2}{q^2} \right) (H_{T,+}^2 + H_{T,-}^2 + H_{T,0}^2) \\
& + 3\mathcal{R}e [(C_{LL}^V - C_{RL}^V)(C_{RL}^S - C_{LL}^S)^*] \frac{m_\tau}{\sqrt{q^2}} H_S H_{V,t} \\
& - 12\mathcal{R}e [(C_{LL}^V)(C_{LL}^T)^*] \frac{m_\tau}{\sqrt{q^2}} (H_{T,0}H_{V,0} + H_{T,+}H_{V,+} - H_{T,-}H_{V,-}) \\
& \left. + 12\mathcal{R}e [C_{RL}^V(C_{LL}^T)^*] \frac{m_\tau}{\sqrt{q^2}} (H_{T,0}H_{V,0} + H_{T,+}H_{V,-} - H_{T,-}H_{V,+}) \right\}, \tag{D.8}
\end{aligned}$$

$$\begin{aligned}
\frac{d\Gamma_\tau^*}{dq^2} = & \frac{G_F^2 V_{cb}^2}{192 m_B^3 \pi^3 q^2} \sqrt{((m_B - m_{D^*})^2 - q^2)((m_B + m_{D^*})^2 - q^2)} (m_\tau^2 - q^2)^2 \\
& \left\{ (|C_{LL}^V|^2 + |C_{RL}^V|^2) \left[(H_{V,+}^2 + H_{V,-}^2 + H_{V,0}^2) \left(\frac{m_\tau^2}{2q^2} - 1 \right) + \frac{3m_\tau^2}{2q^2} H_{V,t}^2 \right] \right. \\
& - 2\mathcal{R}e [(C_{LL}^V)(C_{RL}^V)^*] \left[(2H_{V,+}H_{V,-} + H_{V,0}^2) \left(\frac{m_\tau^2}{2q^2} - 1 \right) + \frac{3m_\tau^2}{2q^2} H_{V,t}^2 \right] \\
& + \frac{3}{2} (H_S)^2 |C_{RL}^S - C_{LL}^S|^2 + 8|C_{LL}^T|^2 \left(1 - \frac{2m_\tau^2}{q^2} \right) (H_{T,+}^2 + H_{T,-}^2 + H_{T,0}^2) \\
& + 3\mathcal{R}e [(C_{LL}^V - C_{RL}^V)(C_{RL}^S - C_{LL}^S)^*] \frac{m_\tau}{\sqrt{q^2}} H_S H_{V,t} \\
& + 4\mathcal{R}e [(C_{LL}^V)(C_{LL}^T)^*] \frac{m_\tau}{\sqrt{q^2}} (H_{T,0}H_{V,0} + H_{T,+}H_{V,+} - H_{T,-}H_{V,-}) \\
& \left. - 4\mathcal{R}e [C_{RL}^V(C_{LL}^T)^*] \frac{m_\tau}{\sqrt{q^2}} (H_{T,0}H_{V,0} + H_{T,+}H_{V,-} - H_{T,-}H_{V,+}) \right\}.
\end{aligned}$$

The corresponding decay rates with RH neutrinos instead are

$$\begin{aligned}
\frac{d\Gamma_{\text{tot}}^*}{dq^2} = & \frac{G_F^2 V_{cb}^2}{192 m_B^3 \pi^3 q^2} \sqrt{((m_B - m_{D^*})^2 - q^2)((m_B + m_{D^*})^2 - q^2)} (m_\tau^2 - q^2)^2 \\
& \left\{ (|C_{LR}^V|^2 + |C_{RR}^V|^2) \left(\frac{m_\tau^2}{2q^2} + 1 \right) ((H_{V,-})^2 + (H_{V,+})^2) \right. \\
& + |C_{LR}^V - C_{RR}^V|^2 \left((H_{V,0})^2 \left(\frac{m_\tau^2}{2q^2} + 1 \right) + (H_{V,t})^2 \frac{3m_\tau^2}{2q^2} \right) \\
& - 4\mathcal{R}e [C_{LR}^V (C_{RR}^V)^*] \left(\frac{m_\tau^2}{2q^2} + 1 \right) H_{V,+} H_{V,-} + \frac{3}{2} |C_{RR}^S - C_{LR}^S|^2 (H_S)^2 \\
& + 3\mathcal{R}e [(C_{RR}^V - C_{LR}^V) (C_{LR}^S - C_{RR}^S)^*] \frac{m_\tau}{\sqrt{q^2}} H_S H_{V,t} \\
& + 8|C_{RR}^T|^2 \left(1 + \frac{2m_\tau^2}{q^2} \right) ((H_{T2,-})^2 + (H_{T,0})^2 + (H_{T2,+})^2) \\
& - 12\mathcal{R}e [C_{LR}^V (C_{RR}^T)^*] \frac{m_\tau}{\sqrt{q^2}} (H_{T2,-} H_{V,-} - H_{T,0} H_{V,0} - H_{T2,+} H_{V,+}) \\
& \left. + 12\mathcal{R}e [C_{RR}^V (C_{RR}^T)^*] \frac{m_\tau}{\sqrt{q^2}} (H_{T2,-} H_{V,+} - H_{T,0} H_{V,0} - H_{T2,+} H_{V,-}) \right\} \quad (\text{D.9})
\end{aligned}$$

$$\begin{aligned}
\frac{d\Gamma_\tau^*}{dq^2} = & \frac{G_F^2 V_{cb}^2}{192 m_B^3 \pi^3 q^2} \sqrt{((m_B - m_{D^*})^2 - q^2)((m_B + m_{D^*})^2 - q^2)} (m_\tau^2 - q^2)^2 \\
& \left\{ (|C_{LR}^V|^2 + |C_{RR}^V|^2) \left(-\frac{m_\tau^2}{2q^2} + 1 \right) ((H_{V,-})^2 + (H_{V,+})^2) \right. \\
& + |C_{LR}^V - C_{RR}^V|^2 \left((H_{V,0})^2 \left(-\frac{m_\tau^2}{2q^2} + 1 \right) - (H_{V,t})^2 \frac{3m_\tau^2}{2q^2} \right) \\
& - 4\mathcal{R}e [C_{LR}^V (C_{RR}^V)^*] \left(-\frac{m_\tau^2}{2q^2} + 1 \right) H_{V,+} H_{V,-} - \frac{3}{2} |C_{RR}^S - C_{LR}^S|^2 (H_S)^2 \\
& - 3\mathcal{R}e [(C_{RR}^V - C_{LR}^V) (C_{LR}^S - C_{RR}^S)^*] \frac{m_\tau}{\sqrt{q^2}} H_S H_{V,t} \\
& + 8|C_{RR}^T|^2 \left(-1 + \frac{2m_\tau^2}{q^2} \right) ((H_{T2,-})^2 + (H_{T,0})^2 + (H_{T2,+})^2) \\
& - 4\mathcal{R}e [C_{LR}^V (C_{RR}^T)^*] \frac{m_\tau}{\sqrt{q^2}} (H_{T2,-} H_{V,-} - H_{T,0} H_{V,0} - H_{T2,+} H_{V,+}) \\
& \left. + 4\mathcal{R}e [C_{RR}^V (C_{RR}^T)^*] \frac{m_\tau}{\sqrt{q^2}} (H_{T2,-} H_{V,+} - H_{T,0} H_{V,0} - H_{T2,+} H_{V,-}) \right\}.
\end{aligned}$$

We can use (D.8)–(D.9) to find the contribution of each type of neutrinos to R_{D^*} and

\mathcal{P}_τ^* .

The symmetry outlined in (4.12)–(4.13) between RH and LH neutrino contribution is manifested in the decay rates (D.6)–(D.9). In other words, the unpolarized decay rates have the same q^2 dependence for either types of neutrinos. The only difference between the two cases is the irreducible SM contribution. Even considering this difference, there are scenarios with different types of neutrinos that have indistinguishable q^2 distributions. An example of this is illustrated in Fig. D.1 for U_1 LQ models interacting with different types of neutrinos. In this figure we normalize the differential rate to the SM total rate, so that the area under each plot is proportional to its $R_{D^{(*)}}$ prediction. Each curve results in an $R_{D^{(*)}}$ close to the current global averages (see the 10σ scenario in Sec. 4.1.4). These plots show that in this scenario there are benchmark points that, unlike the asymmetry observables we studied, the q^2 distribution of the decay rates will not be able to distinguish models with different types of neutrinos.

For Γ_\perp and Γ_T we have

$$\frac{d\Gamma_\perp}{dq^2} = \frac{G_F^2 V_{cb}^2}{192 m_B^3 \pi^3 q^2} \sqrt{((m_B - m_D)^2 - q^2)((m_B + m_D)^2 - q^2)} (m_\tau^2 - q^2)^2 \mathcal{R}e(\Sigma), \quad (\text{D.10})$$

$$\frac{d\Gamma_T}{dq^2} = \frac{G_F^2 V_{cb}^2}{192 m_B^3 \pi^3 q^2} \sqrt{((m_B - m_D)^2 - q^2)((m_B + m_D)^2 - q^2)} (m_\tau^2 - q^2)^2 \mathcal{I}m(\Sigma),$$

where

$$\begin{aligned} \Sigma = & \frac{3\pi}{4q^2} \left[\left(\sqrt{q^2} (C_{RR}^S + C_{LR}^S) H_S^s + m_\tau (C_{LR}^V + C_{RR}^V) H_{V,t}^s \right) \times \right. \\ & \left((C_{LR}^V + C_{RR}^V)^* \sqrt{q^2} H_{V,0}^s - 4m_\tau (C_{RR}^T)^* H_T^s \right) - \\ & \left((C_{RL}^S + C_{LL}^S)^* \sqrt{q^2} H_S^s + m_\tau (C_{LL}^V + C_{RL}^V)^* H_{V,t}^s \right) \times \\ & \left. \left((1 + C_{LL}^V + C_{RL}^V) \sqrt{q^2} H_{V,0}^s - 4m_\tau (C_{LL}^T) H_T^s \right) \right] \end{aligned} \quad (\text{D.11})$$

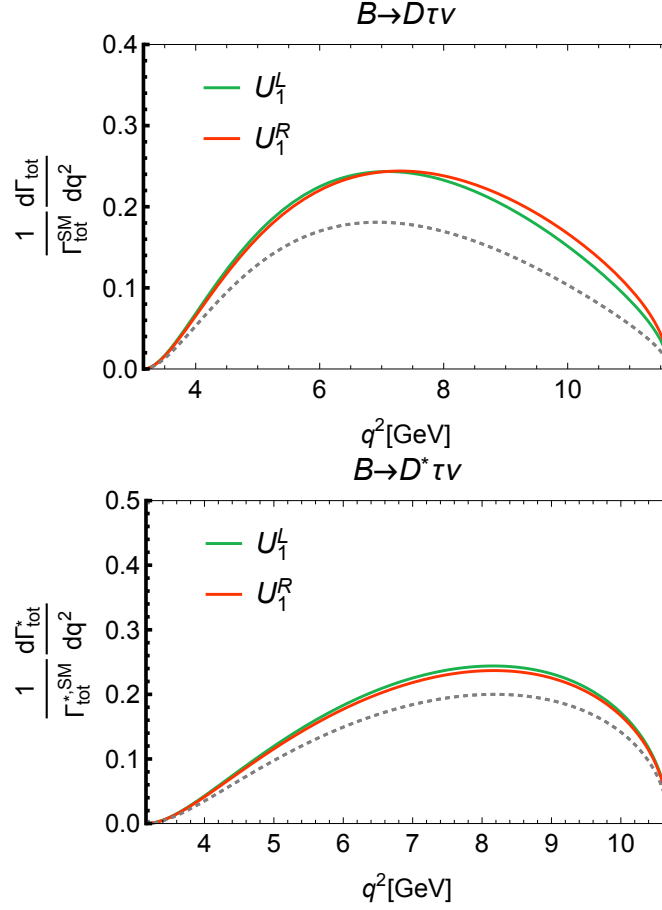


Figure D.1: The q^2 distribution for benchmark WCs for models interacting with LH neutrinos (green curves) and those interacting with RH neutrinos (red curves). The decay rate for $\bar{B} \rightarrow D\tau\nu$ ($\bar{B} \rightarrow D^*\tau\nu$) is shown on top (bottom). We show the viable LQ models whose effective operators from Tab. 4.1 are related through the symmetry in (4.12)–(4.13). The dashed gray line is the SM prediction. The area under each curve is proportional to its prediction for $R_{D^{(*)}}$. Up to a rescaling factor the plots for different types of neutrinos have indistinguishable shapes.

Equivalently, we can write the polarization asymmetries in $\bar{B} \rightarrow D^* \tau \nu$ as

$$\frac{d\Gamma_{\perp}^*}{dq^2} = \frac{G_F^2 V_{cb}^2}{192 m_B^3 \pi^3 q^2} \sqrt{((m_B - m_{D^*})^2 - q^2)((m_B + m_{D^*})^2 - q^2)} (m_\tau^2 - q^2)^2 \mathcal{R}e(\Sigma^*), \quad (\text{D.12})$$

$$\frac{d\Gamma_T^*}{dq^2} = \frac{G_F^2 V_{cb}^2}{192 m_B^3 \pi^3 q^2} \sqrt{((m_B - m_{D^*})^2 - q^2)((m_B + m_{D^*})^2 - q^2)} (m_\tau^2 - q^2)^2 \mathcal{I}m(\Sigma^*),$$

where Σ^* is given by

$$\begin{aligned} \Sigma^* = & \frac{3\pi}{8q^2} \left[- \left((C_{LL}^V) \sqrt{q^2} H_{V,-} - \sqrt{q^2} C_{RL}^V H_{V,+} + 4C_{LL}^T m_\tau H_{T,-} \right) \times \right. \\ & \left(m_\tau (C_{LL}^V)^* H_{V,-} - m_\tau (C_{RL}^V)^* H_{V,+} + 4\sqrt{q^2} (C_{LL}^T)^* H_{T,-} \right) \\ & + \left(2\sqrt{q^2} (C_{LL}^S - C_{RL}^S)^* H_S + 2m_\tau (-1 - C_{LL}^V + C_{RL}^V)^* H_{V,t} \right) \times \\ & \left((C_{LL}^V - C_{RL}^V) \sqrt{q^2} H_{V,0} - 4C_{LL}^T m_\tau H_{T,0} \right) \\ & + \left(\sqrt{q^2} C_{RL}^V H_{V,-} - \sqrt{q^2} (C_{LL}^V) H_{V,+} + 4m_\tau C_{LL}^T H_{T,+} \right) \times \\ & \left(m_\tau (C_{RL}^V)^* H_{V,-} - m_\tau (C_{LL}^V)^* H_{V,+} + 4\sqrt{q^2} (C_{LL}^T)^* H_{T,+} \right) \\ & - \left((C_{RR}^V)^* \sqrt{q^2} H_{V,+}^+ - \sqrt{q^2} (C_{LR}^V)^* H_{V,-}^- + 4(C_{RR}^T)^* m_\tau H_{T2,-} \right) \times \\ & \left(m_\tau C_{RR}^V H_{V,+} - m_\tau C_{LR}^V H_{V,-} + 4\sqrt{q^2} C_{RR}^T H_{T2,-} \right) \\ & + \left(2\sqrt{q^2} (C_{RR}^S - C_{LR}^S) H_S + 2m_\tau (-C_{RR}^V + C_{LR}^V) H_{V,t} \right) \times \\ & \left((C_{LR}^V - C_{RR}^V)^* \sqrt{q^2} H_{V,0} + 4(C_{RR}^T)^* m_\tau H_{T,0} \right) \\ & + \left(\sqrt{q^2} (C_{LR}^V)^* H_{V,+} - \sqrt{q^2} (C_{RR}^V)^* H_{V,-} + 4m_\tau (C_{RR}^T)^* H_{T2,+} \right) \times \\ & \left. \left(m_\tau C_{LR}^V H_{V,+} - m_\tau C_{RR}^V H_{V,-} + 4\sqrt{q^2} C_{RR}^T H_{T2,+} \right) \right] \end{aligned} \quad (\text{D.13})$$

Let us now move on to the forward-backward asymmetries $\mathcal{A}_{FB}^{(*)}$. Here we report the analytic results for a finer observable, namely the forward-backward asymmetry of τ with a specific helicity. For the $\bar{B} \rightarrow D \tau \nu$ decay involving the LH neutrinos we

have

$$\begin{aligned} \frac{d\mathcal{A}_{FB}^+}{dq^2} = & -\frac{G_F^2 V_{cb}^2}{192m_B^3 \pi^3 q^2 \Gamma_{B \rightarrow D\tau\nu}} \sqrt{((m_B - m_D)^2 - q^2)((m_B + m_D)^2 - q^2)} \\ & (m_\tau^2 - q^2)^2 \frac{3}{2q^2} \mathcal{Re} \left[\left(\sqrt{q^2} (C_{RL}^S + C_{LL}^S) H_S^s + m_\tau (C_{LL}^V + C_{RL}^V) H_{V,t}^s \right) \right. \\ & \left. \left(m_\tau (C_{LL}^V + C_{RL}^V) H_{V,0}^s - 4C_{LL}^T \sqrt{q^2} H_T^s \right)^* \right], \end{aligned} \quad (\text{D.14})$$

$$\frac{d\mathcal{A}_{FB}^-}{dq^2} = 0.$$

Here the superscripts \pm refer to specific τ helicities. Similarly, for the right-handed neutrinos contribution we have

$$\frac{d\mathcal{A}_{FB}^+}{dq^2} = 0 \quad (\text{D.15})$$

$$\begin{aligned} \frac{d\mathcal{A}_{FB}^-}{dq^2} = & -\frac{G_F^2 V_{cb}^2}{192m_B^3 \pi^3 q^2 \Gamma_{B \rightarrow D\tau\nu}} \sqrt{((m_B - m_D)^2 - q^2)((m_B + m_D)^2 - q^2)} \\ & (m_\tau^2 - q^2)^2 \frac{3}{2q^2} \mathcal{Re} \left[\left(\sqrt{q^2} (C_{RR}^S + C_{LR}^S) H_S^s + m_\tau (C_{LR}^V + C_{RR}^V) H_{V,s}^s \right) \right. \\ & \left. \left(m_\tau (C_{LR}^V + C_{RR}^V) H_{V,0}^s - 4C_{RR}^T \sqrt{q^2} H_T^s \right)^* \right]. \end{aligned}$$

Equivalently, for the decays into D^* we have

$$\begin{aligned} \frac{d\mathcal{A}_{FB}^{+*}}{dq^2} = & -\frac{G_F^2 V_{cb}^2}{192m_B^3 \pi^3 q^2 \Gamma_{B \rightarrow D^*\tau\nu}} \sqrt{((m_B - m_{D^*})^2 - q^2)((m_B + m_{D^*})^2 - q^2)} \\ & (m_\tau^2 - q^2)^2 \frac{3}{2q^2} \mathcal{Re} \left[\left(\sqrt{q^2} (C_{RL}^S - C_{LL}^S) H_S + m_\tau (C_{LL}^V - C_{RL}^V) H_{V,t} \right) \right. \\ & \left. \left(m_\tau (C_{LL}^V - C_{RL}^V) H_{V,0} - 4C_{LL}^T \sqrt{q^2} H_{T,0} \right)^* \right], \end{aligned} \quad (\text{D.16})$$

$$\begin{aligned} \frac{d\mathcal{A}_{FB}^{-*}}{dq^2} = & \frac{G_F^2 V_{cb}^2}{192m_B^3 \pi^3 q^2 \Gamma_{B \rightarrow D^*\tau\nu}} \times \\ & \sqrt{((m_B - m_{D^*})^2 - q^2)((m_B + m_{D^*})^2 - q^2)} (m_\tau^2 - q^2)^2 \left(\frac{3}{4q^2} \right) \\ & \mathcal{Re} \left[\left(\sqrt{q^2} (C_{LL}^V - C_{RL}^V) (H_{V,-} + H_{V,+}) + 4m_\tau C_{LL}^T (H_{T,-} - H_{T,+}) \right) \right. \\ & \left. \left(\sqrt{q^2} (C_{LL}^V + C_{RL}^V) (H_{V,-} - H_{V,+}) + 4m_\tau C_{LL}^T (H_{T,-} + H_{T,+}) \right)^* \right], \end{aligned}$$

for the LH neutrinos contribution. For the RH neutrino contribution we have

$$\begin{aligned} \frac{d\mathcal{A}_{FB}^{+*}}{dq^2} = & -\frac{G_F^2 V_{cb}^2}{192m_B^3\pi^3q^2\Gamma_{B\rightarrow D^*\tau\nu}} \times \\ & \sqrt{((m_B - m_{D^*})^2 - q^2)((m_B + m_{D^*})^2 - q^2)}(m_\tau^2 - q^2)^2 \frac{3}{4q^2} \\ & \mathcal{Re} \left[\left(\sqrt{q^2}(C_{LR}^V - C_{RR}^V)(H_{V,-} + H_{V,+}) + 4m_\tau C_{RR}^T(-H_{T2,-} + H_{T2,+}) \right) \right. \\ & \left. \left(\sqrt{q^2}(C_{LR}^V + C_{RR}^V)(H_{V,-} - H_{V,+}) - 4m_\tau C_{RR}^T(H_{T2,-} + H_{T2,+}) \right)^* \right], \end{aligned} \quad (\text{D.17})$$

$$\begin{aligned} \frac{d\mathcal{A}_{FB}^{-*}}{dq^2} = & -\frac{G_F^2 V_{cb}^2}{192m_B^3\pi^3q^2\Gamma_{B\rightarrow D^*\tau\nu}} \times \\ & \sqrt{((m_B - m_{D^*})^2 - q^2)((m_B + m_{D^*})^2 - q^2)}(m_\tau^2 - q^2)^2 \\ & \frac{3}{2q^2} \mathcal{Re} \left[\left(\sqrt{q^2}(C_{RR}^S - C_{LR}^S)H_S + m_\tau(C_{LR}^V - C_{RR}^V)H_{V,t} \right) \right. \\ & \left. \left(m_\tau(C_{LR}^V - C_{RR}^V)H_{V,0} + 4C_{RR}^T\sqrt{q^2}H_{T,0} \right)^* \right]. \end{aligned}$$

We note that $\mathcal{A}_{FB}^{\pm, (*)}$ contain more information than the $\mathcal{A}_{FB}^{(*)}$ observables we studied in this work. The experimental proposal in [41] for measuring the forward-backward asymmetry is applicable to the total asymmetry summed over final τ helicity. It is intriguing to find a similar proposal for measurement of $\mathcal{A}_{FB}^{\pm, (*)}$. In particular, (D.14) and (D.15) suggest that a non-zero \mathcal{A}_{FB}^- (\mathcal{A}_{FB}^+) is a clear signature of RH (LH) neutrinos.

The numerical formulas in Sec. 4.2 are obtained by using similar form factors as in [39], and integrating the analytic formulas in this appendix over q^2 . We use the same numerical parameter values as in [60], which we list here again in Tab. D.1 for completeness.

Bibliography

- [1] Y. Grossman and P. Tanedo, “Just a Taste: Lectures on Flavor Physics,” in *Proceedings, Theoretical Advanced Study Institute in Elementary Particle Physics : Anticipating the Next Discoveries in Particle Physics (TASI 2016)*:

V_{cb}	G_F [GeV ⁻²]	$m_{\bar{B}}$ [GeV]	m_D [GeV]
42.2×10^{-3}	1.166×10^{-5}	5.279	1.870
m_{D^*} [GeV]	m_e [GeV]	m_μ [GeV]	m_τ [GeV]
2.010	0.511×10^{-3}	0.106	1.777

Table D.1: The parameter values used in our calculation of the numerical formulas presented in Chap. 4.

Boulder, CO, USA, June 6-July 1, 2016, pp. 109–295. 2018.

arXiv:1711.03624 [hep-ph].

[2] E. Kou *et al.* arXiv:1808.10567 [hep-ex].

[3] **Particle Data Group** Collaboration, M. e. a. Tanabashi *Phys. Rev. D* **98** (Aug, 2018) 030001.

<https://link.aps.org/doi/10.1103/PhysRevD.98.030001>.

[4] **BaBar** Collaboration, B. Aubert *et al.* *Phys. Rev. Lett.* **100** (2008) 021801, arXiv:0709.1698 [hep-ex].

[5] **BaBar** Collaboration, J. P. Lees *et al.* *Phys. Rev. Lett.* **109** (2012) 101802, arXiv:1205.5442 [hep-ex].

[6] **BaBar** Collaboration, J. P. Lees *et al.* *Phys. Rev.* **D88** no. 7, (2013) 072012, arXiv:1303.0571 [hep-ex].

[7] **Belle** Collaboration, A. Bozek *et al.* *Phys. Rev.* **D82** (2010) 072005, arXiv:1005.2302 [hep-ex].

[8] **Belle** Collaboration, M. Huschle *et al.* *Phys. Rev.* **D92** no. 7, (2015) 072014, arXiv:1507.03233 [hep-ex].

[9] A. Abdesselam *et al.* arXiv:1608.06391 [hep-ex].

- [10] **LHCb** Collaboration, R. Aaij *et al.* *Phys. Rev. Lett.* **115** no. 11, (2015) 111803, [arXiv:1506.08614 \[hep-ex\]](#). [Erratum: *Phys. Rev. Lett.*115,no.15,159901(2015)].
- [11] **LHCb** Collaboration, R. Aaij *et al.* [arXiv:1711.05623 \[hep-ex\]](#).
- [12] **LHCb** Collaboration, R. Aaij *et al.* *JHEP* **08** (2017) 055, [arXiv:Aaij:2017tyk \[hep-ex\]](#).
- [13] **HFLAV** Collaboration, Y. Amhis *et al.* *Eur. Phys. J.* **C77** no. 12, (2017) 895, [arXiv:1612.07233 \[hep-ex\]](#).
- [14] S. Aoki *et al.* *Eur. Phys. J.* **C77** no. 2, (2017) 112, [arXiv:1607.00299 \[hep-lat\]](#).
- [15] **HPQCD** Collaboration, H. Na, C. M. Bouchard, G. P. Lepage, C. Monahan, and J. Shigemitsu *Phys. Rev.* **D92** no. 5, (2015) 054510, [arXiv:1505.03925 \[hep-lat\]](#). [Erratum: *Phys. Rev.*D93,no.11,119906(2016)].
- [16] S. Fajfer, J. F. Kamenik, and I. Nisandzic *Phys. Rev.* **D85** (2012) 094025, [arXiv:1203.2654 \[hep-ph\]](#).
- [17] **MILC** Collaboration, J. A. Bailey *et al.* *Phys. Rev.* **D92** no. 3, (2015) 034506, [arXiv:1503.07237 \[hep-lat\]](#).
- [18] J. A. Bailey *et al.* *Phys. Rev. Lett.* **109** (2012) 071802, [arXiv:1206.4992 \[hep-ph\]](#).
- [19] J. F. Kamenik and F. Mescia *Phys. Rev.* **D78** (2008) 014003, [arXiv:0802.3790 \[hep-ph\]](#).
- [20] S. Jaiswal, S. Nandi, and S. K. Patra *JHEP* **12** (2017) 060, [arXiv:1707.09977 \[hep-ph\]](#).

- [21] N. Isgur and M. B. Wise *Phys. Lett.* **B232** (1989) 113–117.
- [22] N. Isgur and M. B. Wise *Phys. Lett.* **B237** (1990) 527–530.
- [23] H. Georgi *Phys. Lett.* **B240** (1990) 447–450.
- [24] **LHCb Collaboration** Collaboration *Phys. Rev. Lett.* **120** (Apr, 2018) 171802. <https://link.aps.org/doi/10.1103/PhysRevLett.120.171802>.
- [25] R. Dutta and A. Bhol *Phys. Rev.* **D96** no. 7, (2017) 076001, [arXiv:1701.08598 \[hep-ph\]](#).
- [26] R. Watanabe *Phys. Lett.* **B776** (2018) 5–9, [arXiv:1709.08644 \[hep-ph\]](#).
- [27] C.-T. Tran, M. A. Ivanov, J. G. Krner, and P. Santorelli *Phys. Rev.* **D97** no. 5, (2018) 054014, [arXiv:1801.06927 \[hep-ph\]](#).
- [28] T. D. Cohen, H. Lamm, and R. F. Lebed *JHEP* **09** (2018) 168, [arXiv:1807.02730 \[hep-ph\]](#).
- [29] D. Leljak, B. Melic, and M. Patra [arXiv:1901.08368 \[hep-ph\]](#).
- [30] M. Tanaka *Z. Phys.* **C67** (1995) 321–326, [arXiv:hep-ph/9411405 \[hep-ph\]](#).
- [31] M. Tanaka and R. Watanabe *Phys. Rev.* **D82** (2010) 034027, [arXiv:1005.4306 \[hep-ph\]](#).
- [32] Y. Sakaki and H. Tanaka *Phys. Rev.* **D87** no. 5, (2013) 054002, [arXiv:1205.4908 \[hep-ph\]](#).
- [33] A. Datta, M. Duraisamy, and D. Ghosh *Phys. Rev.* **D86** (2012) 034027, [arXiv:1206.3760 \[hep-ph\]](#).
- [34] M. Duraisamy and A. Datta *JHEP* **09** (2013) 059, [arXiv:1302.7031 \[hep-ph\]](#).

- [35] M. A. Ivanov, J. G. Krner, and C. T. Tran *Phys. Rev.* **D92** no. 11, (2015) 114022, [arXiv:1508.02678 \[hep-ph\]](#).
- [36] D. Becirevic, S. Fajfer, I. Nisandzic, and A. Tayduganov [arXiv:1602.03030 \[hep-ph\]](#).
- [37] R. Alonso, A. Kobach, and J. Martin Camalich *Phys. Rev.* **D94** no. 9, (2016) 094021, [arXiv:1602.07671 \[hep-ph\]](#).
- [38] A. K. Alok, D. Kumar, S. Kumbhakar, and S. U. Sankar *Phys. Rev.* **D95** no. 11, (2017) 115038, [arXiv:1606.03164 \[hep-ph\]](#).
- [39] D. Bardhan, P. Byakti, and D. Ghosh *JHEP* **01** (2017) 125, [arXiv:1610.03038 \[hep-ph\]](#).
- [40] M. A. Ivanov, J. G. Krner, and C.-T. Tran *Phys. Rev.* **D95** no. 3, (2017) 036021, [arXiv:1701.02937 \[hep-ph\]](#).
- [41] R. Alonso, J. Martin Camalich, and S. Westhoff *Phys. Rev.* **D95** no. 9, (2017) 093006, [arXiv:1702.02773 \[hep-ph\]](#).
- [42] P. Asadi, M. R. Buckley, and D. Shih *Phys. Rev.* **D99** no. 3, (2019) 035015, [arXiv:1810.06597 \[hep-ph\]](#).
- [43] **Belle** Collaboration, A. Abdesselam *et al.*, “Measurement of the D^{*-} polarization in the decay $B^0 \rightarrow D^{*-}\tau^+\nu_\tau$,” in *10th International Workshop on the CKM Unitarity Triangle (CKM 2018) Heidelberg, Germany, September 17-21, 2018*. 2019. [arXiv:1903.03102 \[hep-ex\]](#).
- [44] S. Bhattacharya, S. Nandi, and S. Kumar Patra *Eur. Phys. J.* **C79** no. 3, (2019) 268, [arXiv:1805.08222 \[hep-ph\]](#).

- [45] Z.-R. Huang, Y. Li, C.-D. Lu, M. A. Paracha, and C. Wang *Phys. Rev. D* **98** (Nov, 2018) 095018.
<https://link.aps.org/doi/10.1103/PhysRevD.98.095018>.
- [46] S. Fajfer, J. F. Kamenik, I. Nisandzic, and J. Zupan *Phys. Rev. Lett.* **109** (2012) 161801, [arXiv:1206.1872 \[hep-ph\]](#).
- [47] A. Crivellin, C. Greub, and A. Kokulu *Phys. Rev.* **D86** (2012) 054014, [arXiv:1206.2634 \[hep-ph\]](#).
- [48] A. Celis, M. Jung, X.-Q. Li, and A. Pich *JHEP* **01** (2013) 054, [arXiv:1210.8443 \[hep-ph\]](#).
- [49] X.-Q. Li, Y.-D. Yang, and X. Zhang *JHEP* **08** (2016) 054, [arXiv:1605.09308 \[hep-ph\]](#).
- [50] A. Celis, M. Jung, X.-Q. Li, and A. Pich *Phys. Lett.* **B771** (2017) 168–179, [arXiv:1612.07757 \[hep-ph\]](#).
- [51] R. Alonso, B. Grinstein, and J. Martin Camalich *Phys. Rev. Lett.* **118** no. 8, (2017) 081802, [arXiv:1611.06676 \[hep-ph\]](#).
- [52] A. G. Akeroyd and C.-H. Chen *Phys. Rev.* **D96** no. 7, (2017) 075011, [arXiv:1708.04072 \[hep-ph\]](#).
- [53] X.-G. He and G. Valencia *Phys. Rev.* **D87** no. 1, (2013) 014014, [arXiv:1211.0348 \[hep-ph\]](#).
- [54] S. M. Boucenna, A. Celis, J. Fuentes-Martin, A. Vicente, and J. Virto *JHEP* **12** (2016) 059, [arXiv:1608.01349 \[hep-ph\]](#).
- [55] A. Greljo, G. Isidori, and D. Marzocca *JHEP* **07** (2015) 142, [arXiv:1506.01705 \[hep-ph\]](#).

- [56] D. A. Faroughy, A. Greljo, and J. F. Kamenik *Phys. Lett.* **B764** (2017) 126–134, [arXiv:1609.07138 \[hep-ph\]](#).
- [57] A. Crivellin, D. Mller, and T. Ota *JHEP* **09** (2017) 040, [arXiv:1703.09226 \[hep-ph\]](#).
- [58] M. Tanaka and R. Watanabe *Phys. Rev.* **D87** no. 3, (2013) 034028, [arXiv:1212.1878 \[hep-ph\]](#).
- [59] L. Calibbi, A. Crivellin, and T. Li [arXiv:1709.00692 \[hep-ph\]](#).
- [60] P. Asadi, M. R. Buckley, and D. Shih *JHEP* **09** (2018) 010, [arXiv:1804.04135 \[hep-ph\]](#).
- [61] P. Asadi and D. Shih [arXiv:1905.03311 \[hep-ph\]](#).
- [62] D. Beirevi, S. Fajfer, N. Konik, and O. Sumensari *Phys. Rev.* **D94** no. 11, (2016) 115021, [arXiv:1608.08501 \[hep-ph\]](#).
- [63] J. M. Cline *Phys. Rev.* **D93** no. 7, (2016) 075017, [arXiv:1512.02210 \[hep-ph\]](#).
- [64] S. Iguro and Y. Omura *JHEP* **05** (2018) 173, [arXiv:1802.01732 \[hep-ph\]](#).
- [65] R. Dutta, A. Bhol, and A. K. Giri *Phys. Rev.* **D88** no. 11, (2013) 114023, [arXiv:1307.6653 \[hep-ph\]](#).
- [66] R. Dutta and A. Bhol *Phys. Rev.* **D96** no. 3, (2017) 036012, [arXiv:1611.00231 \[hep-ph\]](#).
- [67] A. Donini, F. Feruglio, J. Matias, and F. Zwirner *Nucl. Phys.* **B507** (1997) 51–90, [arXiv:hep-ph/9705450 \[hep-ph\]](#).
- [68] Y. Sakaki, M. Tanaka, A. Tayduganov, and R. Watanabe *Phys. Rev.* **D88** no. 9, (2013) 094012, [arXiv:1309.0301 \[hep-ph\]](#).

- [69] **Particle Data Group** Collaboration, C. Patrignani *et al.* *Chin. Phys.* **C40** no. 10, (2016) 100001.
- [70] K. Hagiwara, A. D. Martin, and M. F. Wade *Nucl. Phys.* **B327** (1989) 569–594.
- [71] D. Melikhov and B. Stech *Phys. Rev.* **D62** (2000) 014006, [arXiv:hep-ph/0001113](#) [hep-ph].
- [72] I. Caprini, L. Lellouch, and M. Neubert *Nucl. Phys.* **B530** (1998) 153–181, [arXiv:hep-ph/9712417](#) [hep-ph].
- [73] A. Efrati, A. Falkowski, and Y. Soreq *JHEP* **07** (2015) 018, [arXiv:1503.07872](#) [hep-ph].
- [74] **SLD Electroweak Group, DELPHI, ALEPH, SLD, SLD Heavy Flavour Group, OPAL, LEP Electroweak Working Group, L3** Collaboration, S. Schael *et al.* *Phys. Rept.* **427** (2006) 257–454, [arXiv:hep-ex/0509008](#) [hep-ex].
- [75] **CMS** Collaboration, V. Khachatryan *et al.* *JHEP* **02** (2017) 048, [arXiv:1611.06594](#) [hep-ex].
- [76] **CMS** Collaboration, V. Khachatryan *et al.* *Phys. Lett.* **B770** (2017) 278–301, [arXiv:1612.09274](#) [hep-ex].
- [77] **ATLAS** Collaboration, M. Aaboud *et al.* *Eur. Phys. J.* **C76** no. 11, (2016) 585, [arXiv:1608.00890](#) [hep-ex].
- [78] **ATLAS** Collaboration, M. Aaboud *et al.* *JHEP* **01** (2018) 055, [arXiv:1709.07242](#) [hep-ex].
- [79] **ATLAS** Collaboration, M. Aaboud *et al.* [arXiv:1706.04786](#) [hep-ex].

- [80] **ATLAS Collaboration** Collaboration Tech. Rep. ATLAS-CONF-2016-085, CERN, Geneva, Aug, 2016. <http://cds.cern.ch/record/2206278>.
- [81] **ATLAS** Collaboration, G. Aad *et al.* *JHEP* **07** (2015) 157, [arXiv:1502.07177](https://arxiv.org/abs/1502.07177) [[hep-ex](#)].
- [82] S. M. Boucenna, A. Celis, J. Fuentes-Martin, A. Vicente, and J. Virto *Phys. Lett.* **B760** (2016) 214–219, [arXiv:1604.03088](https://arxiv.org/abs/1604.03088) [[hep-ph](#)].
- [83] J. Alwall, R. Frederix, S. Frixione, V. Hirschi, F. Maltoni, O. Mattelaer, H. S. Shao, T. Stelzer, P. Torrielli, and M. Zaro *JHEP* **07** (2014) 079, [arXiv:1405.0301](https://arxiv.org/abs/1405.0301) [[hep-ph](#)].
- [84] **ATLAS Collaboration** Collaboration Tech. Rep. ATLAS-CONF-2016-032, CERN, Geneva, Jun, 2016. <http://cds.cern.ch/record/2161545>.
- [85] **CMS** Collaboration, A. M. Sirunyan *et al.* *JHEP* **05** (2017) 029, [arXiv:1701.07409](https://arxiv.org/abs/1701.07409) [[hep-ex](#)].
- [86] **CMS** Collaboration, A. M. Sirunyan *et al.* *Phys. Lett.* **B772** (2017) 634–656, [arXiv:1701.08328](https://arxiv.org/abs/1701.08328) [[hep-ex](#)].
- [87] **ATLAS** Collaboration, M. Aaboud *et al.* *JHEP* **08** (2017) 052, [arXiv:1705.10751](https://arxiv.org/abs/1705.10751) [[hep-ex](#)].
- [88] **CMS** Collaboration, A. M. Sirunyan *et al.* *JHEP* **11** (2017) 085, [arXiv:1706.03408](https://arxiv.org/abs/1706.03408) [[hep-ex](#)].
- [89] **ATLAS** Collaboration, M. Aaboud *et al.* *JHEP* **10** (2017) 141, [arXiv:1707.03347](https://arxiv.org/abs/1707.03347) [[hep-ex](#)].
- [90] **CMS** Collaboration, A. M. Sirunyan *et al.* [arXiv:1708.01062](https://arxiv.org/abs/1708.01062) [[hep-ex](#)].
- [91] **CMS** Collaboration, A. M. Sirunyan *et al.* [arXiv:1708.02510](https://arxiv.org/abs/1708.02510) [[hep-ex](#)].

- [92] **CMS** Collaboration, A. M. Sirunyan *et al.* [arXiv:1710.01539](#) [[hep-ex](#)].
- [93] **CMS** Collaboration, A. M. Sirunyan *et al.* *Phys. Rev. Lett.* **119** no. 22, (2017) 221802, [arXiv:1708.07962](#) [[hep-ex](#)].
- [94] A. Kusenko *Phys. Rept.* **481** (2009) 1–28, [arXiv:0906.2968](#) [[hep-ph](#)].
- [95] F. Bezrukov, H. Hettmansperger, and M. Lindner *Phys. Rev.* **D81** (2010) 085032, [arXiv:0912.4415](#) [[hep-ph](#)].
- [96] T. Asaka, M. Shaposhnikov, and A. Kusenko *Phys. Lett.* **B638** (2006) 401–406, [arXiv:hep-ph/0602150](#) [[hep-ph](#)].
- [97] **Planck** Collaboration, N. Aghanim *et al.* [arXiv:1807.06209](#) [[astro-ph.CO](#)].
- [98] K. Osato, T. Sekiguchi, M. Shirasaki, A. Kamada, and N. Yoshida *JCAP* **1606** no. 06, (2016) 004, [arXiv:1601.07386](#) [[astro-ph.CO](#)].
- [99] K. Ichikawa, M. Kawasaki, K. Nakayama, T. Sekiguchi, and T. Takahashi *JCAP* **0908** (2009) 013, [arXiv:0905.2237](#) [[astro-ph.CO](#)].
- [100] **Planck** Collaboration, P. A. R. Ade *et al.* *Astron. Astrophys.* **594** (2016) A13, [arXiv:1502.01589](#) [[astro-ph.CO](#)].
- [101] J. Kumar, D. London, and R. Watanabe [arXiv:1806.07403](#) [[hep-ph](#)].
- [102] **CMS** Collaboration, A. M. Sirunyan *et al.* [arXiv:1708.00373](#) [[hep-ex](#)].
- [103] **ATLAS, CMS** Collaboration, G. Aad *et al.* *JHEP* **08** (2016) 045, [arXiv:1606.02266](#) [[hep-ex](#)].
- [104] **DELPHI, OPAL, ALEPH, LEP Electroweak Working Group, L3** Collaboration, J. Alcaraz *et al.* [arXiv:hep-ex/0612034](#) [[hep-ex](#)].

- [105] S. Iguro, T. Kitahara, R. Watanabe, and K. Yamamoto [arXiv:1811.08899](#) [hep-ph].
- [106] M. Blanke, A. Crivellin, S. de Boer, M. Moscati, U. Nierste, I. Niandi, and T. Kitahara [arXiv:1811.09603](#) [hep-ph].
- [107] R. Dutta [arXiv:1710.00351](#) [hep-ph].
- [108] F. U. Bernlochner, Z. Ligeti, M. Papucci, and D. J. Robinson *Phys. Rev.* **D95** no. 11, (2017) 115008, [arXiv:1703.05330](#) [hep-ph]. [Erratum: *Phys. Rev.* **D97**, no. 5, 059902(2018)].
- [109] A. Azatov, D. Bardhan, D. Ghosh, F. Sgarlata, and E. Venturini [arXiv:1805.03209](#) [hep-ph].
- [110] A. Angelescu, D. Beirevi, D. A. Faroughy, and O. Sumensari [arXiv:1808.08179](#) [hep-ph].
- [111] R. Alonso, B. Grinstein, and J. Martin Camalich *JHEP* **10** (2015) 184, [arXiv:1505.05164](#) [hep-ph].
- [112] O. Cat and M. Jung *Phys. Rev.* **D92** no. 5, (2015) 055018, [arXiv:1505.05804](#) [hep-ph].
- [113] I. Dorner, S. Fajfer, A. Greljo, J. F. Kamenik, and N. Konik *Phys. Rept.* **641** (2016) 1–68, [arXiv:1603.04993](#) [hep-ph].
- [114] K. S. Babu, C. F. Kolda, and J. March-Russell *Phys. Lett.* **B408** (1997) 261–267, [arXiv:hep-ph/9705414](#) [hep-ph].
- [115] **H1** Collaboration, C. Adloff *et al.* *Z. Phys.* **C74** (1997) 191–206, [arXiv:hep-ex/9702012](#) [hep-ex].

- [116] **ZEUS** Collaboration, J. Breitweg *et al.* *Z. Phys.* **C74** (1997) 207–220,
arXiv:hep-ex/9702015 [hep-ex].
- [117] A. Manohar and H. Georgi *Nucl. Phys.* **B234** (1984) 189–212.
- [118] Y. Grossman, Z. Ligeti, and E. Nardi *Nucl. Phys.* **B465** (1996) 369–398,
arXiv:hep-ph/9510378 [hep-ph]. [Erratum: *Nucl. Phys.*B480,753(1996)].
- [119] W. Altmannshofer, A. J. Buras, D. M. Straub, and M. Wick *JHEP* **04** (2009)
022, arXiv:0902.0160 [hep-ph].
- [120] B. Dumont, K. Nishiwaki, and R. Watanabe *Phys. Rev.* **D94** no. 3, (2016)
034001, arXiv:1603.05248 [hep-ph].
- [121] M. E. Peskin and T. Takeuchi *Phys. Rev.* **D46** (1992) 381–409.
- [122] P. H. Frampton and M. Harada *Phys. Rev.* **D58** (1998) 095013,
arXiv:hep-ph/9711448 [hep-ph].
- [123] L. Lavoura and L.-F. Li *Phys. Rev.* **D48** (1993) 234–239.
- [124] **CMS** Collaboration, A. M. Sirunyan *et al.* *JHEP* **07** (2017) 121,
arXiv:1703.03995 [hep-ex].
- [125] B. Diaz, M. Schmaltz, and Y.-M. Zhong *JHEP* **10** (2017) 097,
arXiv:1706.05033 [hep-ph].
- [126] **CMS** Collaboration, A. M. Sirunyan *et al.* *Eur. Phys. J.* **C78** (2018) 707,
arXiv:1803.02864 [hep-ex].
- [127] J. E. Camargo-Molina, A. Celis, and D. A. Faroughy *Phys. Lett.* **B784** (2018)
284–293, arXiv:1805.04917 [hep-ph].
- [128] **CMS** Collaboration, A. M. Sirunyan *et al.* *Phys. Rev.* **D98** no. 3, (2018)
032005, arXiv:1805.10228 [hep-ex].

- [129] M. Schmaltz and Y.-M. Zhong *JHEP* **01** (2019) 132, [arXiv:1810.10017](#) [[hep-ph](#)].
- [130] **CMS** Collaboration, A. M. Sirunyan *et al.* *Submitted to: JHEP* (2018) , [arXiv:1811.00806](#) [[hep-ex](#)].
- [131] **ATLAS** Collaboration, M. Aaboud *et al.* [arXiv:1902.08103](#) [[hep-ex](#)].
- [132] **CMS** Collaboration, A. M. Sirunyan *et al.* *JHEP* **07** (2018) 115, [arXiv:1806.03472](#) [[hep-ex](#)].
- [133] **CMS** Collaboration, A. M. Sirunyan *et al.* *Phys. Rev.* **D97** no. 9, (2018) 092005, [arXiv:1712.02345](#) [[hep-ex](#)].
- [134] **CMS** Collaboration, A. M. Sirunyan *et al.* *Phys. Rev.* **D96** no. 3, (2017) 032003, [arXiv:1704.07781](#) [[hep-ex](#)].
- [135] **ATLAS** Collaboration, M. Aaboud *et al.* *JHEP* **09** (2017) 088, [arXiv:1704.08493](#) [[hep-ex](#)].
- [136] **CMS** Collaboration, A. M. Sirunyan *et al.* *Eur. Phys. J.* **C77** no. 10, (2017) 710, [arXiv:1705.04650](#) [[hep-ex](#)].
- [137] **CMS** Collaboration, A. M. Sirunyan *et al.* *JHEP* **10** (2017) 019, [arXiv:1706.04402](#) [[hep-ex](#)].
- [138] **ATLAS** Collaboration, M. Aaboud *et al.* *JHEP* **11** (2017) 195, [arXiv:1708.09266](#) [[hep-ex](#)].
- [139] **CMS** Collaboration, A. M. Sirunyan *et al.* *Phys. Lett.* **B780** (2018) 384–409, [arXiv:1709.09814](#) [[hep-ex](#)].
- [140] **ATLAS** Collaboration, M. Aaboud *et al.* *JHEP* **06** (2018) 107, [arXiv:1711.01901](#) [[hep-ex](#)].

- [141] **ATLAS** Collaboration, M. Aaboud *et al.* *Phys. Rev.* **D97** no. 11, (2018) 112001, [arXiv:1712.02332](#) [[hep-ex](#)].
- [142] **CMS Collaboration** Collaboration, “Searches for new phenomena in events with jets and high values of the M_{T2} variable, including signatures with disappearing tracks, in proton-proton collisions at $\sqrt{s} = 13$ TeV,” Tech. Rep. CMS-PAS-SUS-19-005, CERN, Geneva, 2019.
<https://cds.cern.ch/record/2668105>.
- [143] J. Fan, M. Reece, and J. T. Ruderman *JHEP* **11** (2011) 012, [arXiv:1105.5135](#) [[hep-ph](#)].
- [144] J. Fan, M. Reece, and J. T. Ruderman *JHEP* **07** (2012) 196, [arXiv:1201.4875](#) [[hep-ph](#)].
- [145] Y. Nakai, M. Reece, and R. Sato *JHEP* **03** (2016) 143, [arXiv:1511.00691](#) [[hep-ph](#)].
- [146] A. Greljo and D. Marzocca *Eur. Phys. J.* **C77** no. 8, (2017) 548, [arXiv:1704.09015](#) [[hep-ph](#)].
- [147] **ATLAS** Collaboration, M. Aaboud *et al.* *JHEP* **10** (2017) 182, [arXiv:1707.02424](#) [[hep-ex](#)].
- [148] A. Greljo, J. Martin Camalich, and J. D. Ruiz-Álvarez *Phys. Rev. Lett.* **122** no. 13, (2019) 131803, [arXiv:1811.07920](#) [[hep-ph](#)].
- [149] **CMS** Collaboration, A. M. Sirunyan *et al.* *Phys. Rev.* **D99** no. 1, (2019) 012010, [arXiv:1810.10092](#) [[hep-ex](#)].
- [150] T. Sjöstrand, S. Ask, J. R. Christiansen, R. Corke, N. Desai, P. Ilten, S. Mrenna, S. Prestel, C. O. Rasmussen, and P. Z. Skands *Comput. Phys. Commun.* **191** (2015) 159–177, [arXiv:1410.3012](#) [[hep-ph](#)].

- [151] **DELPHES 3** Collaboration, J. de Favereau, C. Delaere, P. Demin, A. Giammanco, V. Lematre, A. Mertens, and M. Selvaggi *JHEP* **02** (2014) 057, [arXiv:1307.6346 \[hep-ex\]](#).
- [152] P. Asadi, M. R. Buckley, A. DiFranzo, A. Monteux, and D. Shih *JHEP* **11** (2017) 194, [arXiv:1707.05783 \[hep-ph\]](#).
- [153] **ATLAS** Collaboration, M. Aaboud *et al.* *Phys. Rev.* **D96** no. 11, (2017) 112010, [arXiv:1708.08232 \[hep-ex\]](#).
- [154] **BaBar** Collaboration, J. P. Lees *et al.* *Phys. Rev.* **D87** no. 11, (2013) 112005, [arXiv:1303.7465 \[hep-ex\]](#).
- [155] **Belle** Collaboration, J. Grygier *et al.* *Phys. Rev.* **D96** no. 9, (2017) 091101, [arXiv:1702.03224 \[hep-ex\]](#). [Addendum: *Phys. Rev.* **D97**, no. 9, 099902 (2018)].
- [156] D. J. Robinson, B. Shakya, and J. Zupan [arXiv:1807.04753 \[hep-ph\]](#).
- [157] **Belle** Collaboration, T. Saito *et al.* *Phys. Rev.* **D91** no. 5, (2015) 052004, [arXiv:1411.7198 \[hep-ex\]](#).
- [158] **BaBar** Collaboration, J. P. Lees *et al.* *Phys. Rev. Lett.* **118** no. 3, (2017) 031802, [arXiv:1605.09637 \[hep-ex\]](#).
- [159] **LHCb** Collaboration, R. Aaij *et al.* *Phys. Rev. Lett.* **118** no. 25, (2017) 251802, [arXiv:1703.02508 \[hep-ex\]](#).
- [160] C. Murgui, A. Peuelas, M. Jung, and A. Pich [arXiv:1904.09311 \[hep-ph\]](#).
- [161] K. Agashe, R. Contino, and A. Pomarol *Nucl. Phys.* **B719** (2005) 165–187, [arXiv:hep-ph/0412089 \[hep-ph\]](#).
- [162] D. B. Kaplan *Nucl. Phys.* **B365** (1991) 259–278.

- [163] M. Freytsis, Z. Ligeti, and J. T. Ruderman *Phys. Rev.* **D92** no. 5, (2015) 054018, [arXiv:1506.08896 \[hep-ph\]](#).
- [164] I. Dorner, S. Fajfer, N. Konik, and I. Niandi *JHEP* **11** (2013) 084, [arXiv:1306.6493 \[hep-ph\]](#).
- [165] Y. Sakaki, M. Tanaka, A. Tayduganov, and R. Watanabe *Phys. Rev.* **D91** no. 11, (2015) 114028, [arXiv:1412.3761 \[hep-ph\]](#).
- [166] **ALEPH** Collaboration, R. Barate *et al.* *Eur. Phys. J.* **C19** (2001) 213–227, [arXiv:hep-ex/0010022 \[hep-ex\]](#).
- [167] A. Monteux and A. Rajaraman [arXiv:1803.05962 \[hep-ph\]](#).
- [168] A. Greljo, D. J. Robinson, B. Shakya, and J. Zupan [arXiv:1804.04642 \[hep-ph\]](#).
- [169] M. A. Ivanov, J. G. Krner, and C.-T. Tran *Phys. Rev.* **D94** no. 9, (2016) 094028, [arXiv:1607.02932 \[hep-ph\]](#).
- [170] **Belle** Collaboration, S. Hirose *et al.* *Phys. Rev. Lett.* **118** no. 21, (2017) 211801, [arXiv:1612.00529 \[hep-ex\]](#).
- [171] **The Belle Collaboration** Collaboration, S. Hirose *et. al.* *Phys. Rev. D* **97** (Jan, 2018) 012004.
<https://link.aps.org/doi/10.1103/PhysRevD.97.012004>.